Development of a Liquid Crystal Tunable Filter Based Shortwave Infrared Spectral Imaging System and its Application in the Early Detection of Sour Skin in Onions

by

Weilin Wang

(Under the direction of Changying Li and Ernest William Tollner)

Abstract

Shortwave infrared spectral imaging is an emerging nondestructive technique for food safety and quality inspection. In this research, a liquid crystal tunable filter based shortwave infrared spectral imaging system was developed based on the state-of-the-art technologies. The system was fully calibrated and optimized in both spectral and spatial domains. A LabVIEW software program was also developed for image acquisition. The system can be used for hyperspectral or multispectral image acquisition in the spectral range of 900 - 1700 nm.

The spectral imaging system was applied to detect sour skin in Vidalia sweet onions. A nondestructive sensing method was developed based on the shortwave infrared spectral imaging. The method can effectively detect sour skin in onions in the early stage. Results of these studies indicated that this shortwave infrared spectral imaging system is a powerful nondestructive tool for food safety and quality inspection.

Index words: Hyperspectral Imaging, Multispectral Imaging, LCTF, NDT, Near-infrared, SWIR, Spectral, Onion, Vidalia sweet onions, Sour skin, LabVIEW, Quality, Software development

Development of a Liquid Crystal Tunable Filter Based Shortwave Infrared Spectral Imaging System and its Application in the Early Detection of Sour Skin in Onions

by

Weilin Wang

B.S., China Agricultural University, China, 2002

A Thesis Submitted to the Graduate Faculty
of The University of Georgia in Partial Fulfillment
of the
Requirements for the Degree

Master of Science

Athens, Georgia

2010

Development of a Liquid Crystal Tunable Filter Based Shortwave Infrared Spectral Imaging System and its Application in the Early Detection of Sour Skin in Onions

by

Weilin Wang

Approved:

Major Professor:	Changying Li
Co-Major Professor:	Ernest William Tollner
Committee:	Ron Gitaitis
	Glen Rains

Electronic Version Approved:

Maureen Grasso
Dean of the Graduate School
The University of Georgia
December 2010

Dedication

To:

My wife

– Min Wang

My Parents

– Ping Wang and Xiaoqin Wang

Acknowledgments

I would like to express my earnestly gratitude to my major professor Dr. Changying Li. He mentored and supported me tirelessly through this research. I appreciate his encouragement and trust in past two years, which helped me greatly in my work. Without his great effort on me and this project, this thesis would not be so fruitful.

I would like to sincerely thank my co-advisor Dr. Ernest W. Tollner. At many times, he guided me to think negative problems from different perspectives. His support and help are throughout my study and research. I am very grateful to Dr. Ron Gitaitis for his invaluable help for my research. He guided me to understand many interesting things in onion world and helped me obtain enthusiasm in this project. I also want to extend my thanks to Dr. Glen Rains, who offered timely support and help for every question or request that I asked. Moreover, I would like to show my appreciation to Dr. Seung-Chul Yoon and Dr. Chi N. Thai, who helped me on the hyperspectral imaging at the beginning of my research.

I also want to express my gratitude to my lab colleagues and other graduate students in Biological and Agricultural Engineering department for their friendship and assistance. Particularly, I thank our lab technicians Mr. Gary Burnham and Mr. Tim Rutland for their excellent assistance. Special thanks go to my friends, Qi Wang and Herbert Ssegane, who have shared their invaluable Ph.D study and research experience with me.

Finally, I would like to acknowledge the funding support of USDA National Institute for Food and Agriculture (NIFA) Specialty Crops Research Initiative (SCRI), Georgia Food Industry Partnership, Vidalia onion committee, and Georgia Vegetable Commission.

Table of Contents

List of Figures

List of Tables

Chapter 1

Introduction

This thesis presents a research with three main aspects: the development of a liquid crystal tunable filter (LCTF) based shortwave infrared (SWIR) spectral imaging system, the development of a LabVIEW data acquisition software program for the LCTF-based spectral imaging system, and the early detection of sour skin in Vidalia sweet onions by using the SWIR spectral imaging technique. This chapter provides a brief introduction of the background, the motivations, and the objectives of this research. The last section of this chapter provides an overview for the overall structure of the thesis.

1.1 Project Background and Motivations

Vidalia sweet onion is one of the most important contributors to the agricultural economy of the state of Georgia. The brand of Vidalia sweet onions is recognized nationally (Clemens, 2002). This national reputation was confirmed by a survey of primary food shoppers in 2003 (Costa et al., 2004): about 63% of respondents indicated that the Vidalia onions were their favorite sweet onions. Vidalia onion production has dramatically increased in the last two decades. In 1989, there were only 4800 acres of Vidalia onions planted in Georgia, with a farm gate value of $17.27 million (USDA, 2005). In 2009, about 13,000 acres of Vidalia onions were planted in Georgia, which contributed a farm gate value of $126 million, 13.77% of Georgia's total vegetable farm gate value in the year (Boatright and McKissick, 2010).

The great success of Vidalia sweet onions can be attributed to its national reputation, regulatory control of the Vidalia name, the adoption of controlled atmosphere (CA) storage, and the effective marketing and research assistance from research institutions. Among these

factors, the CA storage technology, which was introduced into the Vidalia onion industry in the 1990s, plays a critical role. The main benefit of using CA storage is that it extends the marketing season of Vidalia onions from spring to fall, and thus it enables growers to keep a premium price for a longer time (Boyhan and Torrance, 2002). However, the performance of CA storage has been inconsistent with respect to the quality of stored onions. Thus, the percent marketable onions after CA storage would fluctuate rapidly from year to year (Boyhan et al., 2005). In some years, annual onion production and storage losses would be up to 70% due to postharvest diseases (Schwartz and Mohan, 2008). Although postharvest diseases in onion storage are very difficult to be avoided, they can be controlled or slowed within certain limits. One of the most effective methods is to identify and eliminate those diseased onions in packing houses before they are stored in CA rooms. Nevertheless, it is extremely difficult to assess the quality of onion bulbs because they are covered by thick and inhomogeneous dry leaves. Also, most of onion diseases happen inside onion bulbs at the early stage. Currently nondestructive inspection technologies used by the onion industry, such as human visual inspection (HVI) and conventional machine vision approaches, are not able to detect internal defects and diseases of onions and also cannot assess invisible quality attributes of onions such as sugar content and dry matter content. Therefore, research on advanced sensing technologies for quality inspection of onions is highly demanded.

Another imperative motivation for developing effective sensing technologies for quality inspection of onions was the increasing consumer demand on high quality onion products. Vidalia onions now face the increased competition from both other states in U.S and South America. Since Vidalia sweet onions are mild and lack some pungent compounds, which make them prone to bruising and postharvest diseases (Maw et al., 1996). Without effective quality control, onions with internal diseases or external defects could readily be delivered into the fresh vegetable market, which will greatly reduce consumers' satisfaction.

To keep the competitive advantage of Vidalia onions, more stringent inspection and grading requirements had been applied to the Vidalia onion industry in 2002. From that

time, all Vidalia onions have to be inspected and pass U.S. No.1 grade before they are sold (State of Georgia, 2003). However, current inspection is conducted mainly by using human visual inspections. It's difficult to identify onions with internal defects and diseases by human labors. Moreover, results of human visual inspections are often inconsistent. Although inspectors under federal and state supervision inspect 100% of Vidalia onions, currently inspection methods are often limited to straightforward factors like shape, size, color, and etc.

To address onion postharvest problems and enhance onion postharvest handling efficiency, a research team including scientists in the University of Georgia has proposed a series of multi-disciplinary research plans. These ongoing research efforts have been financially supported by USDA National Institute for Food and Agriculture (NIFA) Specialty Crops Research Initiative (SCRI), Georgia Food Industry Partnership, Vidalia onion committee, and Georgia Vegetable Commission. The research reported in this thesis is part of this comprehensive study. The principal incentive of my thesis work was to develop effective engineering solutions to enhance the onion quality inspection efficiency.

1.2 Objectives

The work reported by this thesis aimed to develop sensing methods that can be used to improve the efficiencies of the quality inspection and classification of onions. From our preliminary studies, the shortwave infrared (SWIR) spectral imaging showed great potentials for developing new nondestructive inspection techniques to test onion quality, due to its capability of collecting both spatial and spectral characteristics of the test object. Thus, the main target of this work was to develop an SWIR spectral imaging system for non-destructive quality inspection of onions. The detailed objectives of this research theme were to:

- Design and calibrate a high performance SWIR spectral imaging system.

- Develop a user friendly spectral image acquisition software program on the LabVIEW platform.
- Apply the system to detect sour skin-infected onions in the early stage.

1.3 Thesis Overview

The first chapter of the thesis introduces the project background, rationales and objectives. It also presents a brief overview of the organization of the chapters in this thesis. Chapter 2 reviews the literatures of the fundamental principles of multispectral and hyperspectral imaging techniques, the development and applications of spectral imaging systems in food and agricultural inspection, and the cause organism and symptoms of sour skin-infected onions. Chapter 3 demonstrates the development of a shortwave infrared spectral imaging system, and discusses the architecture, development, and calibration of the system in details. Chapter 4 illustrates the design and implementation of the spectral image acquisition software for the LCTF spectral imaging system. Chapter 5 presents a successful application of the spectral imaging system for the early detection of sour skin in Vidalia onions. Finally, chapter 6 discusses the results and significances of this work and draws conclusions. Future improvements of the system and its potential applications in onion quality inspection are also discussed in chapter 6.

1.4 Bibliography

Boatright, S. R., McKissick, J. C., 2010. 2009 georgia farm gate value report. Tech. rep., The University of Georgia, Center for Agribusiness and Economic Development College of Agricultural and Environmental Sciences.

Boyhan, G. E., Purvis, A. C., Randle, W. M., Torrance, R. L., Jefferson Cook, M. J. I., Hardison, G., Blackley, R. H., Paradice, H., Hill, C. R., Paulk, J. T., 2005. Harvest and

postharvest quality in short-day onions in variety trials in georgia, 2000-03. HortTechnology 15, 694–706.

Boyhan, G. E., Torrance, R. L., 2002. Vidalia onions–sweet onion production in southeastern georgia. HortTechnology 12 (2), 196–202.

Clemens, R., 2002. Why can't vidalia onions be grown in iowa? developing a branded agricultural product. Center for Agricultural and Rural Development, Iowa State University.

Costa, E. F., Wolfe, K., Epperson, J. E., 2004. The consumers of vidalia onions. Journal of Food Products Marketing 10 (4), 59 – 72.

Maw, B., Hung, Y., Tollner, E., Smittle, D., Mullinix, B., 1996. Physical and mechanical properties of fresh and stored sweet onions. Transactions of the ASAE 39 (2), 633–637.

Schwartz, H. F., Mohan, S. K., 2008. Compendium of onion and garlic diseases and pests, 2nd Edition. Disease compendium series of the American Phytopathological Society. APS Press, American Phytopathological Society, St. Paul, Minn.

State of Georgia, 2003. HB 798 - Vidalia Onion Act; amend provisions.

USDA, 2005. Official Georgia Estimates - Onions. The Georgia Field Office of the National Agricultural Statistics Service (NASS).

Chapter 2

Quality inspection of food and agricultural products by shortwave infrared LCTF spectral imaging - overview

Quality produce is very important to consumers and retailers, and it is a key factor consumers use in evaluating a supermarket.

— *Christine M. Bruhn*

2.1 Introduction

Currently, US consumers have an unprecedented interest in safety and quality of their food. Government authorities are also interested in public health and consumer protection and place considerable obligations to ensure the safety and quality of food. As a result, assuring the safety and quality of food and agricultural products has become one of the major goals of food engineering in the 21st century. To provide effectual food safety and quality inspection and consumer protection, the need of high performance nondestructive inspection technologies is rapidly increasing.

Optical technology has been widely used for nondestructive inspection of food and agricultural products due to its fast, objective and nondestructive nature. The most common optical inspection techniques are color and monochrome imaging methods. Color and monochrome imaging technologies investigate the spatial distribution of light intensity in visible or near-infrared range and are often used for classification of size, color, and shape (Davies, 2009). Another widely adopted optical technology for inspection is the spectroscopy technique (Nicolai et al., 2007). Different from imaging techniques which mainly examine the surface irradiance of the test object, spectroscopy is an analytical technique that studies the

interaction between the light and the matter. Spectroscopy can examine internal physical or chemical characteristics of the test object while conventional color or monochrome imaging only measures external characteristics of the tested object.

Taking advantages of strengths of both imaging and spectral techniques, a technique called spectral imaging was developed in the 1980s (Kerekes and Schott, 2007). Spectral imaging collects information of a test object in spectral and spatial domains simultaneously. As a result, spectral images contain a wealth of spectral and image data. However, due to its high requirements of hardware, this technique was constrained mainly in astrophysics, remote sensing, and military applications until the middle of 1990s. Since the late 1990's, spectral imaging has been adopted to food safety and quality inspection (Lu and Chen, 1998) and has undergone a rapid development since recent advances in electronics and optics have reduced the cost to a practical range. Because of its capability to characterize a test object in both spectral and spatial domains, spectral imaging has been widely accepted for nondestructive inspection of food and agricultural products.

Based on the wavelength number (n), spectral imaging can be divided into two divisions: hyperspectral imaging (n>10) and multispectral imaging (n<10). In the current literature, spectral imaging is often referred to hyperspectral imaging (HSI). Similar with the spectroscopy technology, spectral imaging can be divided to many divisions based on the range in electromagnetic spectrum. There are a number of ways to divide the electromagnetic spectrum of light in this range. In the literature regarding spectral imaging for food and agricultural products quality inspection, several division schemes have been found for subdividing the electromagnetic spectrum of light: ISO 20473 (International Organization for Standardization, 2007a), ISO 21348 (International Organization for Standardization, 2007b), and the division scheme based on sensor response (Miller, 1994). Figure 2.1 shows the division schemes of these three methods. ISO 20473 and the division scheme based sensor response are two most common methods used in food and agricultural engineering area. The division scheme of ISO 21348 is similar with the division scheme recommended by International

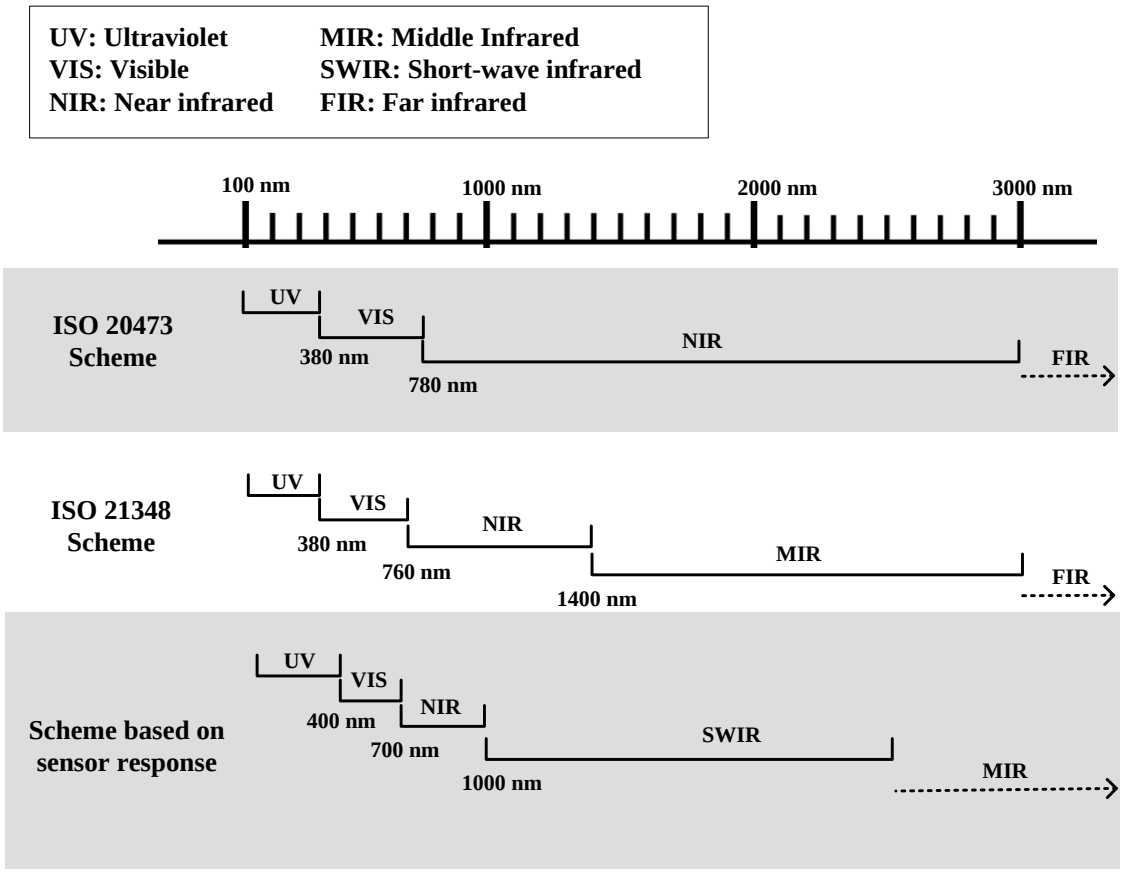

Figure 2.1: Part of the electromagnetic radiation spectrum which is of interest in spectral imaging and three common subdivision schemes for the range of electromagnetic radiation spectrum

Commission for Illumination (CIE). But this scheme has been rarely reported in the literature of food and agricultural engineering. In this thesis, the division scheme based on sensor response is used.

2.2 Spectral imaging systems

Spectral imaging includes hyperspectral imaging and multispectral imaging (MSI). Both HSI and MSI are fast growing areas in non-invasive inspection for food safety and quality.

Hyperspectral imaging has superior inspection capabilities because it is able to collect full spectral and spatial information of the test object simultaneously (Gowen et al., 2007). Multispectral imaging only collects spatial information of the test object at a small number of wavelength bands that contain most useful information for inspection or classification. Hence, multispectral imaging is much faster and more efficient than hyperspectral imaging. On the other hand, since hyperspectral imaging technique collects information over full spectral region prior to understanding spectral characteristics of the test object, it has unique strengths in developing algorithms for multispectral imaging.

2.2.1 Techniques for spectral imaging system

Hyperspectral/multispectral imaging systems can mainly be grouped into two categories based on spatial scanning and spectral selection techniques (Kerekes and Schott, 2007):

- Systems that use filter wheel, interferometer, or tunable filter (TF) to collect spectrum over time, and make use of two-dimensional framing cameras for imaging.
- Systems that use prism and grating methods for spreading out spectrum spatially, and collect images by using line-scan, whiskbroom, or pushbroom scanning techniques.

In food safety and quality inspection, most reported multispectral imaging systems are grouped in the first category. For hyperspectral imaging, configurations in both categories are widely used. Specifically, two HSI configurations have commonly been used for food safety and quality inspection (Gowen et al., 2007):

- The system that uses a line scanner and moves the scanner or the test object during scanning. These systems often use line-scan (moving the test object) or pushbroom (moving the line scanner) acquisition modes.
- The system that uses an electronically tunable filter (ETF) for selecting wavelength bands iteratively and takes 2-D images over time.

A line-scan/pushbroom HSI system for food safety and quality inspection often uses a spectrograph to disperse light from a slit over a two-dimensional focal-plan-array (FPA). When the sensor scans in the direction that is perpendicular to the slit, the images captured by the camera FPA can record the spectral information of the test object line by line. Thus, the spectral and spatial information of the entire object in a given wavelength range can be obtained.

Compared to the identical configuration of line-scan HSI systems, configurations for filter-based HSI systems are more diverse. One decade ago, Gat (2000) reviewed the mainstream configurations of tunable filter (TF) based spectral imaging system. In the past decade, the ETF based spectral imager has gained wide acceptance for spectral imaging. Two types of electronically tunable filters have been reported in food engineering literature. One is liquid crystal tunable filter (LCTF) and the other is acousto-optical tunable filter (AOTF) (Gowen et al., 2007). A liquid crystal tunable filter is essentially a multistage Lyot-Ohman type polarization interference filter using a stack of polarizers and tunable retardation liquid crystal plates (Tran, 2005). An AOTF applies radio frequency acoustic waves to a crystal to separate a broadband light beam and then selects a single wavelength light (Bei et al., 2004).

Comparing the LCTF and the AOTF, the main strengths of the LCTF are large aperture, large field of view, low wave front distortion, and flexible throughput control. The major weaknesses of the LCTF are its low throughput and slower tuning speed (Evans et al., 1998). On the other hand, the main advantages of the AOTF are good transmission, faster tuning time, and broad spectral range. Disadvantages of the AOTF are smaller aperture, broad spectral imaging bandpass, and striking image shifting during wavelength tuning. In summary, the LCTF-based HSI system is relatively slower than the HSI system using an AOTF, but it often provides better imaging performance.

2.2.2 Principles of Liquid Crystal Tunable Filter

Liquid crystal tunable filters select a narrow band of light centering at a specific wavelength for transmission and block all others. A typical LCTF consists of a stack of filters. Generally, each filter is a combination of a briefringent element with fixed retardance, a liquid crystal waveplate, and linear polarizers, as shown in figure 2.2a. The briefringent element and linear polarizers form an essentially Lyot-Ohman type polarization interference filter, which can select light of a specific frequency. The further electronical control of light selection is implemented by the liquid crystal waveplate. Each liquid crystal waveplate contains a cell of liquid crystals and two transparent electrodes (see figure 2.2b). When voltage is applied across the electrodes, liquid crystal molecules re-align their orientations based on the E-field introduced. As a result, the retardance of the liquid crystal waveplate changes, which also changes the overall retardance of the filter. Thus, the retardance of the filter is adjusted electronically by controlling the voltage applied to the liquid crystal waveplate.

The filter element of the LCTF filters light according to the choice of polarizers, the fixed retarder, and the liquid crystal waveplate. Since the retardance of the filter element is adjustable, a narrow bandpass of light could be selected by a combination of selective transmissions of the filters inside the LCTF. Figure 2.2c shows the principle of selecting a single passband of light by the LCTF. In summary, when light passes through the LCTF, multiple retardance stages caused by successive filters select light step by step until a narrow band of light is isolated. Detail introduction of the working principle of the LCTF can be found in Slawson et al. (1999).

2.2.3 Hyperspectral imaging, Pushbroom vs. Electronically Tunable Filters

The line-scan/pushbroom hyperspectral imaging has been studied in depth and has gained considerable acceptance for food safety and quality inspection (Wang and Paliwal, 2007; Gowen et al., 2007; Kim et al., 2001) due to its high speed and high spectral resolution.

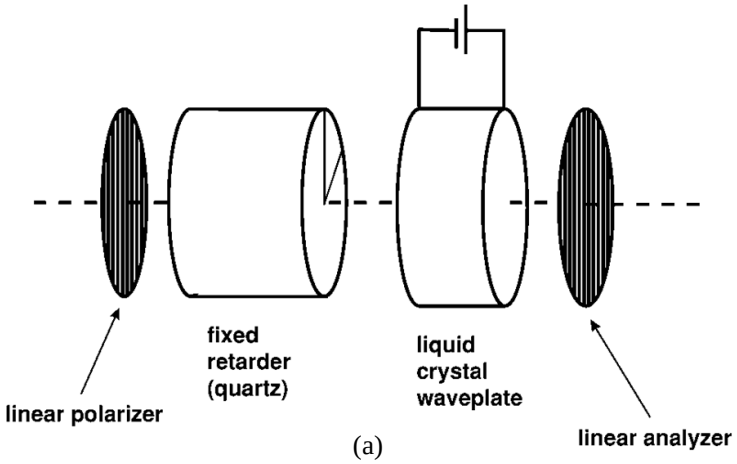

(a)

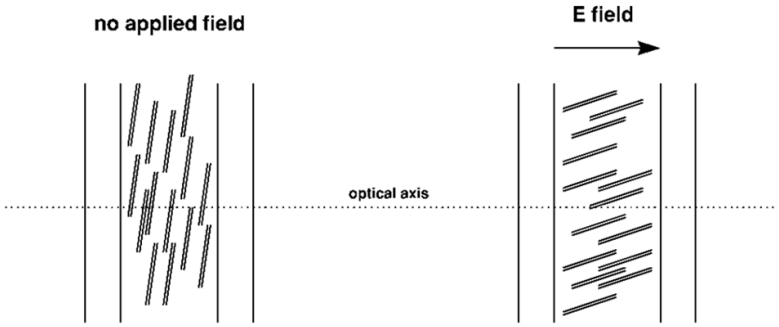

(b)

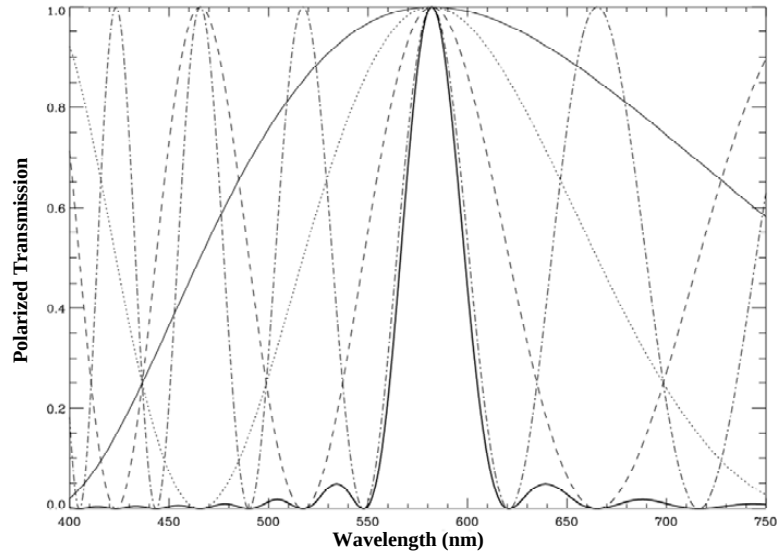

(c)

Figure 2.2: (a) Schematic diagram of a single Lyot-Ohman cell, (b) alignment of liquid crystal in the presence of the E-field, (c) ideal transmittance through through all four stages. The whole figure was adapted from Slawson et al. (1999)

Another reason for the popularity of the line-scan HSI configuration is that the line-scan technique can be readily integrated with the current online inspection systems using a conveyor belt. Since the majority of HSI applications for food and agricultural products inspection target at real time inspections for online sorting and classification, the line-scan technique is preferred by agricultural researchers.

On the other hand, the hyperspectral imaging system based on an ETF has its advantages in many respects. First, an ETF-based HSI system is a natural extension of a multispectral imaging system, which provides the versatility to the system to be used for either HSI or MSI applications. Second, an ETF-based HSI system has an area field of view (FOV), whereas the line-scan HSI systems can only see one line of the test object at one moment. Thus, the ETF-based HSI systems have superiority for instantaneous imaging applications. Third, the ETF-based HSI systems select spectral bands rapidly and randomly, which make them appropriate for applications required selective spectral information. Moreover, the parameter setting of an ETF-based spectral imaging system, such as the exposure time of the camera, is often dynamic and adjustable over each spectral band in a scan, while a pushbroom system often has to keep its parameter setting constant during scanning. Finally, compared to the line-scan systems, the ETF-based spectral imaging systems do not rely on moving mechanical devices such as a linear conveyer module. Therefore, they are compact, easily integrated with other applications, and have higher potential for the field employment.

In the past decade, a number of ETF-based spectral imaging systems have been reported for food and agricultural products quality inspection. Evans et al. (1998) demonstrated a LCTF spectral imaging system for studying plant health, and introduced a calibration approach of leveling system response by linear and logarithmic methods. Cogdill et al. (2004) reported a LCTF-based HSI system for predicting the constituent concentrations of maize kernels by hyperspectral transmittance imaging. Singh et al. (2010b) used the LCTF-based spectral imaging for detecting fungal contamination in wheat and identifying insect-damaged

wheat kernels. However, to date, techniques of applying the LCTF-based spectral imaging system for food safety and quality inspection have not been sufficiently explored.

2.3 Shortwave-infrared spectral imaging for food and agricultural products inspection

2.3.1 Principles of shortwave-infrared technology

Shortwave infrared (SWIR) covers the wavelength range from 1000 nm to 3000 nm. This spectral range is classified as near-infrared in ISO 20473 scheme. The utility of SWIR spectral technology has been successfully demonstrated by numerous nondestructive inspection applications of fruit and vegetable (Williams et al., 2001; Nicolai et al., 2007). The fundamentals of the SWIR spectral technology are the interactions between the light and the matter. Figure 2.3 shows the schematic of the interaction between the light and an onion bulb. When the incident light is projected on the test object, light energy can be absorbed, transmitted and reflected, with a wavelength dependency determined by the material physical or chemical properties. The wavelength dependency can be observed in spectral curves within a given spectral range. The reflectance, transmittance or scattering spectra of the test object could contain useful physical or chemical information, which is induced by the electronic and vibration absorption process of the constituent materials.

Currently, most spectral instruments measure the radiation of reflectance or transmittance. The spectral absorption of the test object can be obtained from the reflectance or transmittance by using the Beer-Lambert law:

$$A = \log \frac{I_o}{I_t}$$

in which A is the absorption, I_o is the incident radiation, and I_t is the intensity of the reflectance or transmittance raditaion (Williams et al., 2001).

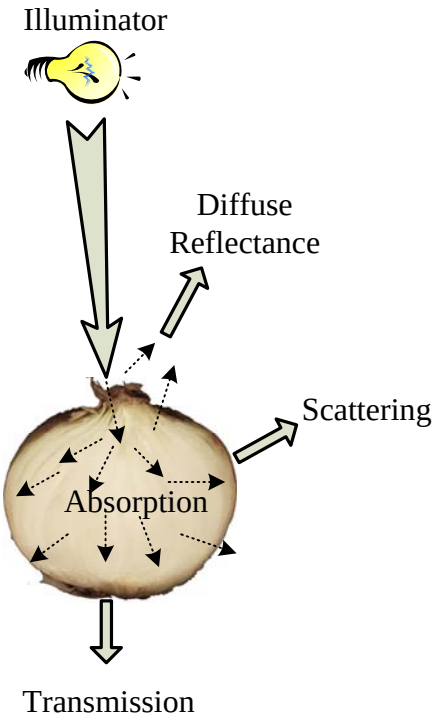

Figure 2.3: The illustration of four types of light interactions with an onion bulb

2.3.2 Applications of shortwave-infrared spectral imaging for quality inspection of food and agricultural products

Shortwave infrared spectral imaging is a recent trend of spectral techniques. Wang and Paliwal (2007) has reviewed the shortwave-infrared spectral imaging applications for food quality and safety inspection by 2006. This section illustrates an overview of the shortwave-infrared spectral imaging applications for quality inspection of food and agricultural products from 2006 to 2010 (table 2.1). The table 2.1 only includes peer-reviewed publications. Papers in conference proceedings are not included since most of them overlap with publications in this list.

The majority of the reported SWIR spectral imaging applications in table 2.1 used the LCTF-based or the line-scan/pushbroom systems for food quality and safety inspections.

Sugiyama et al. (2010) reported a system with a seldom used configuration in spectral imaging, which tunes wavelength bands by filtering the light source. This method is often used with spectroscopy, but its performance for that system is unknown.

Most applications in table 2.1 studied the spectral range from 900 nm to 1700 nm. This was likely due to the availability and the cost of off-the-shelf hardware products. A few applications extended the upper bound to 2500 nm by using up-to-date spectrographs and HgCdTe detectors. Similar with the SWIR or NIR spectroscopy techniques, the SWIR spectral imaging were used mainly for detecting internal/invisible attributes that can be traced by the SWIR spectrum. Thus, the spectral sensitivity of the SWIR spectral imaging system is still a key foundation for the success of the SWIR spectral imaging application.

In addition, the feature selection and classification techniques used by the SWIR applications were classical chemometrics for spectral images, such as PLS, PCA, LDA, etc (table 2.1). Moreover, all of these applications were conducted in the laboratory. This indicates the SWIR spectral imaging technique is still at the research stage. However, these publications demonstrated the feasibility of using the SWIR spectral imaging for safety and quality inspection of food and agricultural products. It appears that developing high performance hardware and advanced spectral image analysis techniques is the current trend of the SWIR spectral imaging.

2.4 Sour skin - one of the major threats for onion postharvest

Sour skin is one of major threats for onions. The cause of sour skin is the gram-negative organism bacterium *Burkholderia cepacia*, which is the phytopathogen responsible for a bacterial rot of onions. *Burkholderia cepacia* is a versatile organism found as an inhabitant of soil and water. Bacterial cells are rods occurring singly or in pairs. The optimum growth temperature for *B. cepacia* is 30-35 °C and they could stop grow below 4 °C (Schwartz and Mohan, 2008).

Table 2.1: Overview of shortwave-infrared spectral imaging applications for quality inspection of food and agricultural products

Product	Subject(s)	Acquisition mode	Wavelength selection method	Spectral range (nm)	Feature selection classification methods	Reference(s)
Apple	Bitter pit	Reflectance	Line-scan	1000 - 1600	Partial least squares (PLS)	Nicolai et al. (2006)
Pickling cucumber	Bruises	Reflectance	Line-scan	900 - 1700	Principal component data (PCA), band ratio	Ariana et al. (2006)
Beef	Tenderness	Reflectance	pushbroom	900-1700	PLS	Naganathan et al. (2008)
Canadian wheat	Wheat class	Reflectance	LCTF	960-1700	Quadratic DiscriminantAnalysis (QDA), ANN	Mahesh et al. (2008)
Cotton	Fiber micronaire	Reflectance	Optical bandpass filters	1450, 1550, 1600	Linear regression	Sui et al. (2008)
Wheat	Storage fungi, insect-damaged wheat kernels, midge-damaged wheat kernels	Reflectance	LCTF	1000 - 1600	Multivariate image analysis (MIA) based on PCA, K-means clustering	Singh et al. (2007), Singh et al. (2009), Singh et al. (2010a)
Maize	Kernel hardness	Reflectance	LCTF and Pushbroom	960-2498	partial least squares discriminant analysis (PLS-DA)	Williams et al. (2009)
Canadian western wheat	Sprout damage	Reflectance	Line-scan	1000 - 2500	PCA, PLS	Xing et al. (2009)
Apple	Starch index	Reflectance	Line-scan	1000 - 1700	PLS	Menesatti et al. (2009)
Blueberry	Foreign materials	Reflectance	NIR illuminator with monochrometer	1000 - 1600	Discriminant analysis	Sugiyama et al. (2010)

Sour skin can be serious in individual fields and storage rooms. Because onions are relatively resistant to *B. cepacia* prior to bulbing, infections usually begin in the field at the late stage in harvest. But losses often happen in stored onions. Bacteria can gain entrance to onions when onion tops are cut during harvest, or through other wounds on the neck and shoulder areas of onions, such as the wounds caused by the sand blowing by wind. Inoculum of *B. cepacia* also associated with contaminated water like rain and overhead irrigation (Schwartz and Mohan, 2008). At the early stage of an infection, the primary symptom of sour skin in the onion is a pale yellow decay in one to a few inner scales on the neck or shoulder area. There is often no exterior symptom initially except a softened neck. The rot will gradually develop into the entire scale and adjacent onion scales, as pale yellow to light brown decay. In advanced stages, one or a few inner bulb scales could be slimy and slip off from the onion bulb. When sour skin-infected onions are cut open, one or several inner fleshy scales often can be seen to be soft and have a water-soaked appearance.

Figure 2.4: An example of sour skin-infected onions

2.5 Bibliography

Ariana, D. P., Lu, R., Guyer, D. E., 2006. Near-infrared hyperspectral reflectance imaging for detection of bruises on pickling cucumbers. Computers and Electronics in Agriculture 53 (1), 60–70.

Bei, L., Dennis, G., Miller, H., Spaine, T., Carnahan, J., 2004. Acousto-optic tunable filters: fundamentals and applications as applied to chemical analysis techniques. Progress in Quantum Electronics 28 (2), 67–87.

Cogdill, R. P., Hurburgh Jr, C. R., Rippke, G. R., 2004. Single-kernel maize analysis by near-infrared hyperspectral imaging. Transactions of the American Society of Agricultural Engineers 47 (1), 311–320.

Davies, E., 2009. The application of machine vision to food and agriculture: a review. Imaging Science Journal, The 57 (4), 197–217.

Evans, M., Thai, C., Grant, J., 1998. Development of a spectral imaging system based on a liquid crystal tunable filter. Transactions of the ASAE 41 (6), 1845–1852.

Gat, N., 2000. Imaging spectroscopy using tunable filters: A review. Proceedings of SPIE 4056, 50–64.

Gowen, A. A., O'Donnell, C. P., Cullen, P. J., Downey, G., Frias, J. M., 2007. Hyperspectral imaging - an emerging process analytical tool for food quality and safety control. Trends in Food Science & Technology 18 (12), 590–598.

International Organization for Standardization, 2007a. ISO International Standard 20473: specifies the division of optical radiation into spectral bands for optics and photonics.

International Organization for Standardization, 2007b. ISO International Standard 21348: Space environment (natural and artificial) process for determining solar irradiances.

Kerekes, J. P., Schott, J. R., 2007. Hyperspectral Imaging Systems. Wiley-Interscience, Hoboken, N.J., Ch. 2, pp. 19–45.

Kim, M. S., Chen, Y. R., Mehl, P. M., 2001. Hyperspectral reflectance and fluorescence imaging system for food quality and safety. Transactions of the American Society of Agricultural Engineers 44 (3), 721–729.

Lu, R., Chen, Y.-R., 1998. Hyperspectral imaging for safety inspection of food and agricultural products. Proceedings of SPIE - The International Society for Optical Engineering 3544, 121–133.

Mahesh, S., Manickavasagan, A., Jayas, D. S., Paliwal, J., White, N. D. G., 2008. Feasibility of near-infrared hyperspectral imaging to differentiate canadian wheat classes. Biosystems Engineering 101 (1), 50–57.

Menesatti, P., Zanella, A., D'Andrea, S., Costa, C., Paglia, G., Pallottino, F., 2009. Supervised multivariate analysis of hyper-spectral NIR images to evaluate the starch index of apples. Food and Bioprocess Technology 2 (3), 308 – 314.

Miller, J. L., 1994. Principles of infrared technology: A practical guide to the state of the art. Kluwer Academic Pub.

Naganathan, G. K., Grimes, L. M., Subbiah, J., Calkins, C. R., Samal, A., Meyer, G. E., 2008. Visible/near-infrared hyperspectral imaging for beef tenderness prediction. Computers and Electronics in Agriculture 64 (2), 225–233.

Nicolai, B. M., Beullens, K., Bobelyn, E., Peirs, A., Saeys, W., Theron, K. I., Lammertyn, J., 2007. Nondestructive measurement of fruit and vegetable quality by means of NIR spectroscopy: A review. Postharvest Biology and Technology 46 (2), 99–118.

Nicolai, B. M., Lotze, E., Peirs, A., Scheerlinck, N., Theron, K. I., 2006. Non-destructive measurement of bitter pit in apple fruit using NIR hyperspectral imaging. Postharvest Biology and Technology 40 (1), 1–6.

Schwartz, H. F., Mohan, S. K., 2008. Compendium of onion and garlic diseases and pests, 2nd Edition. Disease compendium series of the American Phytopathological Society. APS Press, American Phytopathological Society, St. Paul, Minn.

Singh, C. B., Jayas, D. S., Paliwal, J., White, N. D., 2010a. Detection of midge-damaged wheat kernels using short-wave near-infrared hyperspectral and digital colour imaging. Biosystems Engineering 105 (3), 380 – 387.

Singh, C. B., Jayas, D. S., Paliwal, J., White, N. D. G., 2007. Fungal detection in wheat using near-infrared hyperspectral imaging. Transactions of the ASABE 50 (6), 2171–2176.

Singh, C. B., Jayas, D. S., Paliwal, J., White, N. D. G., 2009. Detection of insect-damaged wheat kernels using near-infrared hyperspectral imaging. Journal of Stored Products Research 45 (3), 151–158.

Singh, C. B., Jayas, D. S., Paliwal, J., White, N. D. G., 2010b. Identification of insect-damaged wheat kernels using short-wave near-infrared hyperspectral and digital colour imaging. Computers and Electronics in Agriculture 73 (2), 118–125.

Slawson, R., Ninkov, Z., Horch, E., 1999. Hyperspectral imaging: wide-area spectrophotometry using a liquid-crystal tunable filter. Publications of the Astronomical Society of the Pacific 111, 621–626.

Sugiyama, T., Sugiyama, J., Tsuta, M., Fujita, K., Shibata, M., Kokawa, M., Araki, T., Nabetani, H., Sagara, Y., 2010. NIR spectral imaging with discriminant analysis for detecting foreign materials among blueberries. Journal of Food Engineering 101 (3), 244 – 252.

Sui, R., Thomasson, J. A., Ge, Y., Morgan, C., 2008. Multispectral sensor for in-situ cotton fiber quality measurement. Transactions of the ASABE 51 (6), 2201–2208.

Tran, C. D., 2005. Principles, instrumentation, and applications of infrared multispectral imaging, an overview. Analytical Letters 38 (5), 735–752.

Wang, W., Paliwal, J., 2007. Near-infrared spectroscopy and imaging in food quality and safety. Sensing and Instrumentation for Food Quality and Safety 1, 193–207.

Williams, P., Geladi, P., Fox, G., Manley, M., 2009. Maize kernel hardness classification by near infrared (NIR) hyperspectral imaging and multivariate data analysis. Analytica Chimica Acta 653 (2), 121 – 130.

Williams, P., Norris, K., Norris, K. H., 2001. Near-infrared technology: in the agricultural and food industries, 2nd Edition. American Association of Cereal Chemists, St. Paul, Minn., USA.

Xing, J., Van Hung, P., Symons, S., Shahin, M., Hatcher, D., 2009. Using a short wavelength infrared (SWIR) hyperspectral imaging system to predict alpha amylase activity in individual canadian western wheat kernelsbi. Sensing and Instrumentation for Food Quality and Safety 3 (4), 211–218.

Chapter 3

Development and Calibration of an LCTF-based Shortwave Infrared Spectral Imaging System for Food Quality Inspection

3.1 Overview

The liquid crystal tunable filter (LCTF) based spectral imaging is an important branch in spectral imaging. Recently, there has been an increasing need of high performance LCTF-based spectral imaging systems for food safety and quality inspections. This chapter thoroughly demonstrates the design, hardware selection and the integration of an LCTF-based shortwave infrared (SWIR) spectral imaging system. A series of tests were conducted to calibrate the linearity of the system output, measure the field of view of the spectral imager, level the system spectral sensitivity, test the spatial and spectral resolution of the system, correct the image distortion, and reduce the spectral noise of the system output. Results of these calibration tests showed that the system satisfied the design criteria in both spatial and spectral domains. As a validation test, the system was used to capture the hyperspectral images of water, 95% ethanol, sugar, and wheat flour in the SWIR region. The results of the validation test demonstrated that the SWIR spectral imaging can be used to differentiate these four materials. This LCTF-based shortwave infrared spectral imaging system can be used for nondestructive inspections that require fast selections of spectral bands and images of high quality.

3.2 Introduction

Spectral imaging is a rapid growing area in food safety and quality nondestructive inspection. By capturing images of the test object at a number of narrow wavelength bands nonde-

structively, spectral imaging offers a wealth of spatial and spectral information of the scene imaged. Spectral images can be used to ascertain the intrinsic interrelationships between spatial/spectral observations and physical/chemical properties of the measured objects (Lu and Chen, 1998). Currently, spectral imaging often refers to hyperspectral imaging (HSI), which acquires images at hundreds of contiguous spectral bands. Spectral imaging that uses a small number of discrete spectral bands (<10) is often called multispectral imaging (MSI). In the last decade, spectral imaging has gained recognition in food safety and quality inspection due to its nondestructive inspection capability. Its sensing capabilities have been demonstrated by numerous applications reported for a broad range of food and agricultural products such as poultry (Chao et al., 2010; Yoon et al., 2010), beef (Naganathan et al., 2008), wheat (Singh et al., 2010), apple (ElMasry et al., 2008; Kim et al., 2008), citrus (Qin et al., 2009) and cucumber (Ariana and Lu, 2009).

In food safety and quality inspection, two most common spectral imaging configurations are: (I) the system uses an imaging spectrograph with the thin line aperture as the line scanner, and moves the scanner (known as line-scan) or moves the test object (known as pushbroom acquisition) during scanning, and (II) the ETF-based system which uses the ETF to select wavelength bands and takes 2-D images over time (Gowen et al., 2007). To make the statement concise, this paper uses the term line-scan to represent the line-scan and pushbroom spectral imaging configurations. In multispectral imaging, reported systems mainly used interference filter (Yang et al., 2005), interchangeable filters (Kise et al., 2010) or electronically tunable filters (ETFs) (Peng and Lu, 2006). Recently, researchers started to use the imaging spectrograph to build the multispectral imaging system in which only image data at a number of key wavelengths was processed and used (Chao et al., 2010).

In hyperspectral imaging, the line-scan system has been predominantly used for food safety and quality inspection due to its high speed and high spectral resolution. Another cause for the popular use of the line-scan HSI is that, compared to stationary area imaging, the line-scan technique is easier to be integrated with the current online inspection systems using a

conveyor belt. As for the ETF-based spectral imaging, liquid crystal tunable filters (LCTF) and acousto-optical tunable filters (AOTF) are the two most commonly used wavelength selection methods (Gowen et al., 2007). The LCTF-based systems are relatively slower than the systems using AOTFs, but they have better imaging performance since LCTFs have larger apertures, relatively wider field of view, and lower wavefront distortions than AOTFs Evans et al. (1998). Thus, the LCTF-based system is the mainstream for the ETF-based spectral imaging.

Methods for calibrating the line-scan/pushbroom spectral imaging system have been well-developed and presented in the literature. Polder and Van der Heijden (2001) discussed the calculation method for quantifying the sensitivity and SNR of a spectrograph. Lawrence et al. (2003) demonstrated a general procedure for calibrating a pushbroom spectral imaging system and attributed an image distortion correction approach of using geometric control points. Details of spectral/spatial accuracy and resolution calibration, and CCD responsitivity calibration methods can be found in Mehl et al. (2004) and Kim et al. (2001). Moreover, some advanced calibration techniques for the line-scan/pushbroom spectral imaging system have been explored, such as spectral and spatial repeatability of HSI (Peleg et al., 2005) and noise reduction (Shafri and Yusof, 2009). Egloff et al. (2009) conducted a thoroughly analysis of grating-induced spectral and spatial distortion for a near-infrared pushbroom hyperspectral imager.

Compared with the widely employed and much studied line-scan hyperspectral imaging technologies (Chao et al., 2010; Gowen et al., 2007; Lawrence et al., 2003; Park et al., 2002; Kim et al., 2001), the LCTF-based hyperspectral imaging has been less studied for food safety and quality inspection in the past decade. Although there are some similarities between the LCTF-based spectral imaging system and the line-scan spectral imaging system, developing an LCTF-based spectral imaging system requires many special considerations on system design, integration, and calibration. For instance, an LCTF-based spectral imaging system can alter the camera exposure time over wavelength bands to correct system spec-

tral sensitivity while a line-scan system can only use a fixed camera exposure time for all wavelengths during one scan. Gat (2000) summarized the most fundamental principles of designing a tunable filters based spectral imaging system, with an example of integrating an LCTF-based hyperspectral imaging system. In food safety and quality inspection, Evans et al. (1998) demonstrated an LCTF-based spectral imaging system for studying plant health, and introduced a calibration approach of leveling system response by linear and logarithmic methods. Archibald et al. (1999) developed an LCTF-based spectral imaging system to differentiate color class of wheat kernels. Cogdill et al. (2004) reported an LCTF-based HSI system for predicting the concentrations of maize kernels' constituents by the hyperspectral transmittance imaging. Williams et al. (2009) evaluated the maize kernels hardness by using both LCTF-based and line-scan HSI imaging systems. Singh et al. (2007, 2010) used the LCTF-based spectral imaging for detecting fungal contamination in wheat and identifying insect-damaged wheat kernels. Nonetheless, the development and calibration of the LCTF-based spectral imaging systems were seldom discussed in depth in these papers.

So far, the majority of the reported LCTF-based spectral imaging systems were designed in the spectral range of 400 - 1100 nm. However, there have been increasing interests of SWIR spectral imaging for food safety and quality inspection (Wang and Paliwal, 2007). In fact, designing an LCTF-based SWIR spectral imaging system requires many special considerations on lens selection, illumination, and system calibration. To our knowledge, methodologies for designing an LCTF-based spectral imaging system in SWIR (900 - 1700 nm) have been rarely demonstrated in detail in food safety and quality inspection. Particularly, the calibration process of an LCTF-based SWIR spectral imaging system was seldom demonstrated in the literature.

This paper demonstrates the methodologies that were used for the design, development, calibration, and characterization of an LCTF-based SWIR spectral imaging system. The main objective of this work was to incorporate the state-of-the-art technologies to develop and calibrate an LCTF-based spectral imaging system for acquiring shortwave infrared spectral

images. The system was designed to operate in dual-mode (HSI and MSI). The specific objectives of this work were to:

- Design a dual-mode spectral imaging system to capture either hyperspectral or multispectral images in the spectral region of 900 - 1700 nm.
- Develop a data acquisition software program to integrate the system for SWIR hyperspectral and multispectral image acquisition.
- Calibrate and characterize the system, including calibrating the linearity of system output, measuring field of view, leveling system spectral response, testing spatial and spectral resolution, and calibrating the lens distortion, etc.

3.3 Shortwave infrared LCTF-based spectral Imaging System

3.3.1 System design criteria and architecture

The spectral imaging system was designed for nondestructive safety and quality inspection of food and agricultural products. The system was designed to be used for indoor inspections. Therefore, the fundamental design criterion for the system was that it must be able to capture spectral images of the test object accurately and completely in a distance of 0.5-1.5 m. Specific design criteria for the system were: (1) accurate spectral response and good image resolution, (2) use in indoor environment, (3) high signal to noise ratio, (4) minimal response time, and (5) high extensibility.

A successful spectral imaging system requires a deliberate design, proper selections of hardware components, good integration and functional software. Figure 3.1 shows the overall architecture of the LCTF-based spectral imaging system. The system was designed on a multi-tier architecture so that functional modules are logically separated and reusable. The system consists of five independent logical tiers including hardware (2 tiers) and software (3 tiers). The bottom tier includes the spectral imager and the illumination system. The next tier consists of a computer and two I/O hardware interfaces which connect the spectral

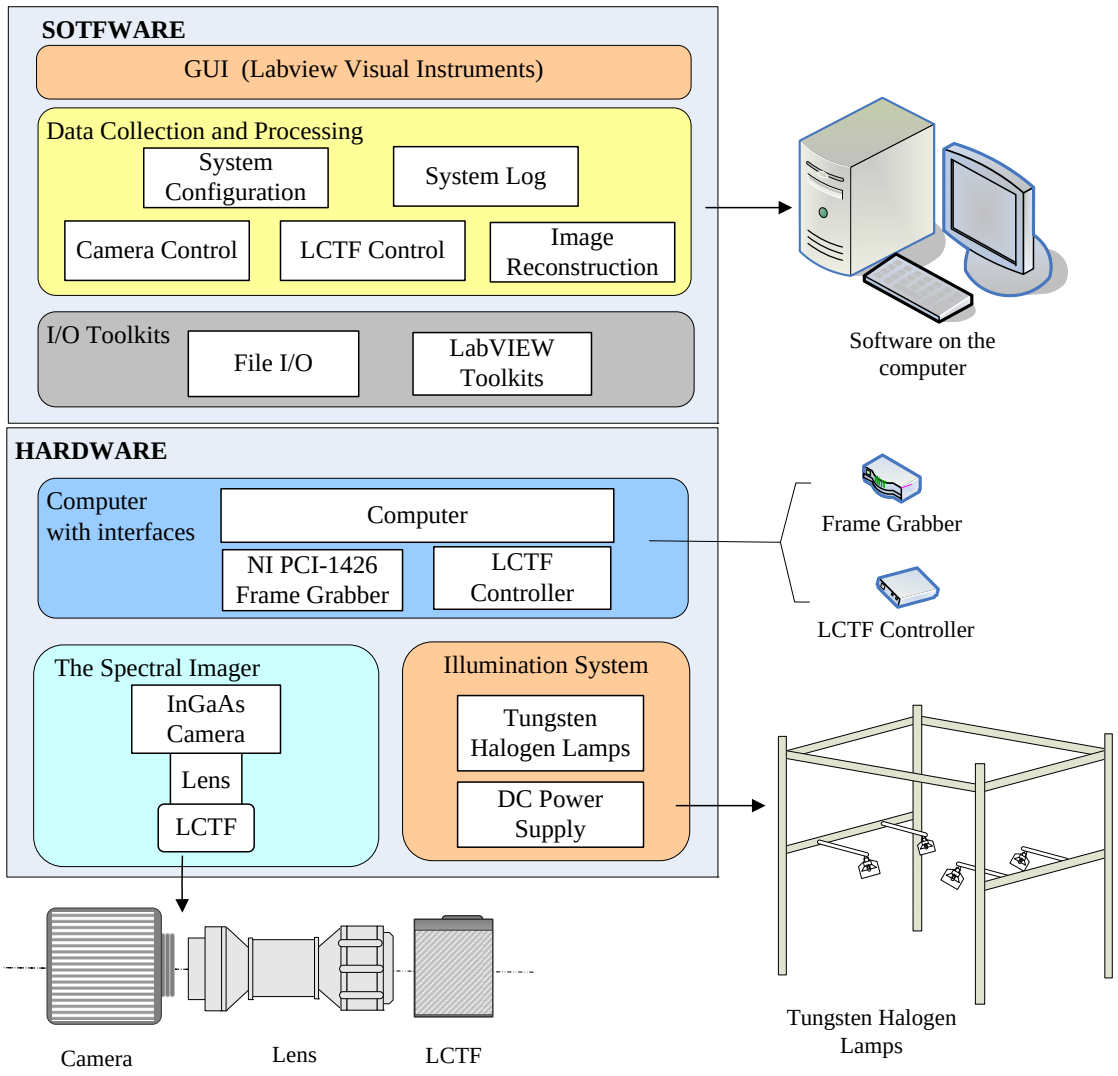

Figure 3.1: The architecture of the LCTF-based spectral imaging system

imager and the computer. The top three layers provide a 3-tier architecture for software. The top three layers takes care of data I/O between software and hardware, handles data process, and provides graphic user interface (GUI), respectively.

Physically, the system consists of a spectral imager, an illumination system, a frame grabber, a computer and data acquisition software. The key sensing unit is the SWIR spectral imager, which takes monochromatic images at specified wavelengths in the spectral

range of 900 - 1700 nm. The spectral imager was designed and fabricated with off-the-shelf commercial products: an LCTF (Model Varispec LNIR 20-HC-20, Cambridge Research & Instrumentation, MA, U.S.A), an InGaAs camera (Model SUI320KTS-1.7RT, GOODRICH, Sensors Unlimited, Inc, NJ, U.S.A) and a lens (Model SOLO 50, GOODRICH, Sensors Unlimited, Inc, NJ, U.S.A). The illumination system used four quartz-halogen lamps to provide a SWIR light source for the system. The configuration of the illumination system is adjustable and should be customized and optimized based on the specific requirements of the applications. The data acquisition software was developed using the LabVIEW graphical programming language (National Instruments, Austin, TX, U.S.A).

3.4 Hardware selection and configuration

Design of an LCTF-based spectral imaging system is a comprehensive process of selecting optical and electrical components, and determining the optimal configuration for the system. The primary strategy for designing this system was to select the state-of-the-art and reliable products. Moreover, only off-the-shelf commercial products were considered to restraint the cost and time for developing the system.

3.4.1 The LCTF-based Spectral Imager

3.4.1.1 The Computation Model of the LCTF-based Spectral Imager

The fundamentals of the LCTF-based spectral imaging are based on the interactions between the light and the test matter. When the light interacts with the test object, the ratio of the reflected, scattered or transmitted light to the incident light is a function of wavelength (λ). In spectral imaging, this function is depicted as the spectrum in spectral domain. Figure 3.2 shows the schematic view of the LCTF-based spectral imaging. In LCTF-based spectral imaging, when light (S(λ)) passes through the LCTF, light energy is filtered based on the overall transmission of the LCTF ($\tau_{TF}(\lambda)$). A convergent lens, which is usually placed behind or before the LCTF, also absorbs and blocks part of light energy ($\tau_{Lens}(\lambda)$). The focal plan

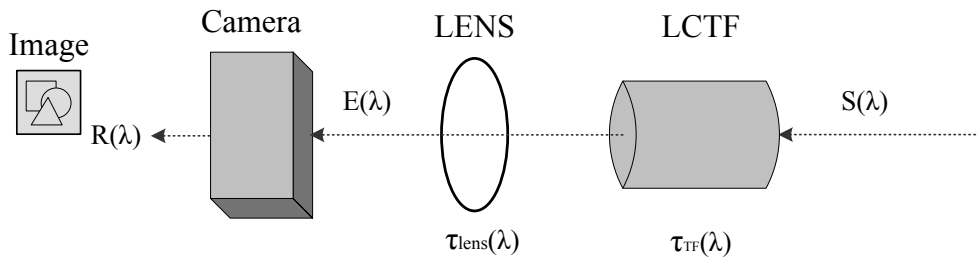

Figure 3.2: The schematic of the LCTF-based spectral imaging

array (FPA) of the camera detects the level of light energy (E(λ)) and then generates the analog signal accordingly. The analog signal, consequently, is converted to digital counts by the analog-to-digital conversion (ADC). The digitized data provides the pixel intensity values of the monochrome images, which are the outputs of the spectral imager. By simplify a 2-D image to one pixel, the following equation can be obtained:

$$E(\lambda) = S(\lambda)\tau_{TF}(\lambda)\tau_{Lens}(\lambda) \tag{3.1}$$

To derive the computational mode of the LCTF-based spectral imaging, we start from a spectral sensitivity model used by Lopez-Alvarez et al. (2008), which was originally derived from a conventional camera sensitivity model given by Ferrero et al. (2006):

$$R(\lambda) = \frac{C^c}{E(\lambda)t_{exp}} \tag{3.2}$$

Where (R(λ)) refers to the responsivity of the spectral imager, C^c is the pixel value after eliminating noise and uniformity correction, E(λ) is the original radiance received by the camera FPA, and t_{exp} is the camera exposure time. Since the camera exposure time is also adjustable as a function of wavelength, the t_{exp} should be extended to $t_{exp}(\lambda)$. Thus, the equation 3.2 is rewritten as:

$$R(\lambda) = \frac{C^c}{E(\lambda)t_{exp}(\lambda)} \tag{3.3}$$

In hyperspectral imaging, a wide-used method for removing noise and correcting the camera uniformity is the flat field correction, which converts the original radiance image (I_r) to a corrected percentage image by using the reference image of a uniform diffuse white target (I_w) and the dark current image (I_d). The corrected image (C^c) is calculated as follows:

$$C^c = k\frac{(I_r - I_d)}{I_w - I_d} \tag{3.4}$$

Where k is the reflectance rate of the white reference target. In practical, the coefficient k is also wavelength-dependant. So, it should be extended to $k(\lambda)$. Using the Eqs. 3.1, 3.3 and 3.4, the computational model for the LCTF-based spectral imager can be obtained:

$$R(\lambda) = \frac{k(\lambda)(I_r - I_d)}{(I_w - I_d)S(\lambda)\tau_{TF}(\lambda)\tau_{Lens}(\lambda)t_{exp}(\lambda)} \tag{3.5}$$

Where $R(\lambda)$ depicts the responsivity of the system, and $I_r, I_w, and I_d$ are the 2-D images of the test object, the white reference, and the dark current at the wavelength number $k(\lambda)$, respectively.

3.4.1.2 Hardware Selection and Integration

The detector (camera) was the first item selected for this system. Generally, two types of high performance photodiode detectors are used for the SWIR imaging: the indium gallium arsenide (InGaAs) sensor and the mercury cadmium telluride (HgCdTe) sensor (Becker and Huntsville, 2005). Both InGaAs and HgCdTe sensors were originally developed for the high performance military applications and have high quantum efficiency. The HgCdTe detectors cover a very broad infrared range, but they need to be operated at a high temperature and are very expensive. In the SWIR region up to 1700 nm, the standard InGaAs sensor or the InGaAs with indium phosfide substrate (InGaAs/InP) sensor can achieve close performance with the HgCdTe sensors (Becker and Huntsville, 2005), while their costs are much lower than HgCdTe sensors. At present, the InGaAs sensors are still the most mature and practical products for inspections in the SWIR region. Thus, our system used a standard InGaAs SWIR camera produced by Sensors Unlimited, Inc (SUI). The camera has a solid state

InGaAs FPA of 320 × 256 pixels with 25 m pitch. It has high response from 900 nm to 1700 nm and provides a number of useful functions such as the on-board non-uniformity correction, predefined corrected camera configuration modes and a programmable startup configuration. Since the camera uses a 12-bit digital Camera Link compatible output, a NI PCI-1426 frame grabber is used to acquire monochromatic images in a 60 frames per second (fps) frame rate.

Selection of an LCTF was straightforward since only limited off-the-shelf LCTF products were available. The aperture size of the LCTF is an essential parameter that could affect the performance of the system. Generally, a large aperture LCTF was preferred when the LCTF is placed at the front of the spectral imager so that more light can pass through. However, to the date that the system was completed, the largest working aperture of the LCTFs in the SWIR range was 20 mm. The LCTF used by the system consists of an optic module and an electronics controller module. The controller module is linked to the computer through a USB interface and connected with the optic module by a serial cable. The controller receives serial commands from the computer and control the LCTF to tune wavelength over the spectral region from 850 nm to 1800 nm with Full-Width at Half-Maximum (FWHM) 20 nm.

The lens is the most critical optics component that could affect the performance of the system. Before calculating the required parameters of a lens, it is important to first determine the assembly order of the three key components of the imager: the camera, the LCTF and the lens. Different assembly layouts have different requirements for the features of the lens. Figure 3.3 shows two possible layouts of an LCTF-based spectral imager. The lens could either be placed between the LCTF and the camera (layout I), or be put in the front of the spectral imager (layout II). In layout I, light passes through the LCTF and then converges to the detector. Because light would easily be blocked by the LCTF, this integration layout requires a relatively large aperture LCTF to avoid severe mechanical vignetting.

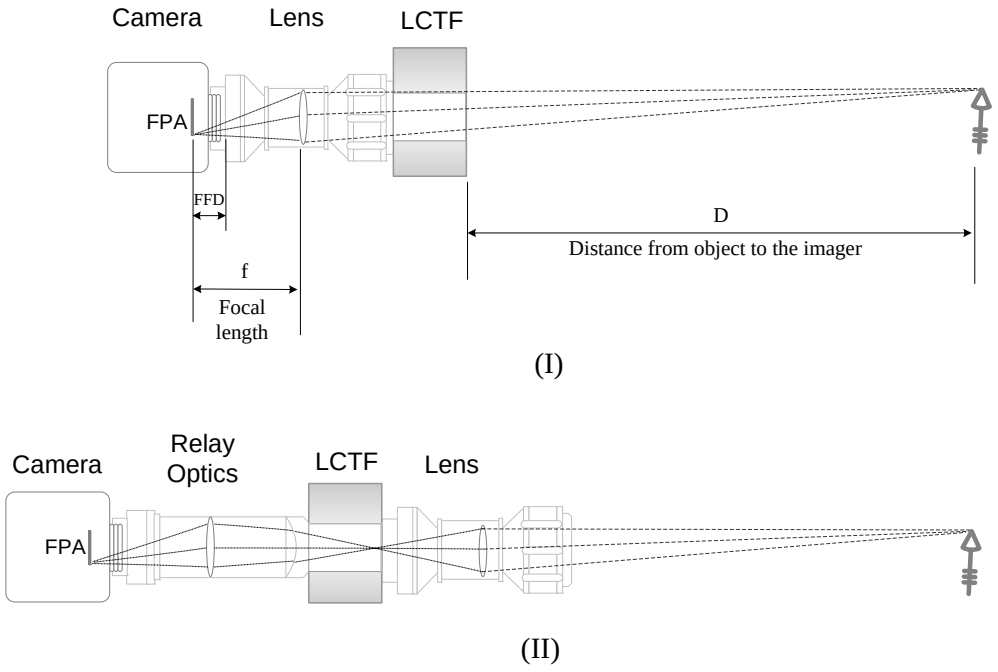

Figure 3.3: Schematic of two typical layouts for the LCTF-based spectral imager to integrate camera, lens, and LCTF: (I) the lens is mounted between the LCTF and the camera, and (II) the lens is placed in the front of the imager, and uses relay optics to focus the image of the test object on the camera FPA.

When the lens is placed in the front of the imager, it must have a long flange focal distance (FFD) to focus the object on the FPA of the camera. The FFD of a lens, which is determined by the lens' mount type, is the distance between the lens rear flange and the focal plane of the camera. Appendix A lists the designed the FFDs of several common lens mount types. In this system, the thickness of the LCTF is 49.5 mm and the default camera mount type is M42. Thus, both the FFD and the effective focal length (f) of the lens must be larger than 49.5 mm if it is placed in the front of the imager. Since the majority of off-the-shelf high performance SWIR lenses can't meet this requirement, a relay optics is often used to extend the focal length and the FFD of the lens, as shown in figure 3.3 layout II. This arrangement, nevertheless, requires a comprehensive optical design and would greatly increase the complexity, size and constructing cost of the imager. Therefore, in this system, the first configuration (layout I in figure 3.3) was used.

Once the layout of the spectral imager was determined, decisions regarding detailed parameters and characteristics of the lens were made. This design process was started by calculating the field of view (FOV) and the magnification (M). This system was designed for the purpose of the quality inspection of onions in postharvest. Therefore, the expected optimal FOV was 187.5 mm × 150 mm which covered a single bulb of most onions. The camera FPA is a 8.0 mm × 6.4 mm plane of a 320 × 256 pixel array, and it has a pixel size (pixel pitch) 6.4 mm/256 = 0.025 mm. Thus, with the expected FOV, the resolution of the image should be 256 dots/150 mm = 1.7 dots per mm (about 43 dpi or 0.85 lp/mm). Thus, the expected image resolution was 1 lp/mm. The magnification was predicted as the ratio of the FOV and the camera sensor size, which was 150 mm/6.4 mm = 23.4.

The expected focal length (f) of the lens was calculated based on the estimated FOV, the magnification, and the object-to-camera distance (D). As shown in figure 3.4, the lens focal distance could be predicted using a pin-hole lens model by f = D/(M-2). Since the expected object-to-camera distance was 0.5 - 1.5 m, the focal length of the lens could be a value between 24 mm and 70 mm. For an LCTF-based SWIR spectral imaging system,

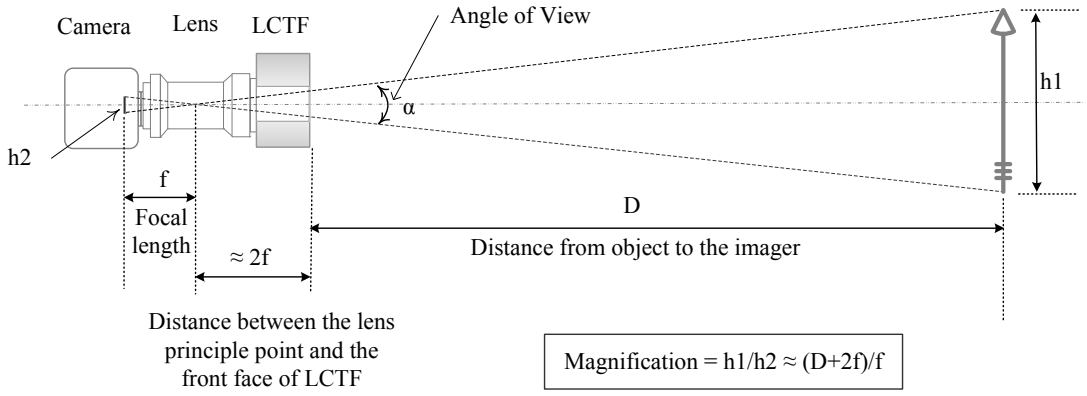

Figure 3.4: Pin-hole optical model of the LCTF-based spectral imaging system for estimating lens parameters.

nevertheless, the angle of view (α) of the system could be affected by the LCTF. Due to its relatively small aperture, the LCTF could block light and cause vignetting problems on images. A lens with a large focal length can mitigate the vignetting problem. But a lens with a large focal length will require a longer object-to-camera distance due to its small angle of view. Therefore, selecting the right focal length of the lens was to make a tradeoff between guaranteeing the image quality, maximizing the angle of view, and minimizing image vignetting.

To accurately evaluate the optimal focal length of the lens, an experimental test was conducted using a manual zoom lens (model Fuji H6x12.5R, Fujinon, NJ, USA), which has an adjustable focal length of 12.5 - 75 mm. A test pattern was designed to indicate the FOV of the system. The size of the pattern was 200 mm $\times$ 200 mm and it was printed on an A4 size paper as the test target. The target was placed on a 500 mm $\times$ 500 mm Teflon sheet to get a white background. The distance between the target and the front of the spectral imager was 1.5 m. Four 35 watt quartz halogen lamps were used to illuminate the test target. Figure 3.5 shows the test pattern and its images taken at different focal lengths (35 mm, 50 mm,

and 75 mm) at 1100 nm. All images were quite blurry because this lens was designed for the use in visual range. The image taken at the 35 mm focal length had a large field of view but with a severe vignetting problem. The FOV was larger than the target size (200 mm $\times$ 200 mm) but only the middle area of the camera FPA was effective. The image of using 50 mm focal length indicated that most pixels of the camera FPA were effective and the image covered an area larger than 200 mm $\times$ 160 mm. The vignetting effective (four relative dark corners in the image) was moderate. When the focal length of the lens increased to 75 mm, the vignetting effective was further mitigated whereas the FOV of the system shrunk to 150 mm $\times$ 120 mm, which was much smaller than the expected FOV. Therefore, the lens of 50 mm focal length was considered as a tradeoff between a larger FOV and less vignetting effect in images.

Several additional important aspects were considered to meet the special requirements of the SWIR LCTF-based spectral imaging. First, taking into considerations of relatively low throughput of LCTF, a fast lens (a large aperture or a small f-number) was preferred so that more light can pass. In addition to the numerous NIR or SWIR lenses, using off-the-shelf commercial VIS glass lenses is also feasible since light at the SWIR range can readily pass through glass. However, coating of a lens is another important but easily neglected factor. Generally, antireflective coatings on most lenses are optimized for visible light, and these lenses often have a larger reflectivity and poor throughput in the SWIR region. Thus, it's important to ascertain that the coating of the lens is optimized for the correct spectral region. Moreover, a wide-angle lens is not recommended because it would cause remarkable image distortion. Another critical consideration is related to the optical phenomenon named "axial chromatic aberration". As for a converging lens, light beams at different wavelengths have different refractive indexes. Therefore, when the wavelength of light changes, the focus point of the lens shifts too, leading to blurred images (Smith, 2008). For a spectral imaging system, it's essential to reduce chromatic aberration to avoid spectral distortion. Although it is feasible to use image processing methods to reduce axial chromatic aberration (Wang

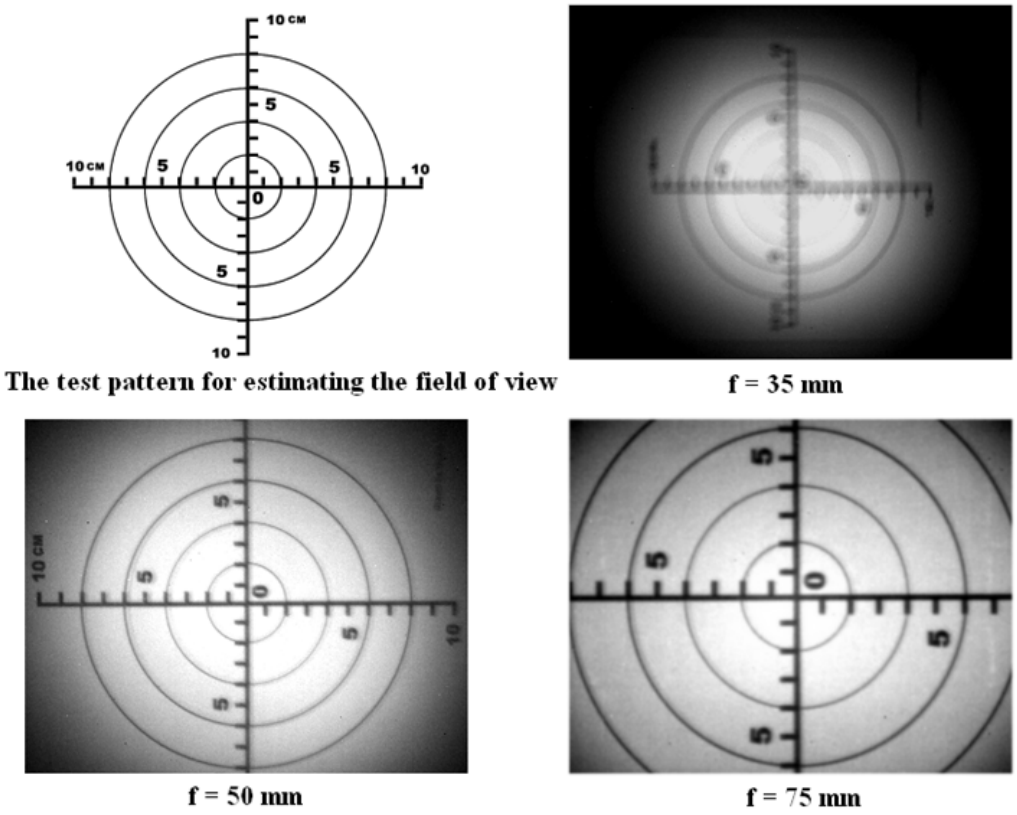

Figure 3.5: A test pattern for measuring the system field of view and its images at 1100 nm. Images were taken when the focal length of the lens was 35 mm, 50 mm, and 75 mm.

et al., 2006), the optical techniques such as using achromatic doublet are the most reliable and effective approach to correct the chromatic aberration. Therefore, although the initial investment would be higher, a lens that has been chromatically corrected over the interested spectral region is a key factor for the success of an LCTF-based SWIR spectral imaging system. In summary, a 50mm F/1.4 SWIR lens (Model SOLO 50, GOODRICH, Sensors Unlimited, Inc, NJ, U.S.A) was selected for the system. The lens has been optimized for the spectral region from 900 nm to 1700 nm, and has a minimum 90% throughput in the spectral region from 900 nm to 1700 nm. Two step-up ring adapters (47 mm - 52 mm, 52 mm - 55 mm) were also used to attach the LCTF to the lens. A detailed performance comparison between this SWIR lens and other lens has been reported by Hansen (2009).

3.4.2 The Illumination System

The illumination system was another major design challenge in hardware. An ideal illumination should provide the stable, constant spectral output, and the uniform lighting on the area of interest. Although the illumination unit should be customized for each specific application, some general issues need to be taken into consideration for an LCTF-based spectral imaging system. For the spectral imaging systems in the visual and NIR/SWIR region, tungsten halogen lamps are the most common and suitable light sources which have been widely used, as they could provide stable and continuous spectral output (Wang and Paliwal, 2007). In addition, a stabilized DC power supply is always necessary to keep the light output constant. However, it has to be noted that real spectral output of different brands' lamps are often distinct. Moreover, since the halogen lamp emits a board wavelength region of light, some optical filters can be used to block out the light in the spectral regions not of interests. However, it is not recommended to utilize a polarization filter for an LCTF-based spectral imaging system, since the LCTF is polarization sensitive (Gat, 2000).

The uniformity of the lighting was the major difficulty for designing a light unit for the system. Different from the line light in a line-scan spectral imaging system, the light

source in an LCTF-based spectral imaging system has to illuminate an area uniformly on a heterogeneous surface. A good strategy for achieving a good light uniformity is to use multiple lamps and arrange them meticulously with a suitable geometry. Some optic diffusers, reflectors and chambers with a white reflectance coating, can be also used to enhance the light uniformity. The MR lamp is a good light source for the LCTF-based spectral imaging since it is compact and provides directional area lighting. The multifaceted reflector (MR) halogen lamp uses a single-ended, quartz halogen filament capsule mounted within a pressed glass reflector. There are two important parameters for characterizing the light distribution of the MR lamp: the beam spread and the center beam candlepower (CBCP). The CBCP is the intensity emitted at the center of a directional lamp beam, which is determined by the lamp voltage and the beam angle (Paget et al., 2008). The beam spread is a beam angle that covers the illuminated area in which the beam intensity is 50% of the CBCP (figure 3.6). For the LCTF-based spectral imaging system, the beam spread of the lamp is determined by the expected lamp-to-object distance and the size of the illumination area. However, a lamp with a wide beam spread is generally preferred because it requires a relatively shorter lamp-to-object distance, which could reduce the need for the power of the lighting unit. In summary, this system used four 12V 35 watt MR16 halogen lamps (model S4121, Superior Lighting, FL, U.S.A), which have build-in reflectors and a front frosted lens to diffuse light. The lamps used by the system have 36° beam spread angle and the CBCP is 520 cd.

3.4.2.1 System hardware integration

Figure 3.7 shows the overall configuration of the system hardware. A dark chamber was fabricated to enclose the spectral imaging system. The chamber is a 600mm × 600mm × 2000 mm (L× W× H) box and the frame is composed by aluminum square tubes. A curtain and a top cover were made by the black commando cloth to completely block the outside ambient light. A heavy-duty camera mounting bracket is mounted on a 2 m long stainless steel tube with a diameter of 38.1 mm. The spectral imager is attached to the mounting

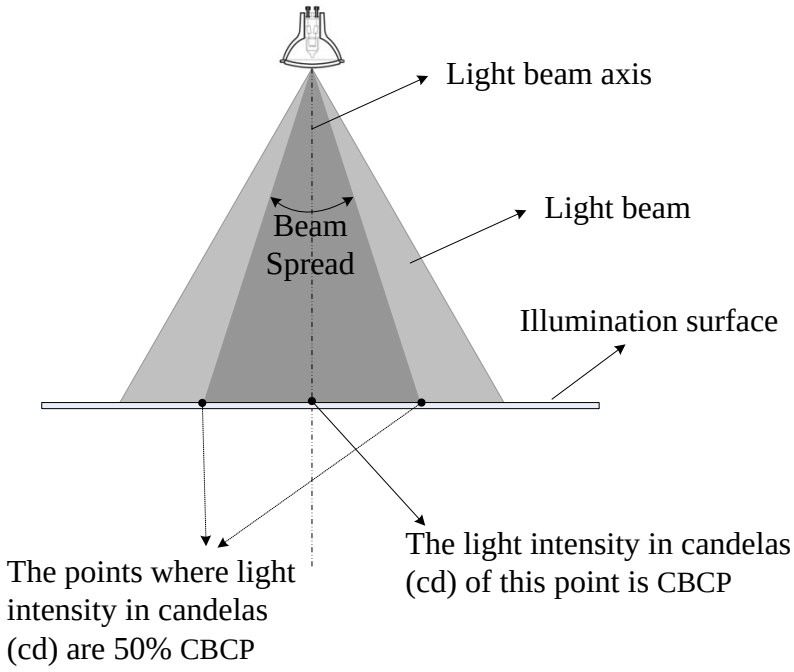

Figure 3.6: Illustration of the beam spread and the center beam candlepower (CBCP) of the MR16 halogen lamp

bracket by a customized mounting plate. The spectral imager can be moved up and down along the steel tube when the mounting bracket loosens from the steel tube. When the mounting bracket is fastened, the adjustment nob on the mounting bracket can be used to fine tune the position of the imager in a range of 0-100 mm.

Lamps were mounted on the horizontal aluminum beams to achieve good light projection angles. However, the setup of the illumination unit is flexible and could be optimized for specific application requirements. A tripod with a 3-way head was modified to be used as the sample stand, so that the distance between the sample and the spectral imager can be easily adjusted without moving the spectral imager. Moreover, the orientation of the test sample can be easily adjusted by using the 3-way head of the tripod.

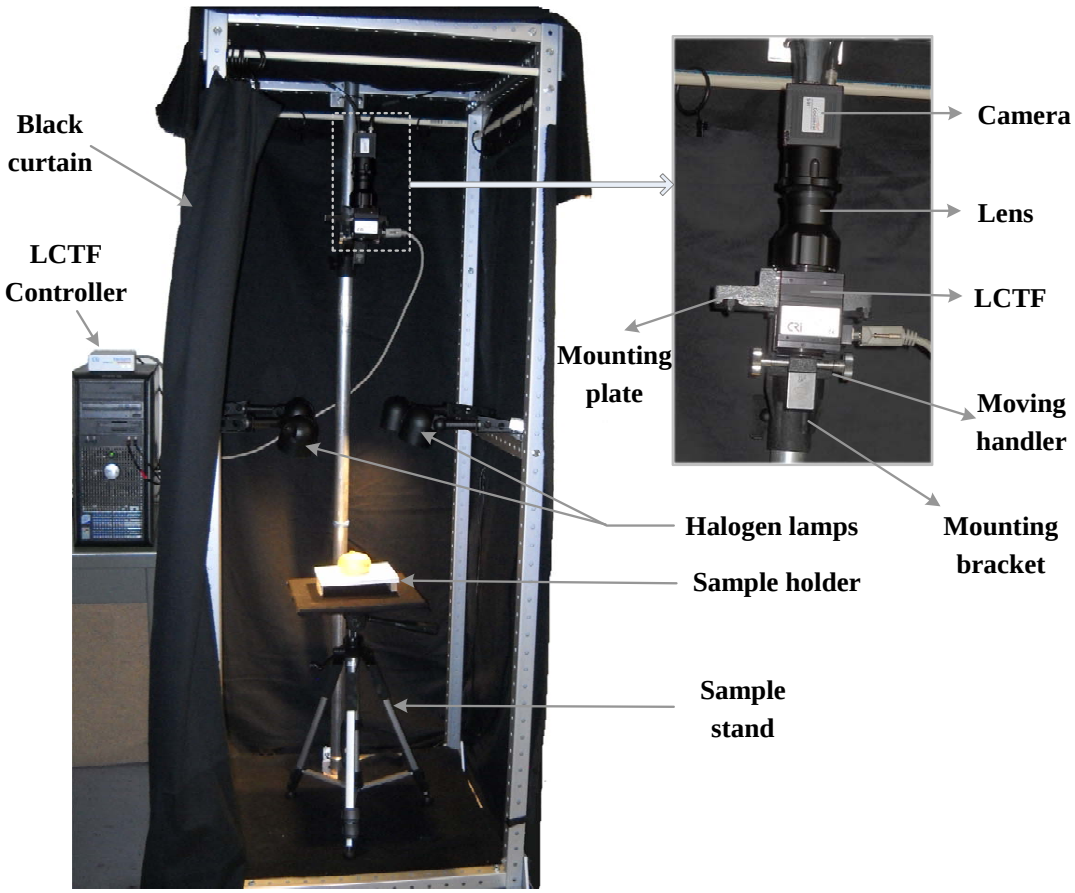

Figure 3.7: The hardware configuration of the LCTF-based spectral imaging system

3.5 Software Overview

A software program was developed to control the InGaAs camera and the LCTF to collect spectral images. The software was developed by using the LabVIEW graphical programming language. The advantages of the LabVIEW platform are its rich GUI components and capabilities for hardware control. The LabVIEW NI-IMAQdx toolkit provides a high level tool to control the InGaAs camera via the Camera Link interface. The VariSpec Software Developer Kit (SDK) (Cambridge Research & Instrumentation, MA, U.S.A) provides a set of LabVIEW sub-virtual instruments (sub-VIs), which were used for controlling the LCTF. The software comprised a main function module and a number of sub-modules, which were developed as LabVIEW sub-VIs. As shown in figure 3.1, the software modules were organized into three layers (hardware I/O, data collection and processing, and GUI) to maximize the reusability of modules and the flexibility of the software program. The lowest hardware communication layer sends commands and receives data from hardware components. The data collecting and processing layer contains all processing modules for hardware control, data collection, data processing, and system configuration. The GUI layer provides the graphic user interfaces of the system.

The software can be operated under two modes: hyperspectral imaging or multispectral imaging. Before starting a scan, the user selects the system operation mode (HSI or MSI), and set corresponding scan parameters. For a hyperspectral image acquisition, the user needs to specify the start and the end wavelength numbers of the spectral region to scan, and the spectral interval between bands in the spectral region. For a multispectral image acquisition, the user has to specify the band numbers of all wavelengths that need be scanned. The software also provides several advanced functions for operating the system, such as auto correction, auto naming, and selection of region of interest, etc. During the data acquisition, images at each band are displayed in the live preview window on the main GUI. The reconstructed hyperspectral or multispectral image file will be automatically named and saved into the pre-defined path.

3.6 System Calibration and Characterization

Since a spectral image records the spectral and image characteristics of the test object, it is essential that the system accuracy be guaranteed in both spectral and spatial domains. A well calibrated spectral imaging system has to test and calibrate all critical aspects that would affect the system performance, including wavelength accuracy, spectral sensitivity, spectral resolution, spectral linearity, spatial resolution, spatial contrast, the uniformity of field illumination, and lens functions etc.

For an LCTF-based spectral imaging system, all hardware components have to be regulated precisely before integration. Unfortunately, the fully calibration of all components individually requires spatial, spectral and optical tests with particular calibration tools, which is a formidable task that beyond the capability and scope of most laboratories. To simplify the calibration task to a manageable level, this LCTF-based spectral imager was treated as a single unit in calibration tests. Thus, the calibration tests treated the LCTF-based spectral imager as a "black-box", and didn't explicitly calibrate the camera, the lens and the LCTF separately. With this premise, the LCTF-based spectral imaging system was meticulously calibrated. Moreover, some essential parameters like the spatial and spectral resolution of the imager were also measured to characterize the performance of the system.

3.6.1 Image preprocessing

Before each calibration test, dark images of the system were measured by completely covering the optical entrance of the spectral imager. The dark images recorded the internal noise signal mainly caused by the dark current within the InGaAs camera. In all following calibration tests, dark images were measured and subtracted from the hyperspectral and multispectral images.

3.6.2 Calibration Tests in Spectral Domain

3.6.2.1 Spectral Accuracy

A pencil style krypton calibration lamp (model 6031, Oriel Instruments, Stratford, CT, USA) powered by an AC power supply (model 6045, Oriel Instruments, Stratford, CT, USA) was scanned to test spectral accuracy. The lamp was scanned in the spectral region of 900 nm - 1700 nm with 1 nm intervals. The lamp was scanned three times and the three hyperspectral images were averaged. A square ROI was selected on the averaged lamp image to cover the lamp light tube area. The mean spectrum of the lamp light tube was calculated from the extracted data. Figure 3.8 shows the spectra of the krypton calibration lamp measured by this system and the spectra provided by the lamp manufacturer. The wavelength location values of eight spectrum peaks (975, 1182, 1318, 1363, 1443, 1475, 1528, and 1685 nm) were identified and compared to the known krypton spectrum published by Sittner and Peck (1949) and the spectrum provided by the lamp manufacturer (Newport, 2010).

Generally, the spectrum of the krypton lamp measured by this LCTF-based spectral imaging system matched the published krypton spectrums accurately. Due to the 20 nm bandwidth of the system, spectral peaks were shown as crests instead of straight lines. The peaks at wavelength 975 nm, 1363 nm, and 1443 nm precisely matched the krypton lamp spectral datasheet published by the lamp manufacturer. Since the spectral datasheet of the lamp manufacture didn't provide corresponding data, peaks at wavelength 1182 nm, 1318 nm, and 1475 nm were compared to the krypton spectrum published by Sittner and Peck (1949), and the location errors of these three wavelength peaks were less than 1 nm. Two peaks (1528 nm and 1689 nm) showed obvious deviations from the published krypton spectrum. These deviations were caused by the relatively large bandwidth of the system (20 nm) and the short location distance between the two peaks, which resulted in a combination of two spectral crests. Thus, the strong spectral peaks at 1528 nm and 1689 nm can be interpreted as the combinations of wavelength peak pairs of 1523.9 nm and 1533.4 nm, 1678.5 nm and 1689 nm, respectively.

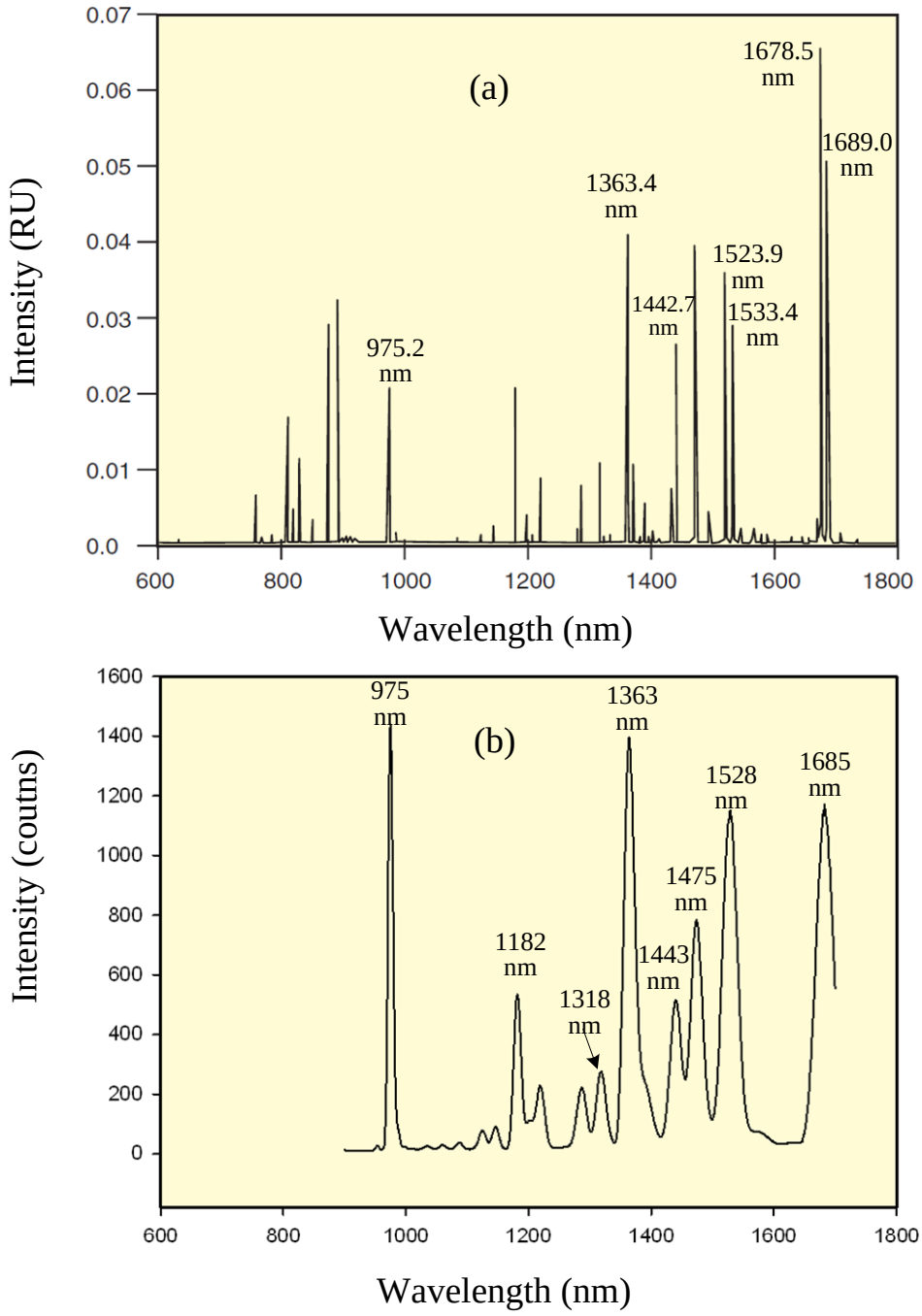

Figure 3.8: The spectra of 6031 Krypton Lamp: (a) adapted from the lamp manufactory catalog (Newport, 2010), and the spectrum was measured with MIR 8025 FT-IR with CaF2 beam splitter and InGaAs Detector; (b) measured by this spectral imaging system in the spectral region from 900 nm to 1700 nm.

3.6.2.2 Sensitivity

Ideally, the spectral output of a spectral imaging system should be consistent at wavelengths that the test object has identical reflectance spectral characteristics. That means the sensitivity (responsivity) of a spectral imaging system should be consistent in the working spectral range. The sensitivity of the LCTF-based spectral imaging system is determined by a combination of the spectral output of the light source, the transmittance of the LCTF, the transmittance of the lens, and the sensitivity of the InGaAs camera, which all are wavelength-dependent. Evans et al. (1998) reported a linear and a logarithmic method for leveling LCTF-based spectral imaging system sensitivity by controlling the LCTF attenuation and the camera gain. A similar approach was used in this work to level the system spectral sensitivity by controlling the camera exposure time and gain. However, the camera exposure time was used instead of the LCTF attenuation because the camera exposure time is easier to be manipulated. Moreover, increasing the camera exposure time can improve the signal to noise ratio of the system.

To obtain the original spectral response of the system, a 99% diffuse Spectralon target was scanned in the spectral region of 900 nm -1700 nm with 1 nm increments. The mean reflectance spectrum of a 30×30 pixel ROI was extracted from the center region of the target. Based on the visual observations of the mean spectrum collected, the system spectral region was divided into several sections to apply different camera exposure times. The InGaAs sensor provides a number of preset camera operation configurations that use different exposure times. Instead of assigning a specific exposure time to each individually wavelength band, the preset camera operation configurations were used to adjust the camera exposure time because those preset operation configurations also offered several useful camera-level functions, such as the FPA uniformity correction and the bad pixel correction. Direct manipulation of the camera exposure time will result in the loss of these applied functions. After the system spectral sensitivity was adjusted by applying preset camera operation configurations, the digital gain was used to fine tune the system sensitivity to a consistent level. The mean

reflectance spectrum of the Spectralon target was obtained again by using the previous method. A MATLAB program (2009b, The MathWorks, Natick, MA, U.S.A) was written to calculate the gain values for each wavelength band to make the system spectral sensitivity uniform. These wavelength-dependent camera exposure times and gains were saved to a text profile file. Using the profile file, the image acquisition software program alters the camera exposure time and gain correspondingly to calibrate the system sensitivity at each wavelength during image acquisition. Figure 3.9 illustrates three mean spectra of the Spectralon target before leveling sensitivity, after controlling the exposure time, and after applying both the camera exposure time and the digital gain control, respectively.

The dot curve in figure 3.9 shows the spectrum of the target scanned with the default camera exposure time (7.47 ms) and without gain control. It showed the great disparities at different wavelength regions. The system sensitivity was very low in the spectral regions below 970 nm and above 1670 nm. Thus, the working spectral range of this system is from 970 nm to 1670 nm. In the range of 970 nm - 1670 nm, the spectral signature curve showed three ascending plateaus from the low wavelength end to the high wavelength end. The system sensitivity in the region of 1500 - 1670 nm had three-fold increase over the region below 1150 nm, which revealed a strong need of leveling system sensitivity. Thus, multiple exposure time values (up to 16.57 ms) were applied to level up the system sensitivity below 1500 nm. After adjusting the exposure time, the system sensitivity had been increased 25% to 150% in the spectral region below 1500 nm. Finally, after applying wavelength by wavelength gain control, the system sensitivity curve was corrected to a relative flat line (figure 3.9). The means and standard deviations of these three curves are listed in the figure 3.9. The standard deviation of the reflectance spectrum of the 99% diffuse Spectralon target was reduced from 47.5% of the mean to 0.76% of the mean after correction, which indicated that the overall uniformity of the system spectral responsivity at the spectral axis had been great improved.

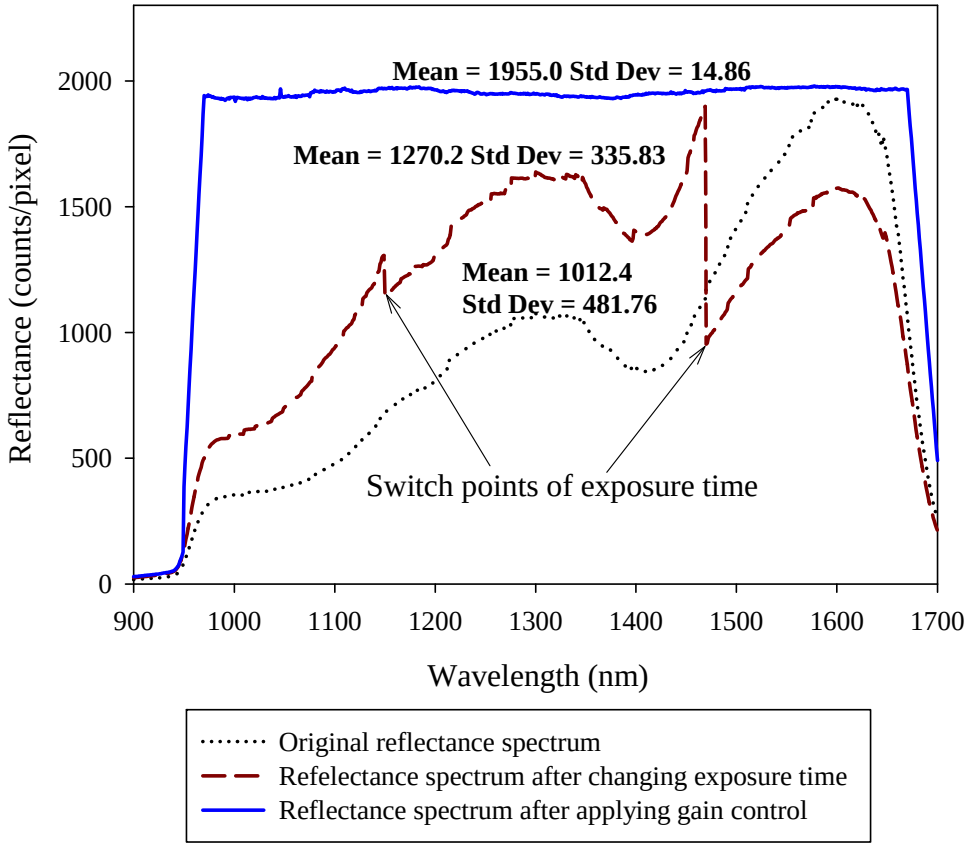

Figure 3.9: Reflectance spectra of the Spectralon 99% diffuse target before leveling the system sensitivity, after adjusting the camera exposure time, and after applying both the exposure time control and the gain control, respectively.

3.6.3 Linearity

In spectral imaging, the spectral signatures of the test object are built upon the pixels' intensity values of images. Thus, the linearity of system's response is a vital factor for a spectral imaging system. Ideally, the pixel intensity value of the system output should change linearly to the input light intensity. To verify the linearity of the system, a Spectralon multi-

step contrast target (model SRT-MS-050, LABSPHERE, NH, USA) was used. The target was a 127 mm × 127 mm square panel and consisted of four side-by-side panels which had equal reflectance of 99, 50, 25 & 12%, respectively. In this work, the target was scanned three times continuously from 900 nm to 1700 nm with 1 nm increments, and then the three captured hyperspectral images of the target were averaged, resulting a spectral image (T). The 99 % diffuse reflectance Spectralon target was also scanned to provide the white reference image (R). Dark current image (D) was recorded by averaging three scans as well. Thus, the following equation was used to convert the raw hyperspectral image of the multistep contrast target to a percentage image (I):

$$I = 99 \times \frac{T - D}{R - D}$$

From the converted percentage hyperspectral image of the multistep contrast target, a 30 × 30 pixels ROI was extracted on each of four small reflectance panels and the mean spectra of ROIs were calculated. Figure 3.10(a) shows relative reflectance values of four panels in the spectral range of 950 - 1700 nm. Spectra of the four spectral contrast panels were approximately parallel, which indicated a linear relationship between the system input and system output. It should be noted that the real reflectance rate of the 99% diffuse reflectance Spectralon target varied from 98.3% to 98.8% in the spectral range of 900 - 1700 nm. Thus, the reflectance values of a reflectance panel have small variations between 900 nm and 1700 nm. Figure 3.10(b) shows the linear equation obtained from the linear regression analysis by using the standard reflectance values (99%, 50%, 25%, and 12%) and the observed mean reflectance values (97.5%, 54%, 22.8%, and 15.9%) of four panels. The result (the coefficient of determination (r) = 1) confirmed the spectral linearity of the system.

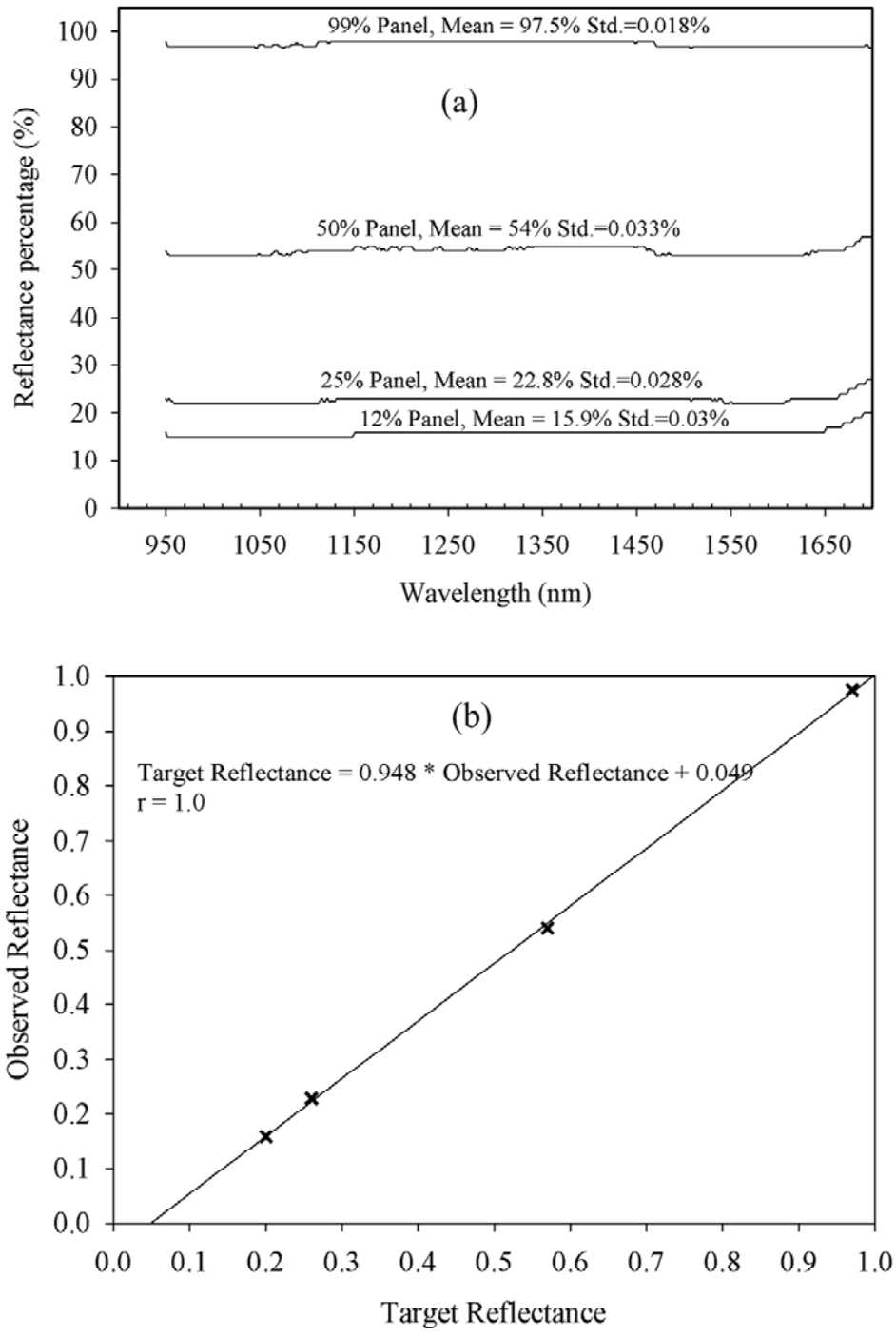

Figure 3.10: (a) Reflectance spectra of four Spectralon contrast panels (99, 50, 25 & 12% reflectance), measured by the LCTF-based spectral imaging system; (b) the linear regression plot of observed mean reflectance values and standard reflectance values of four Spectralon contrast panels.

3.6.4 Calibration Tests In Spatial Domain

3.6.4.1 Field of View

Field of view (FOV) describes the size of the area that is visible to the imaging system. FOV is often depicted by the angle of view (α). Calculating the angle of view as a function of distance enables system users to determine the optimal distance between the test object and the camera of the spectral imager. In the spectral imaging system, the narrow angle of view of the LCTF may change the FOV of the lens. Therefore, the FOV of the spectral imaging system should be measured on-site instead of an approximation based on the parameters of system components. In this work, a plastic transparent ruler was placed on a white Teflon board and imaged by the spectral imaging system from 950 nm to 1700 nm with the 50 nm intervals. The vertical heights of the camera's views were measured when the object-to-imager distances were set to 0.5 m to 1.2 m, with 0.1 m increments. Figure 3.11 shows the results of the test and the linear relationship between the vertical FOV and the object-to-imager distance. The FOV of the system was verified to be linear to the object-to-imager distance. When the object distance was 50 mm, the actual area imaged by the system was 77 mm $\times$ 61.5 mm (3 inch $\times$ 2.4 inch). Since the slope of the linear regression equation was 0.122, the actual angle of the view of the system was equal to: arctan (0.122) $\times$ 2 = 13.9 °.

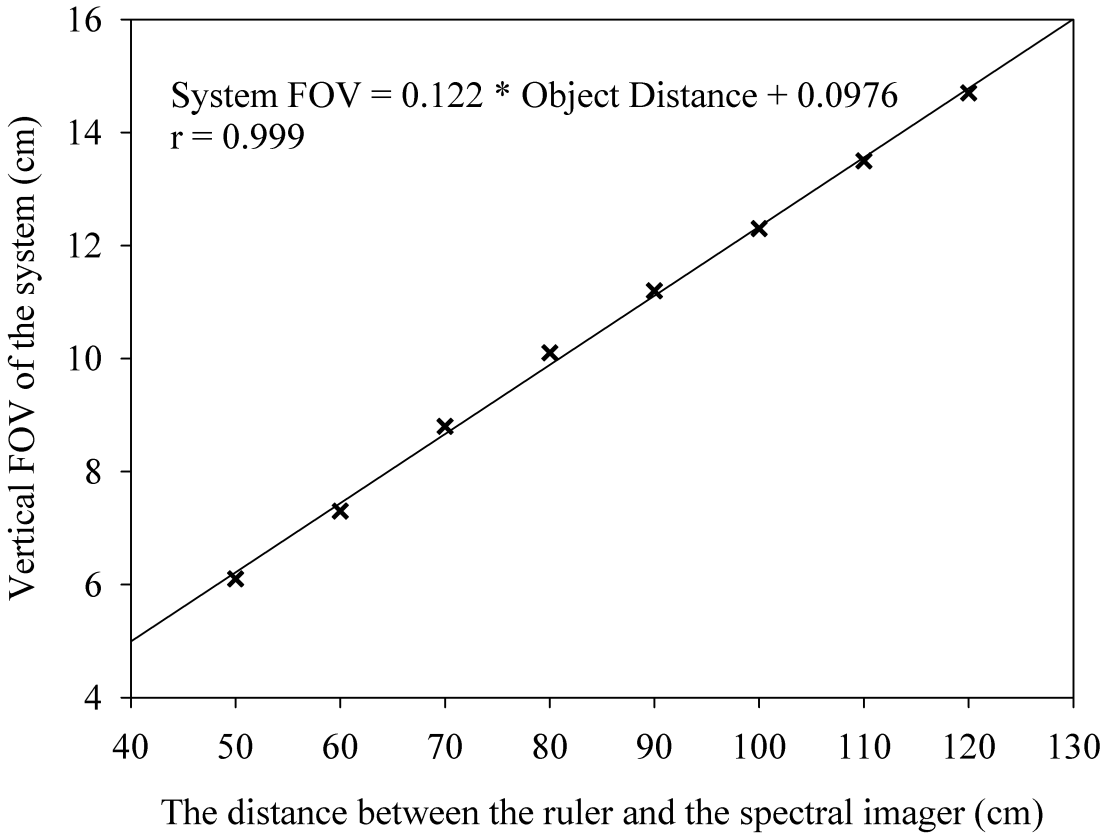

Figure 3.11: The vertical FOV of the system versus the distance between the test object and the lens of the LCTF-based spectral imager.

3.6.4.2 Spatial Resolution

The spatial resolution of the system was measured using a USAF 1951 resolution paper target (Edmund Optics Inc. Barrington, NJ, USA). The target was placed under the spectral imager, perpendicular to the optical axis of the system. The distance between the spectral imager and the target was adjusted until the overall test pattern fit in with the image plane. The target was scanned three times in the spectral range of 950 - 1700 nm with the intervals of 50 nm. Images were extracted from the hyperspectral image by using the ENVI software (ITT Visual Information Solutions, Boulder, CO, U.S.A). To quantify the spatial resolution, the horizontal and vertical histogram profiles of lines were extracted from the ruling sets (three identical bars in each set) in the resolution test chart. Intensity peaks and valleys of

histogram profiles were identified and the peak to valley ratio (PVR) of intensity profile was calculated for each ruling set, as shown in figure 3.12. A MATLAB program was written to calculate the PVRs of each ruling set in each extracted test chart image. A ruling set was deemed to be discernible when its PVR was larger than $\sqrt{2}$ (Gebhart et al., 2007). By this way, the system spatial resolution was recognized at the tested bands (figure 3.13). The measured spatial resolution of the system was from 3.17 to 2.52 line pairs per millimeter (lp/mm) in the spectral range from 1000 nm to 1650 nm, and 2 lp/mm at two ends (950 nm and 1700 nm). The results indicated that the spatial resolution of the system meets the design criterion (1 lp/mm).

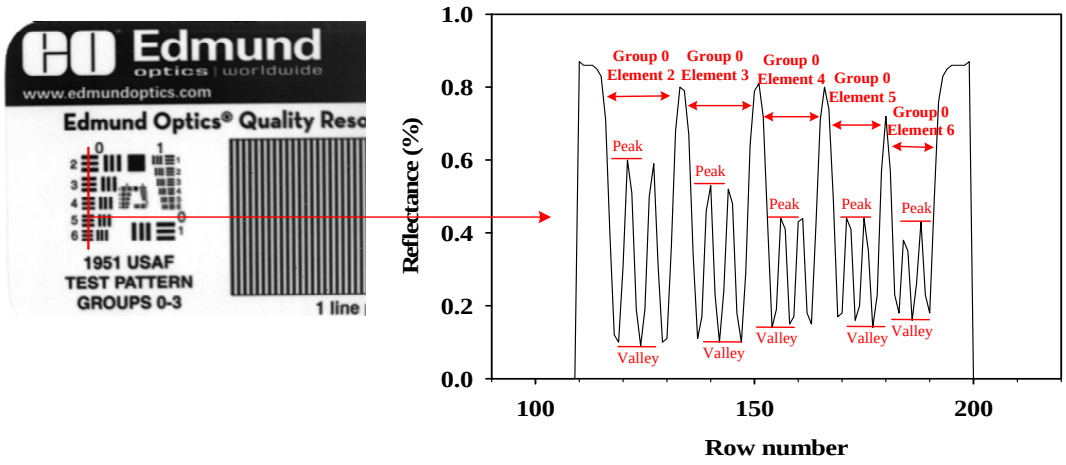

Figure 3.12: The 1951 USAF resolution test pattern and a demonstration of the line vertical histogram of ruling sets of Group 0, element 2 - element 6.

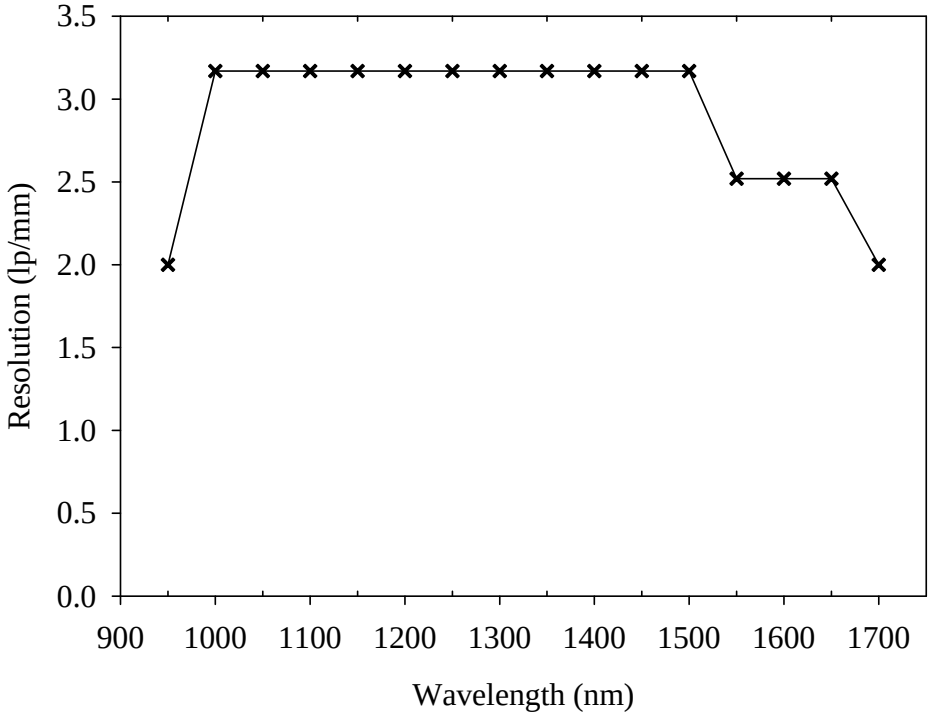

Figure 3.13: Spatial resolution of the spectral imaging system measured by using the 1951 USAF resolution test pattern.

3.6.4.3 Lens Distortion

Lens distortion is one of the major concerns in calibration of machine vision systems. Accurate modeling the lens distortion requires the use of some complex non-linear techniques or the combination of linear and non-linear techniques (Remondino and Fraser, 2006). The planar checkerboard pattern (Zhang et al., 1999) is a common target used for testing and correcting lens distortion. In this work, a simplified approach was developed to estimate and calibrate the lens distortion based on the planar checkerboard pattern. A square checkerboard pattern (10 $\times$ 10) was printed on a piece of A4 transparent film. The target was mounted on a flat Teflon sheet to create a planar checkerboard pattern target. The planar checkerboard target was scanned from 950 nm to 1700 nm with intervals of 50 nm. Images

at the wavelength 1000, 1100, 1200, 1300, 1400, 1500 and 1600 nm were extracted for estimating the image distortion caused by the lens. The method used is demonstrated in figure 3.14. Mean histogram was first calculated for each raw and each column of the test pattern. The first derivative of each histogram was computed. The absolute local maxima in the first derivative plot of each histogram were identified to indicate the positions of the internal borders between white and black grids. By comparing the positions of each internal border in rows/columns, the distortion of the lens can be estimated.

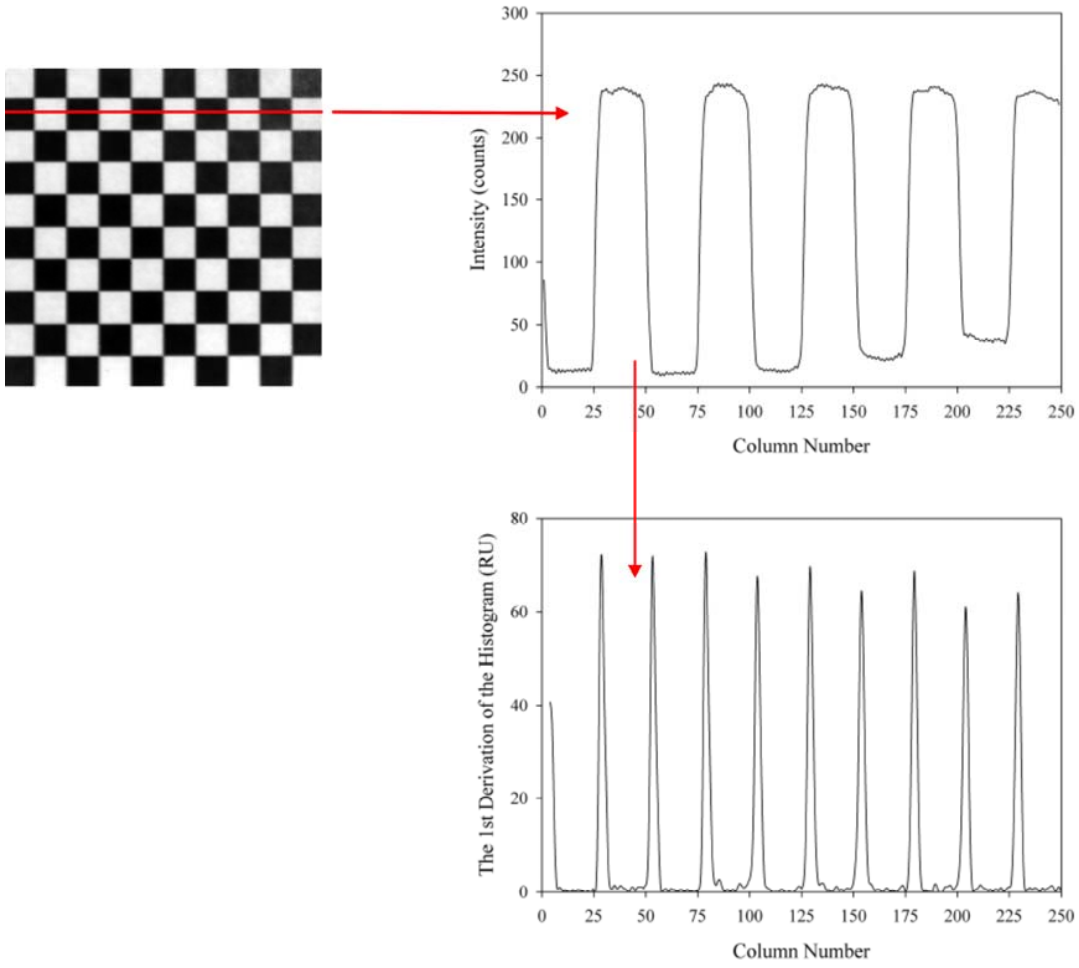

Figure 3.14: The schematic for estimating the lens distortion.

Figure 3.15 demostrates the positions and the first derivative values of the mean histograms of rows in the checkerboard target image at 1200 nm. At the 3rd, 4th, and 5th rows (from left to right in figure 3.15), the border positions kept constant. For all other rows, the positions of the internal borders showed very small (1-pixel) differences. These differences could be caused by the lens distortion or other factors such as the blur of the borders in the images. Thus, these small shits of the borders' positions were treated as acceptable. Similar results were obtained from the extracted images of the checkerboard target at other wavelengths. In summary, the distortion of the lens was confirmed to be an acceptable level.

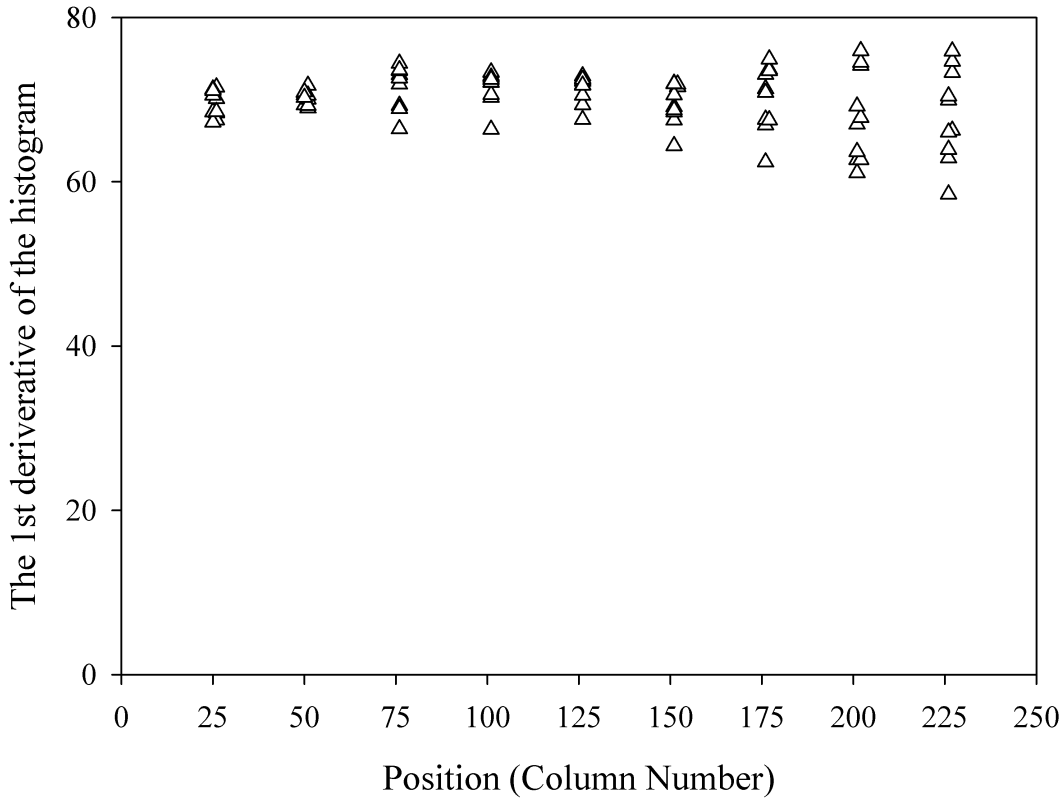

Figure 3.15: The scatter plot of the derivative values and positions of absolute local maxima in the first derivative plots of the mean histograms of rows in the image of the checkerboard target (at 1200 nm).

3.7 Demonstration

Water, 95% ethanol, sugar, and wheat flour were scanned by this LCTF-based SWIR system to demonstrate the system's capability for distinguishing agricultural materials in spectral and spatial domains. The goal of the test was to differentiate water from ethanol, and wheat flour from sugar. In the test, two liquid materials (3 ml 95% Ethanol and 3 ml water), and two solid materials (5 grams pure sugar and 5 grams wheat flour) were placed in the individual transparent glass plates. The plates with liquid materials were put on the sample stand side by side (figure 3.17) and then were scanned by this spectral imaging system from 950 nm to 1700 nm with 2 nm intervals. The process was repeated to scan the plates with solid materials. A dark image and an image of the 99% white reference were also captured for converting the collected images to percentage images. On the image area of each plate, a 10 $\times$ 10 pixels ROI was selected and the mean reflectance spectrum of the ROI was calculated. Figure 3.16 illustrates the extracted reflectance spectral signatures of these four materials. The spectrum of the water plate showed a lower reflectance than the spectrum of the plate with 95% ethanol, while the spectrum of the plate with wheat flour showed a higher reflectance than the spectrum of the plate with sugar. Reflectance differences were calculated wavelength by wavelength to identify the wavelengths that could show the best contrasts between the plates of water and the plate of ethanol, and between the plate of sugar and the plate of wheat flour. The two-end arrows in figure 3.16 indicated two wavelength bands which had biggest reflectance differences between the spectra of water and ethanol (1400 nm, marked by the left arrow), and between the spectra of sugar and wheat flour (1500 nm, marked by the right arrow).

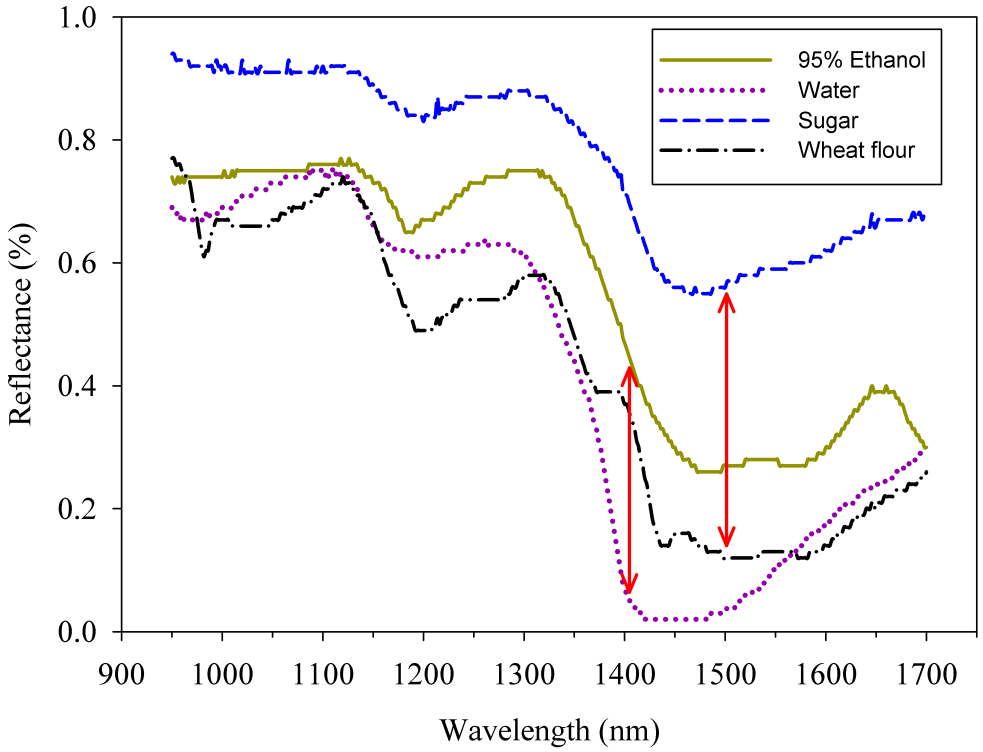

Figure 3.16: The reflectance spectra of 95% ethanol, water, sugar, and wheat flour in the wavelength range of 950 nm - 1700 nm.

Figure 3.17 demonstrates the images of the plate with water and the plate with 95% ethanol at 1100 nm and 1400 nm, and the images of the plate with sugar and the plate with wheat flour at 1100 nm and 1500 nm. In the image taken at 1100 nm, water and ethanol was shown as transparent liquid in plates and it's very difficult to distinguish them on the image. In the image taken at 1400 nm, because water absorbed more light energy than ethanol at this band, the plate with water was about 7 times darker than the ethanol plate on the image. Thus, water and ethanol can be easily distinguished using the image at the wavelength 1400 nm. Similar patterns can be observed on the plates with solid materials, the mean intensity of the wheat flour plate was 90% greater than the mean value of the sugar plate in the image taken at 1500 nm, whereas the pixel intensity difference between these two plates was only

20% in the image of 1100 nm. Therefore, using the intensity information provided by the image taken at 1400 nm, sugar and wheat flour can be easily distinguished.

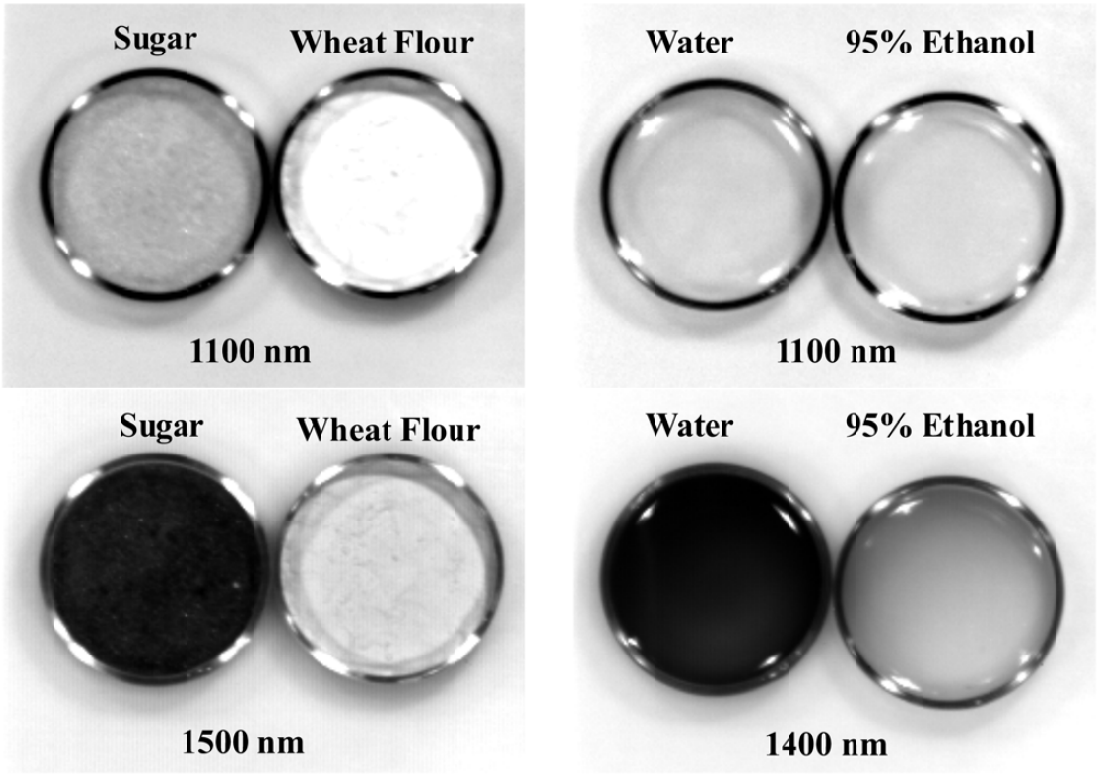

Figure 3.17: Spectral images of water, 95% ethanol, sugar, and wheat flour.

3.8 Conclusions

A dual-mode LCTF-based shortwave-infrared spectral imaging system was developed for safety and quality inspection of food and agricultural products. The data acquisition software can be used to control the hardware for acquiring hyperspectral images or multispectral images in the spectral region of 900 nm -1700 nm. The system was fully calibrated and optimized in both spatial and spectral domains. It was shown that the system has a 13.7 ° angle of view and its spatial resolution is from 2 lp/mm to 3.17 lp/mm. The spectral responsivity of the system was corrected and the spectral accuracy and spectral linearity of the system were also confirmed by calibration tests. Results of the validation test showed

that the SWIR spectral imaging is a promising technique for differentiating agricultural materials. Particularly, the system is suitable for spectral imaging applications that require fast selection of spectral bands and high quality images.

3.9 Bibliography

Archibald, D., Thai, C., Dowell, F., 1999. Development of short-wavelength near-infrared spectral imaging for grain color classification. Proc. SPIE 3543, 189–198.

Ariana, D. P., Lu, R., 2009. Evaluation of internal defect and surface color of whole pickles using hyperspectral imaging. Journal of Food Engineering 96 (4), 583–590.

Becker, L., Huntsville, A., 2005. Current and future trends in infrared focal plane array technology. In: Proc. of SPIE Vol. Vol. 5881. pp. 588105–1.

Chao, K., Yang, C.-C., Kim, M. S., 2010. Spectral line-scan imaging system for high-speed non-destructive wholesomeness inspection of broilers. Trends in Food Science & Technology 21 (3), 129–137.

Cogdill, R. P., Hurburgh Jr, C. R., Rippke, G. R., 2004. Single-kernel maize analysis by near-infrared hyperspectral imaging. Transactions of the American Society of Agricultural Engineers 47 (1), 311–320.

Egloff, T., Knobbe, J., Sinzinger, S., Gruger, H., 2009. Design of a micro-opto-electro-mechanical-system-based near-infrared hyperspectral imager. Applied Optics 48 (34), 6583–6593.

ElMasry, G., Wang, N., Vigneault, C., Qiao, J., ElSayed, A., 2008. Early detection of apple bruises on different background colors using hyperspectral imaging. LWT - Food Science and Technology 41 (2), 337–345.

Evans, M., Thai, C., Grant, J., 1998. Development of a spectral imaging system based on a liquid crystal tunable filter. Transactions of the ASAE 41 (6), 1845–1852.

Ferrero, A., Campos, J., Pons, A., 2006. Low-uncertainty absolute radiometric calibration of a ccd. In: Metrologia. Vol. 43. pp. S17 – S21.

Gat, N., 2000. Imaging spectroscopy using tunable filters: A review. Proceedings of SPIE 4056, 50–64.

Gebhart, S. C., Thompson, R. C., Mahadevan-Jansen, A., 2007. Liquid-crystal tunable filter spectral imaging for brain tumor demarcation. Applied optics 46, 1896–1910.

Gowen, A. A., O'Donnell, C. P., Cullen, P. J., Downey, G., Frias, J. M., 2007. Hyperspectral imaging - an emerging process analytical tool for food quality and safety control. Trends in Food Science & Technology 18 (12), 590–598.

Hansen, M., January 2009. What You Should Ask Before Investing In A Short-wave Infrared (SWIR) Lens. Tech. rep., Photonics Online, 2591 Wexford-Bayne Road, Building II, Suite 305, Sewickley, PA 15143.

Kim, M. S., Chen, Y. R., Mehl, P. M., 2001. Hyperspectral reflectance and fluorescence imaging system for food quality and safety. Transactions of the American Society of Agricultural Engineers 44 (3), 721–729.

Kim, M. S., Lee, K., Chao, K., Lefcourt, A. M., Jun, W., Chan, D. E., 2008. Multispectral line-scan imaging system for simultaneous fluorescence and reflectance measurements of apples: Multitask apple inspection system. Sensing and Instrumentation for Food Quality and Safety 2 (2), 123–129.

Kise, M., Park, B., Heitschmidt, G. W., Lawrence, K. C., Windham, W. R., 2010. Multispectral imaging system with interchangeable filter design. Computers and Electronics in Agriculture 72 (2), 61–68.

Lawrence, K. C., Park, B., Windham, W. R., Mao, C., 2003. Calibration of a pushbroom hyperspectral imaging system for agricultural inspection. Transactions of the American Society of Agricultural Engineers 46 (2), 513–521.

Lopez-Alvarez, M. A., Hernandez-Andres, J., Romero, J., 2008. Developing an optimum computer-designed multispectral system comprising a monochrome CCD camera and a liquid-crystal tunable filter. Applied Optics 47 (24), 4381 – 4390.

Lu, R., Chen, Y.-R., 1998. Hyperspectral imaging for safety inspection of food and agricultural products. Proceedings of SPIE - The International Society for Optical Engineering 3544, 121–133.

Mehl, P. M., Chen, Y.-R., Kim, M. S., Chan, D. E., 2004. Development of hyperspectral imaging technique for the detection of apple surface defects and contaminations. Journal of Food Engineering 61 (1 SPEC), 67–81.

Naganathan, G. K., Grimes, L. M., Subbiah, J., Calkins, C. R., Samal, A., Meyer, G. E., 2008. Visible/near-infrared hyperspectral imaging for beef tenderness prediction. Computers and Electronics in Agriculture 64 (2), 225–233.

Newport, 2010. Oriel pencil style calibration lamps. Retrieved 10 Nov, 2010, from http://www.newport.com/CatalogPDF/e5395.pdf.

Park, B., Lawrence, K. C., Windham, W. R., Buhr, R. J., 2002. Hyperspectral imaging for detecting fecal and ingesta contaminants on poultry carcasses. Transactions of the American Society of Agricultural Engineers 45 (6), 2017–2026.

Peleg, K., Anderson, G. L., Yang, C., 2005. Repeatability of hyperspectral imaging systems - quantification and improvement. International Journal of Remote Sensing 26 (1), 115–139.

Peng, Y., Lu, R., 2006. An LCTF-based multispectral imaging system for estimation of apple fruit firmness: Part I. Acquisition and characterization of scattering images. Transactions of the ASABE 49 (1), 259 – 267.

Polder, G., Van der Heijden, G. W. A. M., 2001. Calibration and characterization of spectral imaging systems. In: Multispectral and Hyperspectral Image Acquisition and

Processing, October 22, 2001 - October 24, 2001. Vol. 4548 of Proceedings of SPIE - The International Society for Optical Engineering. SPIE, pp. 10–17.

Qin, J., Burks, T. F., Ritenour, M. A., Bonn, W. G., 2009. Detection of citrus canker using hyperspectral reflectance imaging with spectral information divergence. Journal of Food Engineering 93 (2), 183–191.

Remondino, F., Fraser, C., 2006. Digital camera calibration methods: considerations and comparisons. International Archives of Photogrammetry, Remote Sensing and Spatial Information Sciences 36 (5), 266–272.

Shafri, H. Z. M., Yusof, M. R. M., 2009. Trends and issues in noise reduction for hyperspectral vegetation reflectance spectra. European Journal of Scientific Research 29 (3), 404–410.

Singh, C. B., Jayas, D. S., Paliwal, J., White, N. D. G., 2007. Fungal detection in wheat using near-infrared hyperspectral imaging. Transactions of the ASABE 50 (6), 2171–2176.

Singh, C. B., Jayas, D. S., Paliwal, J., White, N. D. G., 2010. Identification of insect-damaged wheat kernels using short-wave near-infrared hyperspectral and digital colour imaging. Computers and Electronics in Agriculture 73 (2), 118–125.

Sittner, W., Peck, E., 1949. The spectra of argon, krypton, and xenon between 1.2 and 2.2 microns. J. Opt. Soc. Am 39, 474–477.

Smith, W. J., 2008. Modern optical engineering: the design of optical systems, 4th Edition. McGraw-Hill, Two Penn Plaza, New York, NY, 10121-2298.

Wang, W., Morrison, J., Paliwal, J., 2006. Correcting axial chromatic aberration in a fixed focal plane, near-infrared imaging system. CSBE/SCGAB 2006 Annual Conference.

Wang, W., Paliwal, J., 2007. Near-infrared spectroscopy and imaging in food quality and safety. Sensing and Instrumentation for Food Quality and Safety 1, 193–207.

Williams, P., Geladi, P., Fox, G., Manley, M., 2009. Maize kernel hardness classification by near infrared (NIR) hyperspectral imaging and multivariate data analysis. Analytica Chimica Acta 653 (2), 121 – 130.

Yang, C. C., Chao, K. L., Chen, Y. R., 2005. Development of multispectral image processing algorithms for identification of wholesome, septicemic, and inflammatory process chickens. Journal of Food Engineering 69 (2), 225–234.

Yoon, S. C., Park, B., Lawrence, K. C., Windham, W. R., Heitschmidt, G. W., 2010. Development of real-time line-scan hyperspectral imaging system for online agricultural and food product inspection. Proceedings of the SPIE 7676, 76760J–76760J–11.

Zhang, M., Ludas, L. I., Morgan, M. T., Krutz, G. W., Precetti, C. J., 1999. Applications of color machine vision in the agricultural and food industries. Proceedings of SPIE - The International Society for Optical Engineering 3543, 208–219.

Chapter 4

Development of the Data Acquisition Software for an LCTF-Based Shortwave Infrared Spectral Imaging System

4.1 Overview

Software development is a major challenge for developing a spectral imaging system. This chapter presents the design and development of a LabVIEW program for the liquid crystal tunable filter (LCTF) based spectral imaging system. The goal was to develop a robust and flexible image acquisition software program that can be used by the LCTF-based spectral imaging system. The software was developed by using the LabVIEW graphic programming language. The architecture, design, and implementation of the program are described and discussed in depth in this chapter. This program has been successfully employed to an LCTF-based spectral imaging system, which was developed for food safety and quality inspection. It has been proven that the software program is a reliable and flexible tool to control the LCTF-based spectral imaging system for spectral image acquisition.

4.2 Introduction

Spectral imaging, which includes hyperspectral and multispectral imaging, is a rapidly growing area in food safety and quality inspection. In the past decade, spectral imaging hardware has become more cost-effective due to the advances in electronics and optics. Spectral imaging, particularly hyperspectral imaging, has been applied for various purposes. As a result, the need for the high performance spectral imaging systems has grown rapidly. A spectral imaging system, nonetheless, requires sophisticated software to control hardware,

and acquire and process spectral images. Currently, commercial hyperspectral software like ENVI (ITT Visual Information Solutions, CO, U.S.A) is derived from the remote sensing and can provide powerful functions for displaying and analyzing spectral images. But the spectral image acquisition software is still a grey area. Currently, spectral imaging data acquisition software is often provided by hardware manufacturers. This kind of software is often with inadequate functions, and limited flexibility and extensibility. Actually, a spectral imaging system is a complex integration of optical and electronical hardware components, which are integrated and controlled by the software. In practice, a small change of the lighting could require re-calibration and re-optimization of the system hardware and software. Therefore, spectral image acquisition software has strict requirements on flexibility and extensibility. As a result, many researchers and engineers have to design and develop their own hyperspectral image acquisition software programs due to their unique hardware configurations, or requirements for additional functions and superior performance.

Although most publications of the spectral imaging applications included some description of the software, only a few introduced the design and implementation of their software programs in detail. Lerner and Drake (1999) demonstrated the design of a software program for a line-scan microscopy hyperspectral imaging system in the spectral range of 385 nm - 750 nm. Their program was developed on LabVIEW and can collect 242 spectra at each line that it scanned. However, the paper put emphasis on presenting its software's functions rather than discussing software design strategies. To our knowledge, there are few publications that discussed the software development for the LCTF-based shortwave infrared spectral imaging system. In fact, LCTF-based spectral imaging has many special requirements and considerations. This chapter describes the design and implementation of the software program for spectral image acquisition, using the hardware system described in Chapter 3.

Software architecture is a critical factor for the success of a software program (Bass et al., 2003). To cope with the complexity of the spectral imaging system, the software for spectral image acquisition requires a well-designed architecture. The finite state machine

(FSM) model, which is often described by a "Moore machine", is a powerful design pattern for implementing complex decision-making algorithms. It is one of the most common software architectures of controlling systems (Wagner et al., 2006). The FSM can provide good support for both design and implementation phases of software development. It allows dynamic operations of the system by defining the system operations to a number of states and providing flexible transitions between the states. Due to its effectiveness and high flexibility, the FSM is one of the most common software structures used by real-time applications (Williams, 2006).

Many programming languages/platforms, such as C++ (Evans et al., 1998; Yoon et al., 2010), Microsoft Visual Basic (Kim et al., 2001), and LabVIEW (Lerner and Drake, 1999; Martin et al., 2006), have been used to develop HSI/MSI software. Selection of a programming platform depends upon many factors, including the skill of the developer, the type of drivers/modules/libraries provided by the hardware manufacturer, and the extensibility and reliability of the platform, etc. The software presented here was developed on LabVIEW platform because of its capability for controlling electronical hardware. Another advantage of LabVIEW is its rich graphic user interface (GUI) widgets, which can be easily linked to and control the hardware components of the spectral imaging system. Moreover, LabVIEW has gained recognition for its simple graphic dataflow programming language and low learning curve for new programmers.

The objectives for developing this software program were to design and implement a LabVIEW program to collect spectral images for the LCTF-based spectral imaging system, and optimize the flexibility and extensibility of the software for future maintenance and enhancement.

4.3 Hardware System Overview

A spectral imaging system was developed to capture hyperspectral or multispectral images in the spectral region of 900 - 1700 nm for reflectance and transmittance measurements.

The system hardware included a spectral imager, an illumination system, the frame grabber, and a computer. The essential hardware component of the system was the spectral imager, which includes a liquid crystal tunable filter (Model Varispec LNIR 20-HC-20, Cambridge Research & Instrumentation, MA, U.S.A), an InGaAs camera (Model SUI320KTS-1.7RT, GOODRICH, Sensors Unlimited, Inc, U.S.A), and an optical focusing lens (Model SOLO 50, GOODRICH, Sensors Unlimited, Inc, NJ, U.S.A). The bandpass of the LCTF be tuned over the spectral region 850 -1800 nm, with 20 nm FWHM (Full-Width at Half-Maximum) and a working aperture of 20 mm. It takes 50 ms to 150 ms for the LCTF to tune the bandpass to a specific wavelength.

The spectral response of the InGaAs camera is from 900 nm to 1700 nm, which is part of the spectral response region of the LCTF. Thus, the HSI imager has a spectral response region from 900 nm to 1700 nm. The digital output interface of the InGaAs camera was a 12 bit Base Configuration Camera Link. A frame grabber (NI PCI-1426, National Instruments Corporation, U.S.A) is linked to the InGaAs camera and is used to capture 12-bit 320 $\times$ 256 pixels gray images with a maximum speed of 60 frames per second (fps). The light source was provided by four quartz halogen lamps (MALIBU 81664, Intermatic, IL, USA). A tripod with a 3-way head was modified and used as the sample stand, so that the object-to-camera distance and the orientation of the test sample can be easily adjusted. To demonstrate the versatility of the system, an additional digital color CCD camera was added. The color camera can collect the complementary color information of the test object since this spectral imager was designed to collect spectral images in the shortwave infrared (SWIR) region. Figure 4.1 shows the schematic of the system hardware setup.

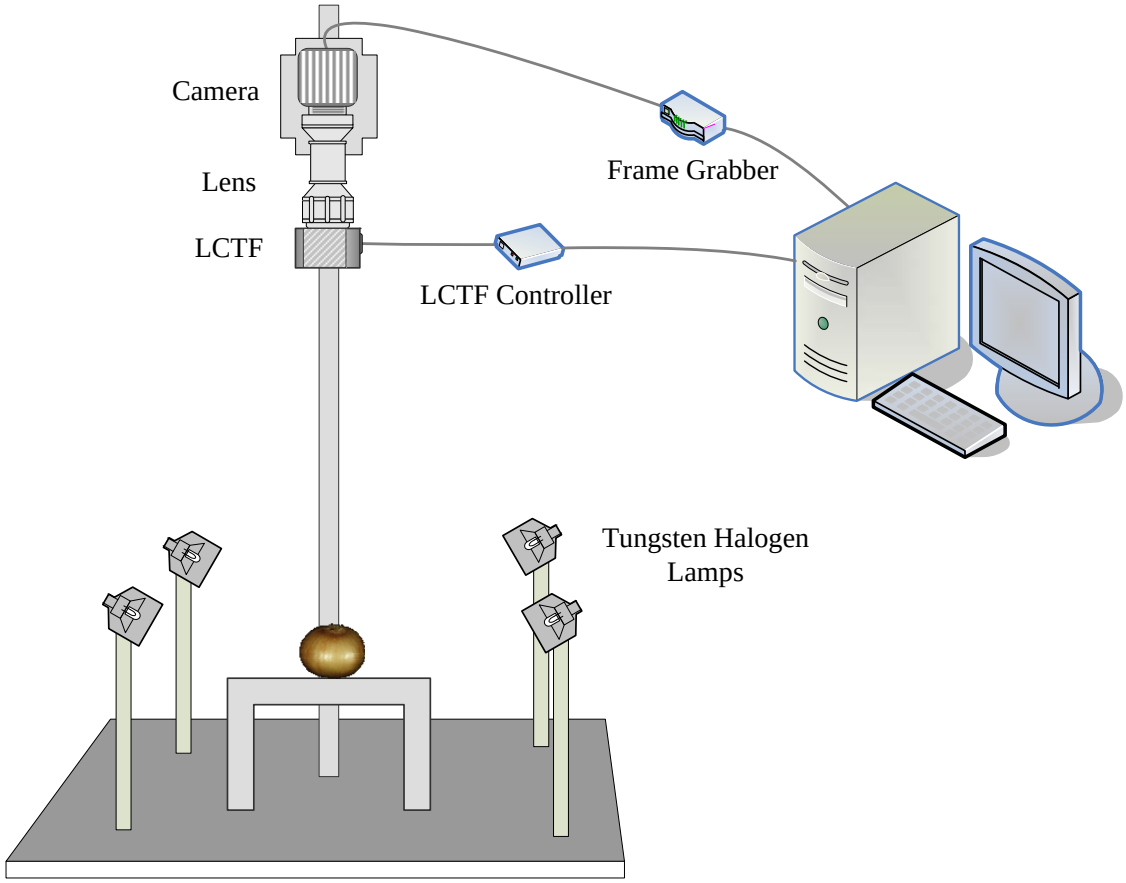

Figure 4.1: The schematic of the LCTF spectral system hardware

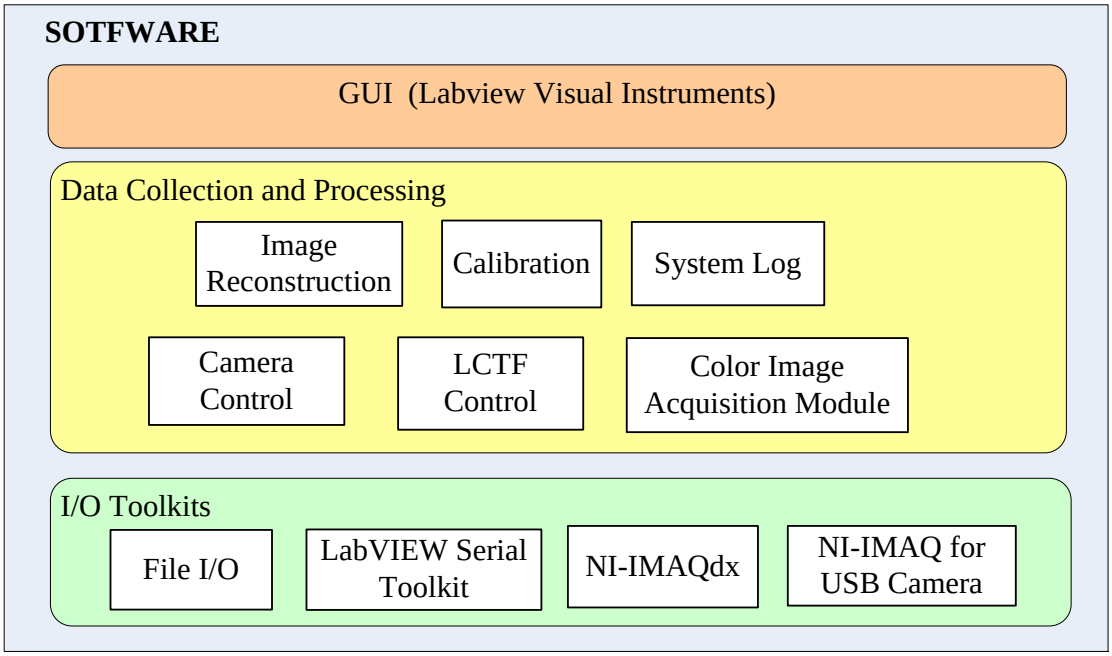

Figure 4.2: The diagram graph of the three-tier structure of the data acquisition software

4.4 Software Design

The software was designed to a three-tier structure, as shown in figure 4.2. A set of toolkits provided by the National Instruments form the low level I/O communication tier, which sends commands and collects data from the hardware components. The data collecting and processing tier contains the most of the processing models for controlling hardware, collecting data, and processing images. The graphic user interface (GUI) tier built on LabVIEW virtual instruments is the topmost level of the system, which provides user interfaces for the system operators. All modules were written by the LabVIEW graphic programming language and organized as virtual instruments (sub-VIs). The details of these modules are discussed in following sections.

System operating processes and status were organized by using a finite state machine model. When the software is operated by a user, different user actions from the user inputs

lead to different processing segments. These segments can either be followed by another segment, or wait for another user event or the end the process flow. In a FSM, each process segment/status is modeled as a state. The process flow and transitions of states are managed by the state machine, depending on the history activities and the current inputs. LabVIEW provides simple but fully-formed state machine infrastructures to help developers build applications quickly.

Figure 4.3 demonstrates the main state diagram of this software program. The FSM was implemented following the design pattern recommended by technical documents of National Instruments. It consists of while loops, case structures, shift registers and transition codes. Data collecting segments and data processing segments of the system were modeled to eight states in the FSM. Each state includes a set of transactions that should be executed as a batch for the same objective. The program can either enter to another state or stay in the current state waiting for another user event. As shown in figure 4.3, the application starts a scan from an "initialization" state, which represents the status that software is loaded into computer memory, and ready for accepting user's input. A "stop" state represents the close of the software program by performing a sequence of clean up actions. State 2-7 represent the main operating statuses of the program for controlling hardware components and collecting images. The system can flexibly perform image acquisition processes to collect a color image and a spectral image together or acquire them independently.

Using the FSM design pattern, the program can easily adjust the process flow or add more states into the system based on the requirements of different applications. A typical process for image acquisition is illustrated in figure 4.4. The system is first initialized by establishing connections with all hardware components. Then, the software program monitors the user's inputs from GUI for setting parameters and waits for the commands to collect images. In this stage, the user can preview the color/SWIR images, set parameters, specify the directory for storing collected images, and start an image data acquisition process. In this case, the image collection starts from capturing a color image. The color image is automatically saved

1. INITIALIZATION
2. PARAMETER SETTING
3. WAIT FOR UI EVENTS
4. CHECK PARAMETERS AND HARDWARE CONNECTIONS
5. COLOR IMAGE ACQUISITION
6. HSI/MSI HEADFILE GENERATION
7. HSI/MSI IMAGE RECONSTRUCTION
8. STOP

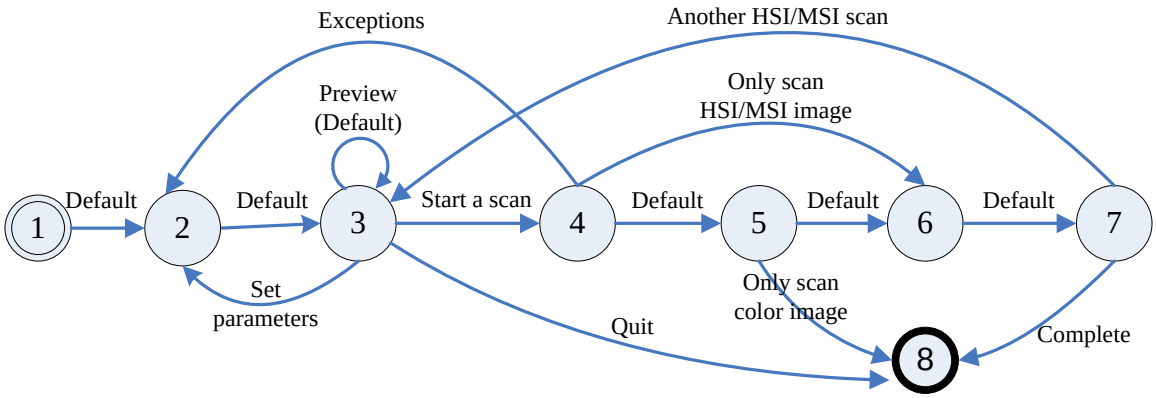

Figure 4.3: The state diagram for the data acquisition software of the spectral imaging system

to the predefined directory. Next, based on the parameters set by the user, the head file for the spectral image cube is created and saved to the predefined directory. After that, the software controls the spectral imager to take images of the test object at each wavelength in the specified wavelength region. During scanning, the software program sends commands to LCTF to tune the filter to a specific wavelength, and then synchronizes the InGaAs camera to take a snapshot of the view. The image data from the snapshot is first cached in memory until it is sent to the image reconstruction module, in which the cached image s pre-processed and then appended to the spectral image cube. After all wavelengths are scanned, the spectral image cube is named automatically and saved to a predefined path in computer.

4.4.1 Programming Language and Tools

The LabVIEW graphic dataflow programming language, referred to as the language G, was used as the main programming language. Using drivers offered by the LabVIEW, the program can easily communicate with the hardware devices through standard software interfaces. The LabVIEW NI-IMAQdx toolkit provided very good supports to the Camera Link interface of the InGaAs camera. Another benefit of using LabVIEW was that the graphical programming approach allows programmers to implement a program quickly by dragging and dropping virtual representations of lab equipment. This feature can shorten the time period required for the software development. The whole system development work was conducted in the Windows XP (Windows XP SP2, Microsoft, U.S.). Two open source software programs, Subversion 1.6 and TortoiseSVN 1.6.5 (Tigris.org, CollabNet Inc.), were used to maintain the versions of the source code.

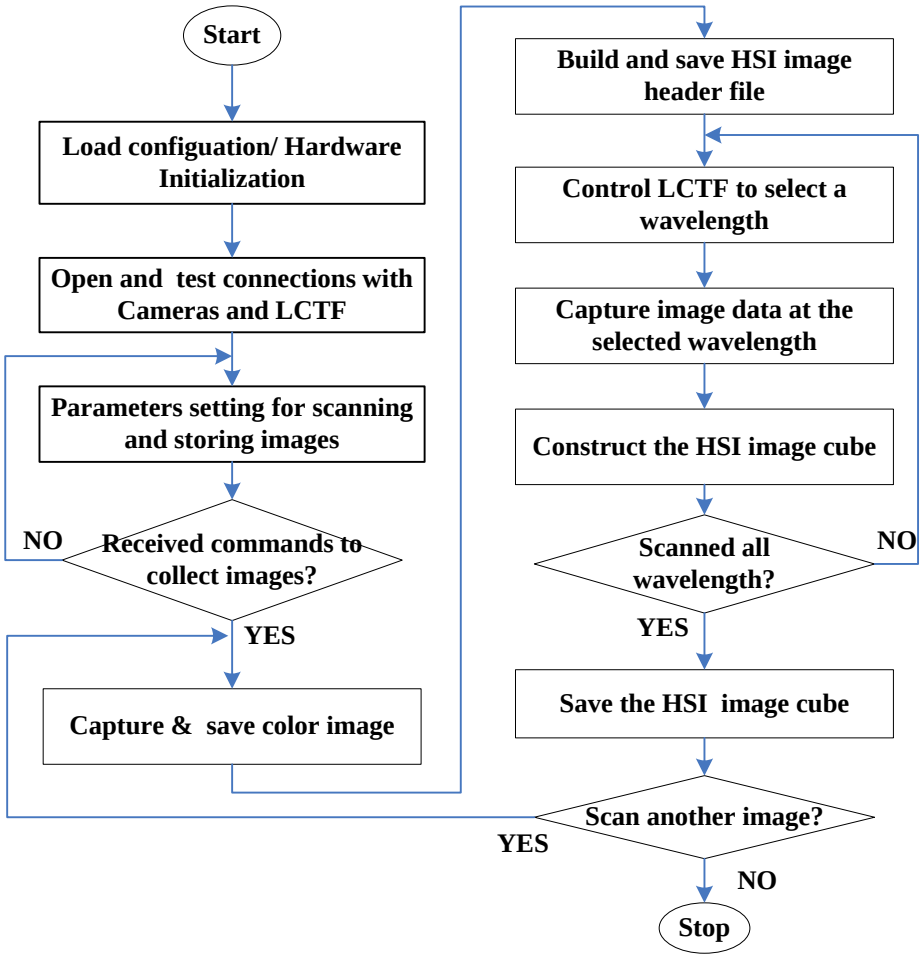

Figure 4.4: The flow chart of a typical spectral image acquisition process

4.5 Description of Software

4.5.1 Graphic User Interface (GUI)

The GUI of the program provides user friendly interfaces for users. It contains a main window and several popup windows. The main window includes five panels: the camera setting panel, the LCTF setting panel, the image preview panel, the system operation panel, and the system status panel. Figure 4.5 shows the main GUI window for spectral image acquisition. The camera setting panel provides the user the interface for setting the camera name and other parameters. The LCTF setting panel was designed to control the LCTF for collecting spectral images. The user can switch the system mode between the HSI and MSI modes by using the two-item radio controls on the top of the LCTF panel. When the user makes a choice of conducting a HSI or MSI scan, the corresponding inputs in the LCTF setting panel are enabled for setting parameters. The parameters stored in the global configuration file will be applied if the user doesn't set parameter values. The image preview panel is used for previewing images before or during HSI/MSI scans. The status panel consists of two read only text input boxes, for prompting help messages to the user and displaying the status information of the system, respectively. In addition to the main operation window, a few popup windows are used for selecting a region of interest (ROI), set camera parameters, and setting multispectral wavelength numbers.

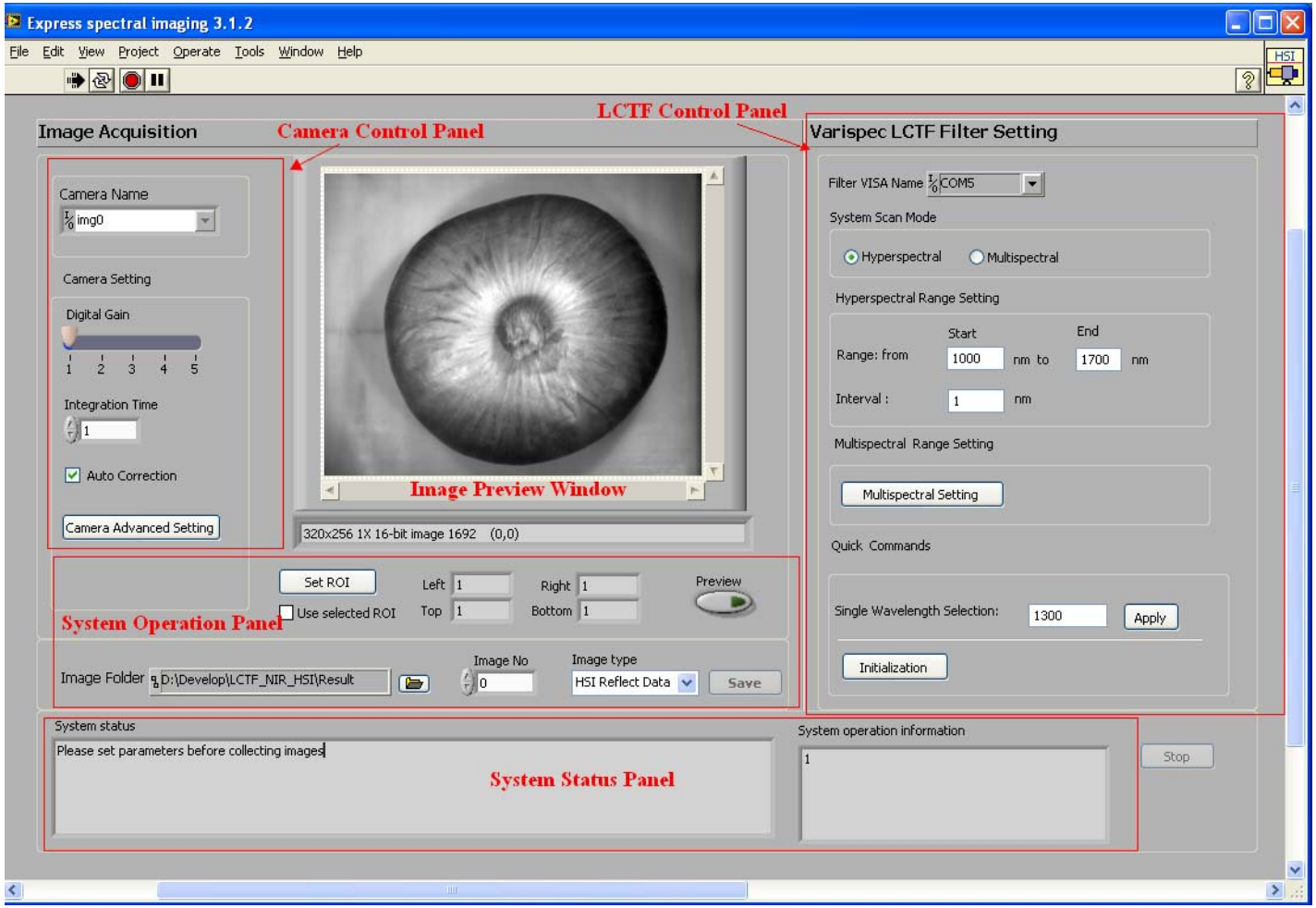

Figure 4.5: The main graphic user interface of the software

4.5.2 System Configuration and Log Files

The configurations of the system are stored in several text configuration files. Each configuration file includes a number of keywords written in ASCII. Two types of configuration files are used for this program: the global configuration file and the module-level configuration file. The global configuration file stores the initial settings and some important parameters of the system, such as the default camera name, the default LCTF interface name and the threshold value for the temperature of LCTF, etc. The module-level configuration files store the parameter settings for processing modules, such as the default start and end wavelength numbers for the hyperspectral imaging scanning. All configuration files are ASCII text files and users can change the values of keywords by any text editor. Another type of text file, known as the log file, is used to record important user activities and system error/warning messages occurred during system operation. The log file was created and managed in a similar approach with the configuration files and it was also used for debugging the program during the system development stage.

4.5.3 The Camera Module

The camera module was developed to control the camera to acquire, display, and save monochrome images through the frame grabber. This module was built on the NI-IMAQdx VI library. The NI-IMAQdx VI library provides groups of application programming interface (API): low-level functions and high level functions. Low level functions can be used for low-level camera control, such as start/stop image acquisition, set/change a camera attribute, and get error information, etc. High level functions encapsulate low levels functions for capturing images more quickly and easily. This camera module mainly uses high level functions of the NI-IMAQdx library. The NI-IMAQdx library provides three methods of using high level functions: snap, grab, and sequence. The snap method captures a single image to computer memory at one time. The grab methods grabs a number of images continually but only the last image can be used for processing and analysis. The sequence method acquires

a specific number of images in a sequence and all these images are saved into the internal buffers for further processing.

A spectral image acquisition has to continuously take images at a serial of specified wavelength bands. The sequence method was first considered since it can acquire consecutive images in a high-speed. However, a hyperspectral image cube contains data up to several hundred megabytes. These image data have to be cached in internal and user buffers, which most likely to exhaust the system resources and lead the program to be unstable. The grab method is also not appropriate because the problem of hardware synchronization. After the camera captures one image, the program has to wait for 50-150 ms for tuning a wavelength by the LCTF. Thus, using the snap functions, the snap image collection process has to be manually suspended for synchronizing hardware, which could make the program unstable. In summary, the grab functions were used to acquire images in this program.

Figure 4.6 demonstrates a process of collecting a spectral image by using the grab functions. In the initialization stage, a camera session is first opened to identify the camera and build a camera session. To establish a camera session, the camera name and camera control mode have to be specified. As for the camera control mode, the NI-IMAQdx provides two options: controller or listener. The controller mode controls camera for collecting image data, while the listener mode can only receive image data. This program uses the controller mode. After initialization, the program configures the camera attributes using the parameters pre-defined in the InGaAs camera configuration file. In a LabVIEW application, the camera configuration file is managed by the National Instruments Measurement & Automation Explorer (NI-MAX) software. In runtime, the camera attributes can also be changed by using the low level functions in NI-IMAQdx VI library. After configuration, images are acquired by using the snap functions iteratively. In this stage, the module copies 12-bit monochrome image data from the camera internal buffers to computer memory. In the computer, the raw data is decoded to the image type “Image_I16” for further processing and

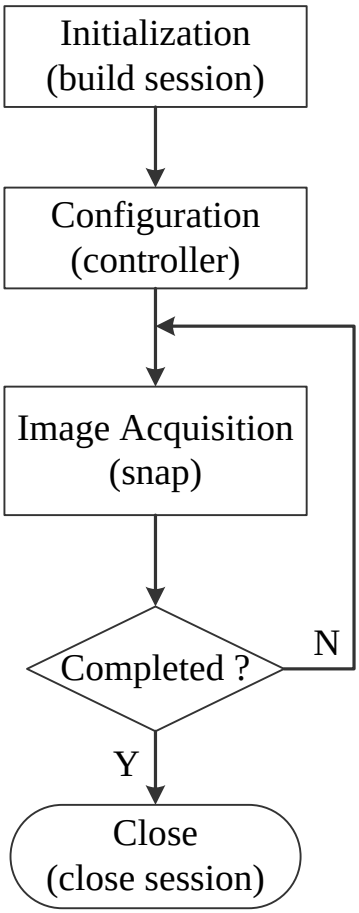

Figure 4.6: The flow chart for a snap-shot spectral image using NI-IMAQdx library

displaying. Finally, the camera session is closed and the camera is disconnected from the computer when the acquisition is completed.

4.5.4 The LCTF Module

The LCTF module was designed to control the LCTF for selecting wavelengths in the spectral region of 900 - 1700 nm. Although the actual data communication interface is a USB interface, the LCTF is recognized as a virtual COM device at 9600 baud rate in the computer. The manufacturer (Cambridge Research & Instrumentation, Inc., MA, U.S.A) provided a software

developer's kit (SDK) for controlling the LCTF. The SDK included a set of sub-VI LabVIEW files for LabVIEW applications. These sub-VIs provide fundamental functions for tuning the wavelength of the LCTF and inquiring the LCTF status.

Based on the image acquisition mode that the user selected, the LCTF module can control the LCTF for acquiring hyperspectral images or multispectral images. For a hyperspectral image acquisition, the user must set up a start wavelength band, an end wavelength band, and the wavelength interval. All values are integers with nanometers as units. Base on these parameters, the LCTF module automatically calculates the next wavelength number on which it has to tune the LCTF during scanning. In contrast, the user has to specify the wavelength numbers and the order of the wavelength bands in a multispectral imaging scan (figure 4.7). During scanning, the LCTF module tunes the bandpass of the LCTF to the pre-defined wavelength bands in order.

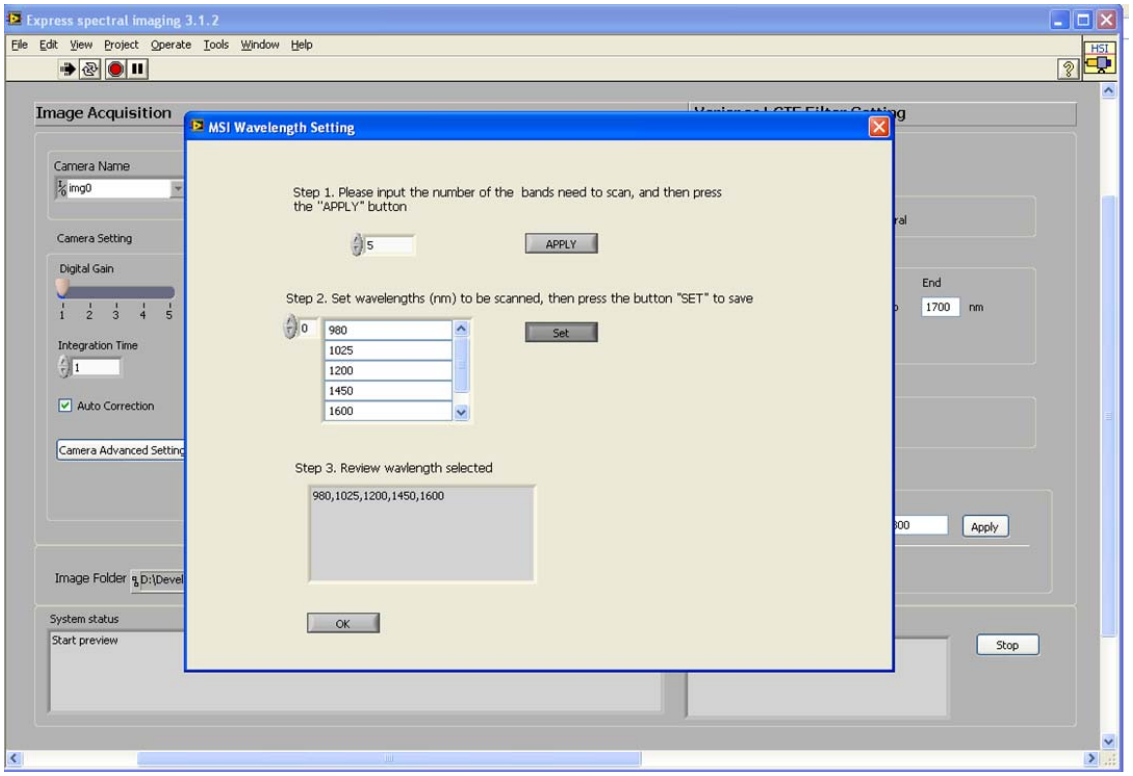

Figure 4.7: The graphic user interface of setting wavelength bands for multispectral image acquisition.

The temperature of the liquid crystal (LC) cells is monitored in the program for guaranteeing the safety of the equipment. The LCTF only allows a narrow band of light to pass through it and blocks light in all other bands. As a result, the energy received by the filter is several hundred or several thousand times greater than the energy that passed through the filter. This system uses halogen lamps as the light source, which emits heat carried by light in infrared bands. Since this LCTF works in the shortwave infrared region, it does not utilize a dielectric hot-mirror for reflecting the infrared energy away, which is a common method that the LCTFs for VIS use. Thus, the majority of the infrared energy will be absorbed by the LCTF filter. Under some situations like using improper lighting, the energy could accumulate and damage the LCTF. Thus, it is necessary that the temperature of the LCTF during the operation period be monitored. This program queries the temperature of the LCTF every 30 seconds when there is no image acquisition task. It also queries the temperature of the LCTF before and after every HSI/MSI scan. The temperature of LCTF is displayed in the status window on the main GUI in centigrade. When the temperature of the LCTF exceeds the threshold value preset in the configuration file, the program will signal with an alarm and set the LCTF to the sleep mode.

4.5.5 The Spectral Image Reconstruction

The spectral image reconstruction module combines the acquired two-dimensional images into a three-dimensional spectral image, known as an image-cube. This program stores the captured raster image data as a stream of binary bytes. The images collected by this software are in ENVI format. There are three common encoding methods for a spectral image: Band Sequential Format (BSQ), Band Interleaved by Pixel Format (BIP), and Band Interleaved by Line Format (BIL). The BSQ stores 2-D spatial images in a sequential order (image by image) according to the order of the images in the spectral domain. BIP saves spectra of the pixels in the image cube in a succession order. It first stores the spectrum of the first pixel, and then save the spectrum of the pixel next to the previous pixel, and so on. The

BSQ format is suitable for accessing the spatial bands and the BIP format can provide good performance for extracting the spectral data in the spectral image. The BIL format, however, is a tradeoff between the BSQ format and the BIP format. The BIL format saves the first line in the first band, and then iteratively saves the information of the same line at the next band, until the last band in the spectral image. Then, it saves the second line for all bands successively, and so on. In summary, since the LCTF-based spectral imaging system collects 2-D images band by band, this program used the BSQ format for encoding the spectral images due to its simplicity and efficiency for re-constructing the image-cube.

The ENVI spectral image format also requires an ASCII header file for each image file. In the image header file, the detailed information of the image is described for automatic image processing. The information is stored as keyword-value pairs in the header file. Critical keywords for a spectral image include: samples, lines, bands, file type, data type, header offset, interleave, band names, and byte order. A LabVIEW sub-VI was developed to automatically create, read, and write image header files during scanning. An image header file is named as the same as the image data file but with different suffix. The ENVI software will automatically search and read the information in the image header file when an image data file is loaded.

4.5.6 The Digital Color Camera Control

The digital color camera module was designed to control the compact digital color camera. Using the LabVIEW USB camera universal toolkit (NI-IMAQ for USB Cameras 1.0, National Instruments Corporation, TX, U.S.A), the color camera control module is completely independent with the camera hardware. Thus, without any change of the software, the CCD camera can be easily replaced by any CCD camera using a USB interface. The NI-IMAQ for USB camera provided two types of image acquisition approaches: snap and grab, whose principles are similar with the snap and grab image acquisition methods discussed in the camera module. This program utilizes the grab image to continuously acquire single 32 bits

RGB color images into the computer memory. The last acquired image saved in the buffer is saved into the computer.

4.6 Conclusions

This chapter demonstrated the development of the image acquisition software for an LCTF-based spectral imaging system. The software program was developed on the LabVIEW platform by using the LabVIEW graphic programming language. The use of the finite state machine design pattern maximized the flexibility and expandability of the system. The software provides flexible operations for acquiring spectral and color images. Using this program, the LCTF-based spectral imaging system can be used to collect: hyperspectral images, multispectral images, or color images based on users' needs. The program was successfully employed by the applications reported in this thesis for collecting spectral images. Results indicated that the program is a reliable and flexible tool for acquiring spectral images using the LCTF-based shortwave infrared spectral imaging system.

4.7 Bibliography

Bass, L., Clements, P., Kazman, R., 2003. Software Architecture in Practices, 2nd Edition. Addison-Wesley Longman Publishing Co., Inc. Boston, MA, USA.

Evans, M., Thai, C., Grant, J., 1998. Development of a spectral imaging system based on a liquid crystal tunable filter. Transactions of the ASAE 41 (6), 1845–1852.

Kim, M. S., Chen, Y. R., Mehl, P. M., 2001. Hyperspectral reflectance and fluorescence imaging system for food quality and safety. Transactions of the American Society of Agricultural Engineers 44 (3), 721–729.

Lerner, J. M., Drake, L. A., 1999. Hyperspectral imaging in a labview environment. Proceedings of SPIE - The International Society for Optical Engineering 3605, 264–272.

Martin, M. E., Wabuyele, M. B., Chen, K., Kasili, P., Panjehpour, M., Phan, M., Overholt, B., Cunningham, G., Wilson, D., Denovo, R. C., Vo-Dinh, T., 2006. Development of an advanced Hyperspectral Imaging (HSI) system with applications for cancer detection. Annals of Biomedical Engineering 34 (6), 1061–1068.

Wagner, F., Schmuki, R., Wagner, T., May 2006. Modeling software with finite state machines: a practical approach. Auerbach Publications, Boca raton, New York.

Williams, R., 2006. Real-time systems development. Butterworth-Heinemann, 30 Corporate Drive, Suite 400, Burlington MA 01803.

Yoon, S. C., Lawrence, K. C., Line, J. E., Siragusa, G. R., Feldner, P. W., Park, B., Windham, W. R., 2010. Detection of campylobacter colonies using hyperspectral imaging. Sensing and Instrumentation for Food Quality and Safety 4 (1), 35–49.

Chapter 5

Near-infrared Hyperspectral Reflectance Imaging for Early Detection of Sour Skin in Vidalia Sweet Onions [1]

[1]This article has been partially presented in American Society of Agricultural and Biological Engineers (ASABE) 2010 Annual International Meeting. Wang, W., Li, C., Gitaitis, R., Tollner, E.W., Rains, G., Yoon, S.-C., 2010. Near-infrared Hyperspectral Reflectance Imaging for Early Detection of Sour Skin Disease in Vidalia Sweet Onions, ASABE Annual International Meeting, Pittsburgh, Pennsylvania, June 20 - June 23, 2010.

5.1 Abstract

Sour skin is a major onion disease caused by the bacterium *Burkholderia cepacia (B. cepacia)*. The disease not only causes substantial economic loss from diseased onions but also could lead to pulmonary infection in humans. It is critical to prevent onions infected by sour skin from entering storage rooms or being shipped to fresh vegetable markets. This paper reports the development of a hyperspectral imaging method for early detection of sour skin-infected onions. In this study, near-infrared hyperspectral reflectance images of 40 Vidalia sweet onions were taken in 2 nm increments from 950 nm to 1650 nm, before and after they were inoculated with *B. cepacia*. Inoculated onion samples were scanned every day after inoculation for 7 days, while the hyperspectral images scanned before inoculation were used as controls. Spectral signatures of onion hyperspectral images were extracted from selected regions of interest. Based on the principal component analysis conducted on spectral signatures of control and inoculated samples, two optimal spectral bands (1070 nm and 1400 nm) were selected to construct ratio images, which revealed the difference between the control and inoculated samples better. Mean ratio values at three different areas on the onion surface (flesh body area, root or neck area, and the whole onion area) were calculated from ratio images and used as inputs for classification models. The three spatial features of mean ratio values obtained from band-ratio images were proven to be good indicators of sour skin-infected onions. When comparing two classifiers, The back-propagation neural network (BPNN) models performed better (95% accuracy) than support vector machine (SVM) classifiers (85%-90%) in discriminating control samples and inoculated samples on day 6 after inoculation. Then, the optimal BPNN classifier using three spatial features of band-ratio images was applied to classify hyperspectral images of tested onion samples over the period of 1-7 days after inoculation, respectively. The results of tests showed that the near-infrared hyperspectral reflectance imaging technique could detect sour skin-infected onions effectively from day 4 to day 7 after inoculation by achieving overall classification accuracies of 80%, 85%, 95%, and 100%, respectively.

Keywords: *Hyperspectral imaging, Vidalia sweet onion, Near-infrared, sour skin, non-destructive testing, food quality and safety.*

5.2 Introduction

Vidalia sweet onion is a world-renowned specialty crop grown in the southeast area of Georgia. It has been a remarkable success story of a lucrative niche market and contributed a farm gate value of $138 million in 2009 (Boatright and McKissick, 2009). Consumers like Vidalia sweet onions due to the onions' sweet (mild) flavor. Vidalia sweet onions lack of pungency compounds found in other varieties (Maw et al., 1989). The absence of pungency compounds, however, makes Vidalia onions more susceptible to fungal or bacterial diseases compared to other onion varieties. Sour skin (caused by *Burkholderia cepacia*) is a bacterial disease that can affect most onion varieties (Burkholder, 1950). The exposure of onions to sour skin infection in controlled atmosphere (CA) rooms is often disastrous because the infection may spread out gradually and affect healthy onions, resulting in up to 50% storage losses (Gitaitis, 1994; Tollner et al., 1995). In addition, some strains of *B. cepacia*, are human pathogens and have been deemed a leading cause of death in individuals with cystic fibrosis (CF) lung disease (Chmiel and Davis, 2003; Isles et al., 1984). Therefore, it is critical to identify and eliminate sour skin-infected onions during the grading process before they are stored in CA rooms or delivered to flesh vegetable markets. The screening of defective Vidalia sweet onions on packing lines is currently carried out manually by human graders. However, sour skin is often limited in a few inner bulb scales at the early stage, and infection can remain latent until the onion becomes mature (Schwartz and Mohan, 2008). Therefore, it is difficult for human visual inspection (HVI) to detect sour skin-infected onion. Furthermore, the performance of detecting sour skin by the HVI is subjected to human subjectivity and inconsistency. Thus, a non-invasive automated detection method that can accurately discriminate sour skin-infected onions and healthy onions is urgently needed.

Researchers have explored a number of nondestructive methods for measuring onion quality and detecting defective onions. X-ray imaging has been studied for detecting internal defects in Vidalia sweet onions, including voids and foreign inclusions (Shahin et al., 2002; Tollner et al., 1995). Birth et al. (1985) reported that NIR spectra of onions can be used to predict dry matter content of intact onions, which indicated that there are some correlations between internal quality of onions and their NIR spectra. Few studies have been found in the literature regarding non-invasive detection of sour skin in onions. The gas sensor array technology was explored to detect sour skin in onions (Li et al., 2009). It achieved 85% correct classification rate when six gas sensors were used. Although this technology showed a promising result to detect sour skin, the gas sensors are more suitable in an indoor confined environment instead of in packing lines.

Hyperspectral imaging (HSI), also named imaging spectroscopy, is another widely used non-destructive sensing technology that combines advantages of conventional machine vision and spectroscopy techniques (Gowen et al., 2007; Lu and Chen, 1998). High resolution spectral and spatial information stored in hyperspectral images makes HSI a powerful tool for studying underlying spectral and/or spatial characteristics of the tested object. In the past, considerable successful applications have been reported on a broad range of agricultural products for non-invasive quality inspection, such as apples (ElMasry et al., 2008; Kim et al., 2002; Lu, 2003), citrus (Qin et al., 2008, 2009), pickling cucumbers (Ariana and Lu, 2008), and poultry (Lawrence et al., 2004; Park et al., 2002; Yoon et al., 2010).

A hyperspectral reflectance image consists of monochrome images over hundreds of bands. Also, images at neighboring spectral bands are often highly correlated, which contains a lot of redundant information for classification. Thus, feature selection is a critical and indispensable task for hyperspectral image analysis and classification. It is often desirable to select the most relevant spectral and/or spatial characteristics from substantial features contained in hyperspectral images of tested objects. Since hyperspectral images are essentially multi-

variate images, multivariate statistical methods and machine learning techniques have been widely used for dimension reduction and feature selection (Grahn and Geladi, 2007).

The overall goal of this study was to detect sour skin in Vidalia sweet onions using near-infrared hyperspectral reflectance images. Specific objectives were to:

- Characterize control and sour skin-infected onions using near-infrared reflectance images in the spectral region of 950 nm-1650 nm;
- Develop a hyperspectral imaging method for early detection of onions infected by sour skin;
- Determine two optimal wavelength bands for classification;
- Develop classification algorithms for discriminating sour skin-infected onions from healthy onions, and evaluate the accuracy and performance of the classification method.

5.3 Materials and Methods

5.3.1 Plant material

One hundred Vidalia sweet onions were harvested in the Vidalia area of Georgia in 2009 and were used for this study. Onion bulbs were visually inspected to remove diseased or defective bulbs, and then were sorted into medium or jumbo groups based on size. In each size group, 20 onion bulbs were selected for further testing. As a result, 20 medium and 20 jumbo healthy Vidalia sweet onions were selected as test samples. All 40 onions had been stored for 3 months in a controlled atmosphere storage room of the Vidalia Onion and Vegetable Research Center in Tifton, GA prior to use in this study.

5.3.2 Inoculation

The 40 onions were inoculated with a suspension of *B. cepacia* in sterile tap water. The concentration of inoculum used in the study was approximately 1×10^6 colony-forming-units

(CFU)/ml, which induced rot in one week at 30°C. Bacterial suspensions were infiltrated into bulbs (1.0 ml per onion) under the first couple of layers at the root cap. Inoculated onions were put into plastic bags individually to avoid cross contamination and stored in an incubator (30°C) during the test period.

5.3.3 Hyperspectral imaging system

A near-infrared hyperspectral imaging system based on liquid crystal tunable filter (LCTF) technology was employed for measuring hyperspectral reflectance images of onions. The system consisted of a near-infrared hyperspectral imager, a frame grabber, an illumination system, a digital color camera, and a computer with software for hyperspectral image acquisition. The schematic diagram of the system is shown in Fig. 5.1.

The near-infrared hyperspectral imager consisted of a liquid crystal tunable filter (Model Varispec LNIR 20-HC-20, Cambridge Research & Instrumentation, MA, USA), an InGaAs camera (Model SUI320KTS-1.7RT, GOODRICH, Sensors Unlimited, Inc, NJ, USA), and an optical focusing lens (Nikkor 50mm f/1.4D AF, Nikon, Japan). The spectral response of the monochrome InGaAs sensor is from 900 nm to 1700 nm. The LCTF can tune wavelength continuously over the wavelength region of 850 nm to 1800 nm, with a minimum 1 nm interval and 20 nm FWHM (Full-Width at Half-Maximum). Coupled with a frame grabber (NI PCI-1426, National Instruments, Austin, TX, U.S.A), the HSI imager can capture 12-bit gray images of 320×256 pixels resolution at spectral bands from 900 nm to 1700 nm, with a maximum speed of 60 frame per second (fps).

The illumination system consisted of four 10-watt quartz halogen lamps (MALIBU 81664, Intermatic Incorporated, Spring Grove, IL, U.S.A). Lamps were powered by a stabilized power supply (12v/DC, 350w). Four lamps were arranged manually so that light on the imaging area was as uniform as possible. Since the HSI imager could only take images in near-infrared region, a digital color camera (Microsoft LifeCam Cinema, Microsoft, WA, U.S.A) was integrated into the system to collect RGB color images of onions to simulate

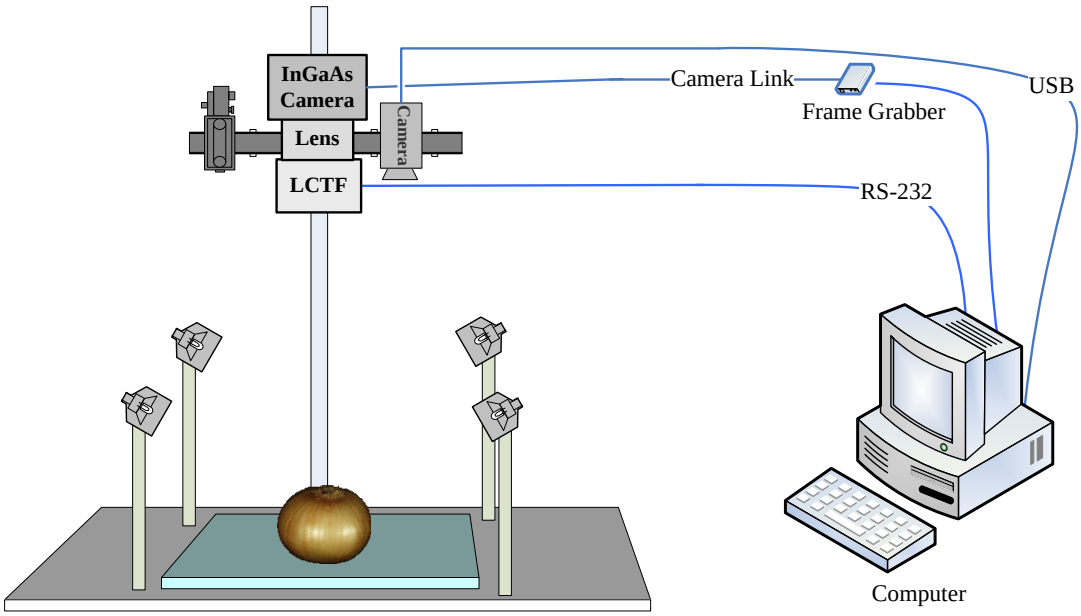

Figure 5.1: The schematic view of the near-infrared hyperspectral imaging system

human vision observations. The color camera has high-precision glass lens and can collect RGB color images of 900×600 pixels resolution with a frame rate up to 30 fps.

The hyperspectral image acquisition software was developed by using LabVIEW 8.2 (National Instruments, Austin, TX) which was installed on a computer (OptiPlex 755, Dell, Round Rock, TX, U.S.A) with a Intel Duo processor E8200 (6M Cache, 2.66 GHz, 1333 MHz FSB) and a 4 GB RAM (random access memory). The software was able to tune the LCTF band by band, control the InGaAs camera to take images, and grab data from the frame grabber to computer memory. After finishing the scans over all bands in the spectral region, the software constructed a 3-D hyperspectral image cube, and then automatically saved the image. The digital color camera was also controlled by the software for a color image acquisition before or after a hyperspectral image scan, so that the color images of the tested object can be automatically collected.

5.3.4 NIR Reflectance hyperspectral image acquisition

The 40 onion samples were evenly divided into two groups (Group I and Group II), with 10 medium and 10 jumbo bulbs in each group. For later identification purposes, all samples were labeled by sequential integer numbers (1-40) written on plastic bags where onions were stored individually. A sample holder was fabricated to hold an onion bulb so that the onion could be kept in a fixed position during scanning. The holder consisted of a wooden box (120×120×30 mm) with a hole cut (radius 30 mm) on the top plate. During scanning, onions in the group I were placed on the sample holder with the neck facing the HSI imager, so that the neck area of each onion bulb was imaged. Onions of the group II were scanned with the root facing the HSI imager so that the half bulbs of root side of onions were captured by hyperspectral images.

The hyperspectral reflectance images of onion samples were collected in a dark room using the HSI system. The aperture of the lens was set at f/2.0. Before the inoculation, onion samples were first scanned, and the scanned hyperspectral images were used as images of "healthy (control) onions". In the subsequent 7 days after inoculation, all onions were scanned once every day. After each scan, infection levels and surface symptoms of each onion were inspected and recorded by a trained inspector. Then, it was replaced in the incubator (30 °C) immediately.

Onions were scanned for 7 days, and then were cut in half from the neck to root and the outer layers peeled away to examine the infection level caused by *B. cepacia*. Among 40 onions tested, sour skin successfully developed in 17 onions of Group I and 18 onions of Group II. In some samples, however, sour skins were slight and limited to the very deep layers of onions and beyond detections of the HSI system. Thus, only 25 onions (12 onions in Group I and 13 onions in Group II) that showed sour skin symptoms on the surface at the end of testing (day 7th) were selected to be further analyzed. For each selected onion, eight hyperspectral reflectance images (1 before inoculation and 7 after inoculation) were recorded. In total, 200 hyperspectral images of 25 onion samples were used in this paper.

5.3.5 Preprocessing of hyperspectral images

Hyperspectral images were preprocessed to obtain relative reflectance hyperspectral images of samples. The white reference images were obtained by scanning a white reference standard plate (120mm × 120 mm, Spectralon, Labsphere, North Sutton, NH, USA), which has 98.1% to 99.3% reflectance in the spectral range of this study (950 nm - 1650 nm). Dark current images were acquired when the lens of the hyperspectral imaging system was completely covered by its cap. Using collected white reference and dark hyperspectral reflectance images, relative reflectance calibration was performed to normalize the intensity values of original hyperspectral images using the following equation:

$$I_R = \frac{I_{raw} - I_{dark}}{I_{ref} - I_{dark}}$$

where I_R is the corrected relative reflectance image, I_{raw} is the original image without any correction, I_{ref} is the white reflectance image obtained from the Spectralon panel and I_{dark} is the dark image. By conducting flat field calibration, image noises caused by dark current of the camera were removed, and raw hyperspectral images were converted to relative reflectance hyperspectral images (reflectance value range is 0-1).

5.3.6 Principal component analysis for optimal wavelength selection

Selection of optimal wavelength bands in this study can be thought of as spectral dimension reduction of the full wavelength bands, since each NIR spectrum is essentially a 1-D multivariate data that has 351 spectral variables. Principal component analysis (PCA) is an eigenvector-based algorithm that has been widely used for the dimension reduction of multivariate data (Rencher, 2002). Using principal components derived from PCA, a low-dimensional model can be built to best explain the variance in the original data set. The elements of eigenvectors, called PC loadings, are coefficients that determine the weights of original variables in new factors. By analyzing the PC loadings, the smaller number of original variables, which represent the original dataset best, could be determined. These variables

could be used to build a fast classifier with less computational complexity than classifiers using full original inputs. In this study, PC loadings of the first two PCs were analyzed to select two optimal wavelength bands for the classification algorithm which is discussed in following sections.

5.3.7 Classification methods based on band ratio images

In hyperspectral and multispectral imaging, an effective technique frequently used is to divide an image at one wavelength by the image of another band (Ariana et al., 2006). A ratio image is able to provide unique information that may not be available in single band of the raw image. In this study, a two-band ratio algorithm was applied to images at two optimal wavelengths. Ratio images were partitioned to background, flesh body, and neck/root parts by using masks obtained by image processing. Mean ratio values of flesh body area, neck/root area, and the whole onion area were used as input features for classification. To test the need of original image information, these three parameters were also computed on one of original images at selected optimal wavelength bands. As a result, for each hyperspectral image, six spatial features were extracted from its image.

For each onion in 25 selected samples, band ratio images were extracted from hyperspectral images of onions scanned before inoculation (control) and day 6, respectively. Grayscale images at the selected optimal wavelength bands were also extracted. Selected features described above were calculated on these images. As a result, 50 patterns of onions (25 healthy and 25 diseased) were obtained as dataset I. The dataset was partitioned randomly into to two parts: a training dataset (60%, 30 patterns) and a testing dataset (40%, 20 patterns). For the use of training Artificial neural networks (ANNs), the training dataset was further divided into a training set (45%, 22 patterns) and a validation dataset (15%, 8 patterns). The validation dataset was used to stop training of ANN models to avoid overfitting. Based on dataset I, dataset II was created by removing three spatial features from the

original onion images. That is, dataset II only contained the three features extracted from band ratio images.

Artificial neural networks (Eberhart and Shi, 2007) and support vector machines (SVMs) (Cortes and Vapnik, 1995) are very useful and efficient methods for classification. A multi-layer neural network using back propagation learning rules (BPNN) can learn non-linear relations between input features and classification labels. SVMs can use linear models to implement classes that have non-linear boundaries. In this work, these two machine learning methods have been used to develop classifiers to discriminate diseased and non-diseased Vidalia sweet onions. Optimal models of classifiers were obtained by trial and error.

The BPNN classifier used in this work was provided by the MATLAB neural network toolbox (2009b, The MathWorks, Natick, MA, USA). The BPNN model 1, which was used to classify dataset I, consisted of three layers (6-5-1), with six input nodes, five hidden units and a single output node. Logistic activation functions were used for the hidden and output neurons, whereas a linear function was used for the input nodes. The network was trained by Levenberg-Marquardt back-propagation algorithm with a learning rate = 0.2, a momentum = 0.2, and initial weights randomly generalized between 0.5 and 0.5. The training was stopped after 1000 epochs or when the network performance failed to be improved on validation dataset in 20 epochs. The BPNN model 2, designed for dataset II, had similar configuration with the BPNN model 1. But it only had three input nodes and three hidden units since the input feature reduced to three.

The software package called SMO in WEKA 3.6.2 (The University of Waikato, Hamilton, New Zealand) was employed to develop a support vector machine classifier. In the SVM model developed for this work, a Gaussian kernel function, called the radial basis function (RBF) was used as the kernel of the classifier. The exponent value of the RBF kernel was 1.0.

5.4 Results and Discussion

5.4.1 Characteristics of near-infrared hyperspectral reflectance images and spectra

Fig. 5.2 shows the mosaic image of one tested onion. It demonstrates images of the onion at seven wavelength bands from 1000 nm to 1600 nm with 100 nm increments (as shown in each row) over the testing period from day 1 to day 7 (shown in each column). In fig. 5.2, a dark triangle spot on the left center area can be observed in onion images from 1000 nm to 1300 nm on day 5. This dark spot increased on day 6 and day 7. Alsp, in images at bands between 1200 nm and 1600 nm, the pixel intensity of the onion root area decreased along with the development of the sour skin. These observations are in agreement with our expectation that *B. cepacia* broke down the inner scale of the onion it colonized, and then developed towards the outer layers. Hyperspectral images captured the physical or chemical change of onion tissues beneath the outer surface layer when disease symptoms reach the layer that hyperspectral system can sense. Based on the visual observation, the best contrast between the diseased area and the healthy area was in the spectral region from 1100 nm - 1300 nm.

Fig. 5.3 illustrates the mean reflectance spectra of the sour skin-infected onion sample shown in Fig. 5.2 in the spectral region of 950 nm - 1650 nm over 7 days. Mean spectra were calculated based on a manually selected ROI that approximately covered the whole onion area. The control spectrum was obtained from the HSI image scanned before inoculation, representing the spectrum of the healthy onion. The pattern of the mean spectra in fig. 5.3 indicates a tendency that reflectance intensity of the spectrum in the late stages (such as day 5 and after) is lower than spectra in the early stage. This characteristic matches the cycle of sour skin development. Sour skin was limited in a few inner bulb scales it occurred initially before the bacteria were able to affect the neighboring layers closer to the surface. When *B. cepacia* affected the scale that the HSI system can detect, the spectrum of the onion showed

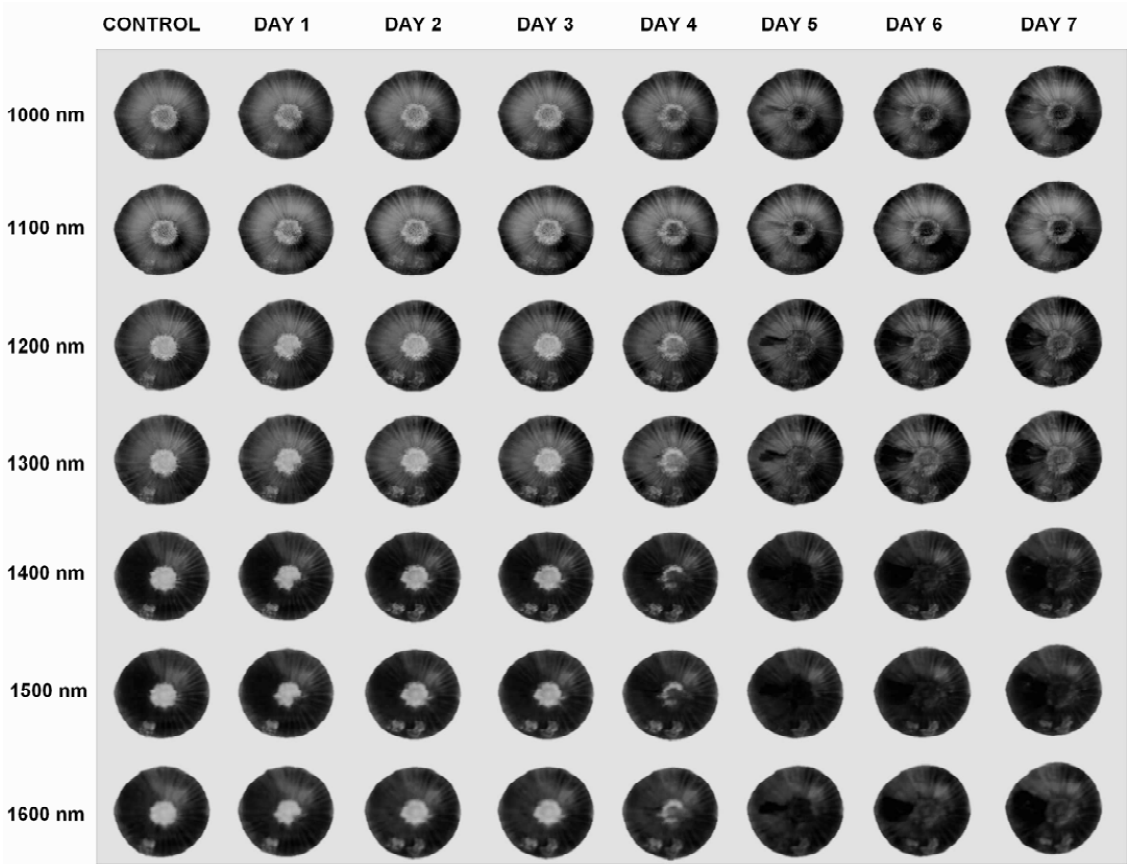

Figure 5.2: The mosaic image of one tested onion in Group II (root facing to the camera) at seven wavelengths (1000 nm - 1600 nm with 100 nm increments) before (control) and after inoculation with sour skin inoculum over 7 days.

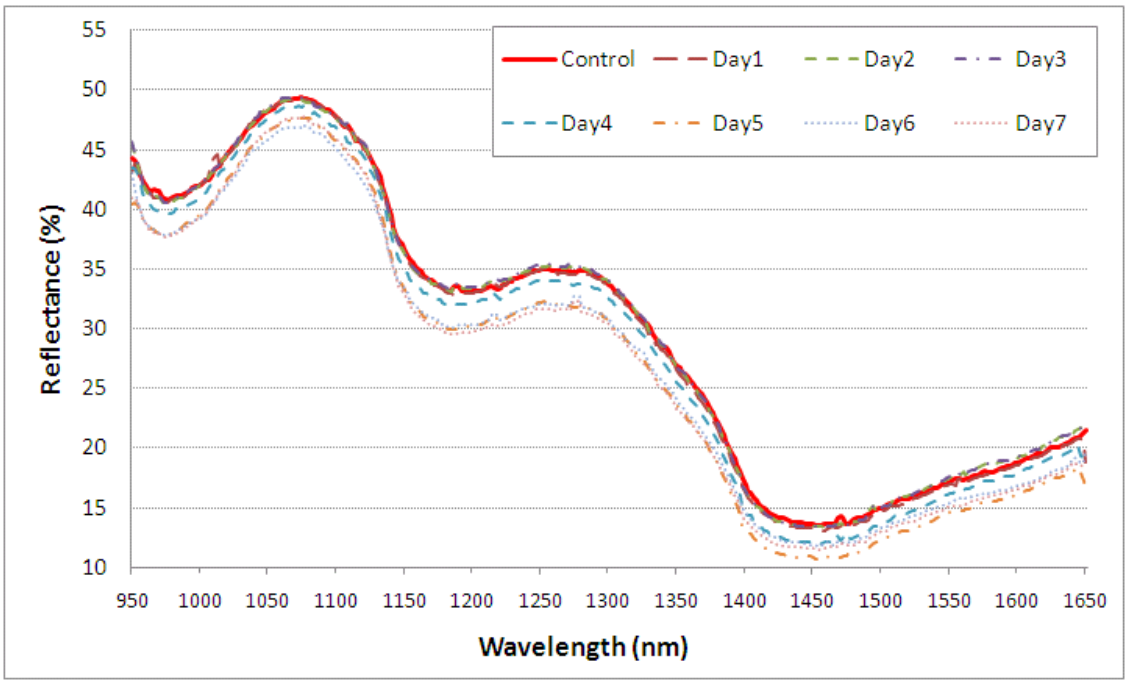

Figure 5.3: Mean relative reflectance spectra of one onion infected by sour skin over 7 days.

a step of change. This change can be credited to the increased water percentage in the scale caused by *B. cepacia*, which resulted in a higher absorption of light in the near-infrared region.

Hence, in this work, hyperspectral images of onion taken after day 4 were expected to contain sour skin information, and could be used for classification. From visual observation and color images of onions, most of the selected onion samples showed obvious sour skin symptoms at day 7 that can be easily detected by a human grader. This indicates that, in this test, the use of hyperspectral images after day 7 does not provide an advantage over using human visual inspection.

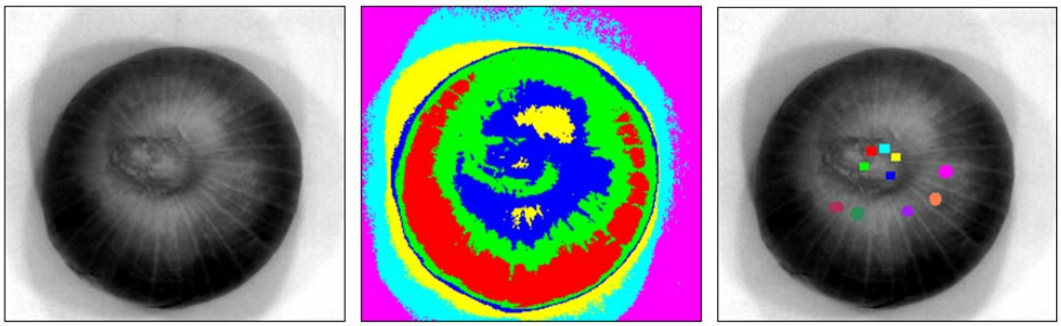

(a) (b) (c)

Figure 5.4: A demonstration of the algorithm for selecting ROIs on onion hyperspectral images: (a) The gray image at 1200nm; (b) Image partitioned by using density slice tool of ENVI; (c) Ten ROIs selected on neck and body area on the hyperspectral image of a tested onion.

5.4.2 Extracting spectral signatures of onions

Hyperspectral images of six randomly selected onion samples were used to provide spectra for feature selection. Square or circular region of interests (ROIs) were selected manually for extracting near-infrared reflectance spectra by using the ROI tool in ENVI software (ITT Visual Information Solutions, Boulder, CO, USA). From direct observations on hyperspectral images, onion images obtained the best contrast at a narrow spectral band around 1200 nm. Therefore, ROIs were selected on the gray image at 1200 nm. Since onion blubs are spherical, different areas on onions with non-uniform surface could have different reflectance and diffuse properties. Thus, for ROI selection, geometric position of pixels on onion images should also be considered to reduce errors from non-uniform geometric shapes. In addition, from a preliminary study, root, neck and flesh tissue of onions have slightly different spectral NIR spectral signatures. Thus, spectra should be extracted from both the flesh body area and root/neck area, to represent original onion spectral information as well.

To alleviate the error introduced by geometric differences, the density slice tool of ENVI was used to partition the gray image to different areas based on predefined pixel ranges. It was assumed that the geometric variance in the same density level region be small. Hence, ROIs were selected from image regions in the same density level. Fig. 5.4 demonstrates procedures of selecting ROIs on an onion hyperspectral image based on an image partitioned by using the density slice tool. The image intensity range of the gray image at 1200 nm was first divided into six ranges evenly. ROIs in the same group had the same radius to centre of the onion image to minimize geometric differences among selected areas. For each hyperspectral image, 5 ROIs were selected on flesh body area and another five ROIs were selected from either root or neck area for spectral data extraction. Every ROI contains about 50-60 pixels. As a result, 500-600 spectra were extracted and saved from each onion hyperspectral image. Spectra extracted from hyperspectral images of control onion samples were labeled as 'healthy', whereas spectra obtained from onions hyperspectral images after inoculation were labeled as 'diseased'.

5.4.3 Optimal wavelengths selection

Principal component analysis was conducted on the near-infrared reflectance spectral data set to reduce the dimensionality of original dataset. The eigenvalues of the PCA model are shown in Fig. 5.5. The majority (95.95%) variance of original training dataset can be represented by the first PC. The second PC explains 3.6% of the variance from the original data. The 99.55% variance of the spectral dataset can be explained by the first two principal components.

Fig. 5.6 shows the scatter plot of the near-infrared spectral data using the first two principle components. In Fig. 5.6, two clusters of spectra extracted from healthy and diseased onion hyperspectral images are completely separated. This indicates that spectral signatures of healthy and diseased onion tissue are distinguishable using the first two PCs. However, a single PC is a linear transformation of original data with full wavelength bands. Even using

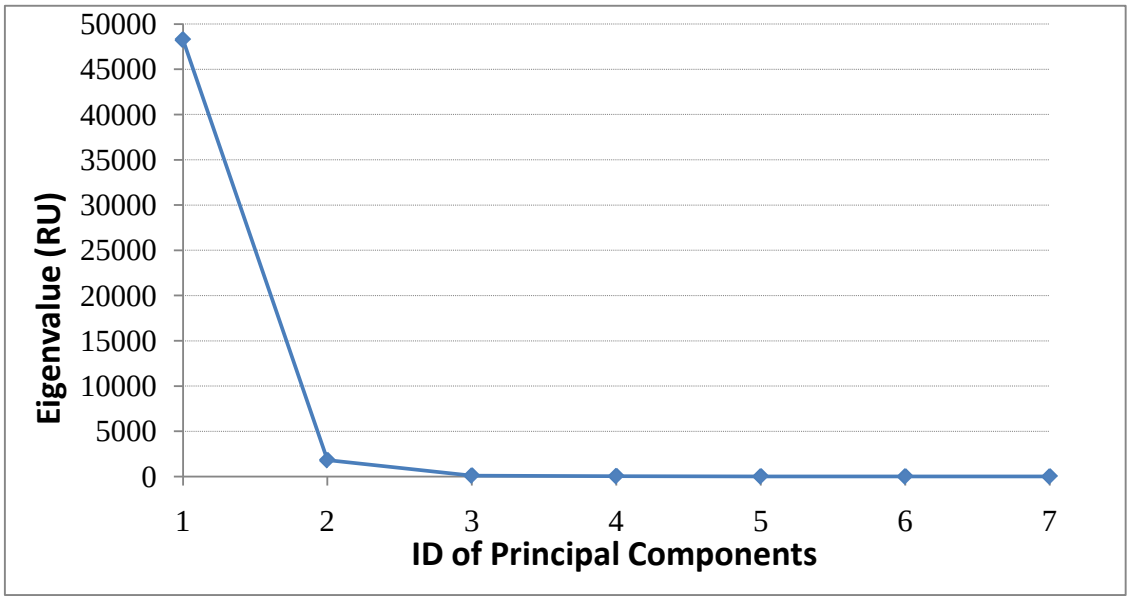

Figure 5.5: Scree plot of eigenvalues of the PCA model.

the first two PCs, a classification system based on PCs requires a spectral data acquisition over the full wavelength range. In this work, we expected to use only a few wavelength bands to build a fast classification system. Thus, the coefficients (PC loading values) of the first two PCs were studied further, to select a small number of original wavelength bands for classification.

Fig. 5.7 shows the distributions of PC loading values of the first two PCs. The goal of studying these PC loadings was to select two optimal wavelength bands for creating band ratio images. Although the PC1 explains the majority of original dataset's variance, the second PC was considered because we wanted to identify two independent wavelength bands. Since PC1 and PC2 are orthogonal and independent, the strategy of selecting optimal wavelength bands was to find the dominant band in the PC1 and PC2. In Fig. 5.7, the global peak of PC1 is located at the spectral region of 1370 nm-1420 nm, which is the spectral region that contributes most to the PC1. As for the PC2, the global peak is in the spectral region

of 1050 nm-1100 nm. As a result, the center bands of these two wavelength regions, 1400 nm and 1070 nm, were selected as optimal wavelength bands for the classification model based on bands ratio images.

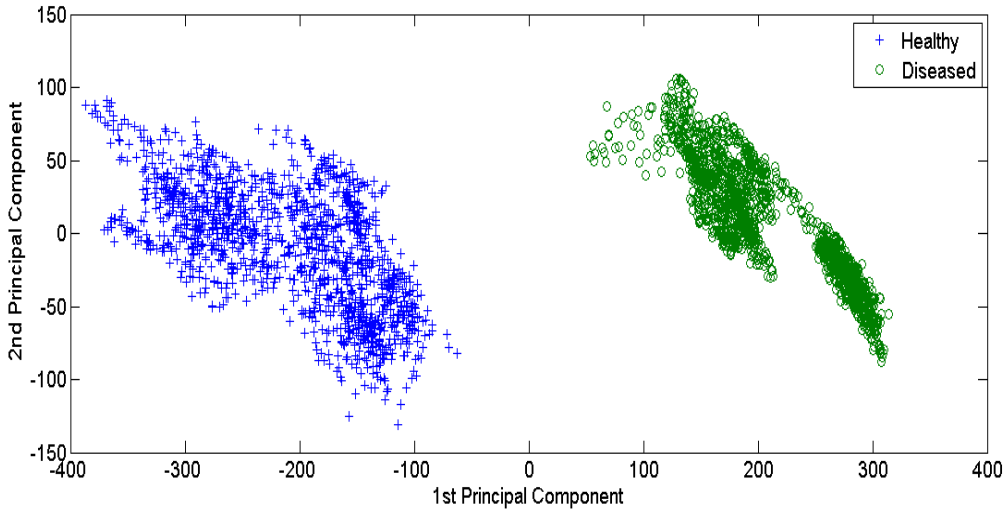

Figure 5.6: Scatter plot of PC1 versus PC2 the PCA on near-infrared spectral data extracted from hyperspectral images of healthy and diseased onions in the spectral region of 950 nm - 1650 nm.

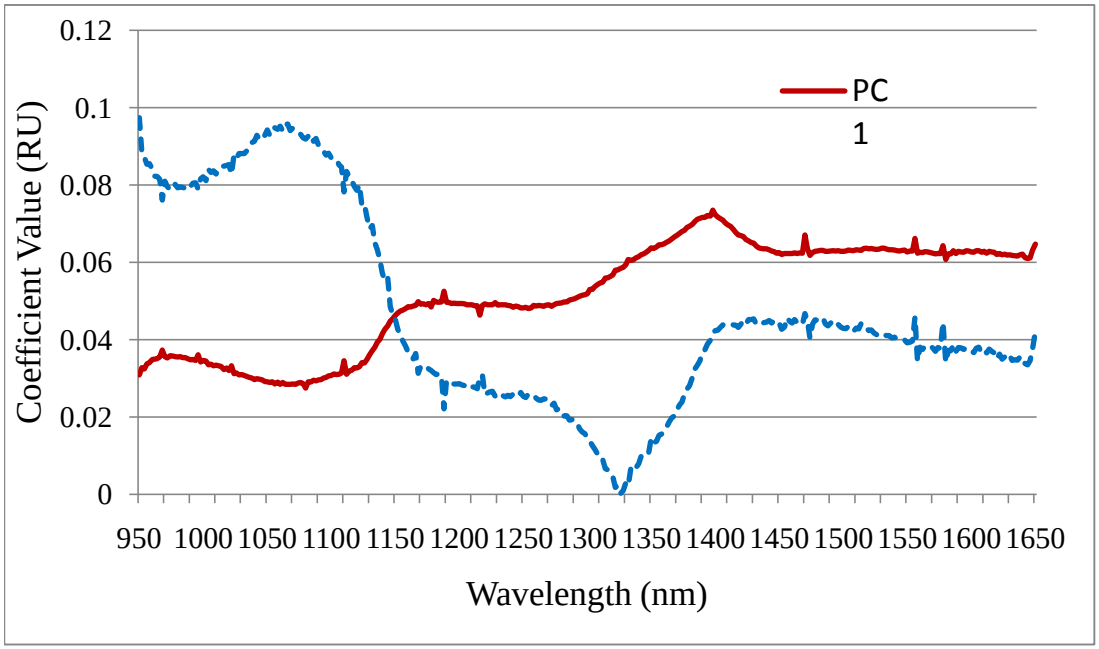

Figure 5.7: Plot of coefficients (PC loading values) of PC1 and PC2 of the PCA model of spectral signatures of healthy and sour skin-infected onions in the spectral region 950 nm - 1650 nm.

5.4.4 Bands ratio image

Using two optimal wavelengths, 1070 nm and 1400 nm, the ratio images of onion samples were calculated by the following equation:

$$I_{ratio} = \frac{I_{1070nm}}{I_{1400nm}}$$

The I_{1070nm} and I_{1400nm} are relative reflectance images at 1070 nm and 1400 nm, respectively. The zero values of denominator (in I_{1400nm}) were treated as background and excluded from computation to avoid infinite values in ratio image. Fig. 5.8 shows two ratio images of one onion sample before inoculation (control) and at day 5 (diseased).

In Fig. 5.8, patterns of band ratio images of healthy onion and the onion infected by sour skin are very distinct. The biggest difference is shown in the neck area of the onion. In ratio images, the neck area of the diseased onion is much brighter than the neck area of healthy onion. This characteristic can be explained by the water content change on surface layers.

Taking the original images of the onion shown in Fig. 5.2 as an example, the overall intensity of the onion image at 1400 nm was lower than that of the image at 1070 nm. When the onion was infected by sour skin, liquid seeped out from diseased onion flesh tissue was absorbed more by dry leaves in neck area and tissues on root cap. It is known that the absorption peak of water in near infrared region is around 1450 nm (Williams et al., 1987).

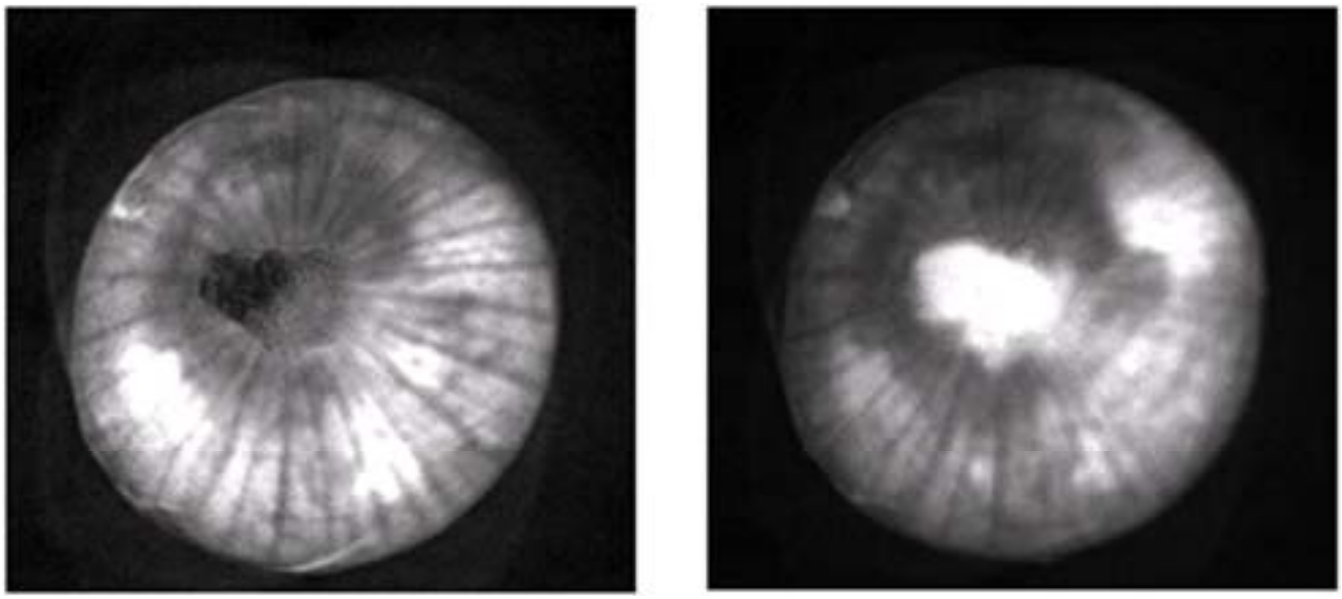

Figure 5.8: Band ratio images of an onion sample (1070 nm/1400 nm); the left band ratio image was extracted from the hyperspectral image of control, and the right image was attained from the hyperspectral image of the onion taken at day 5.

The reason that the band ratio image shows more evident difference between control and inoculated onions is two-fold. First, the reflectance intensity of the neck/root area decreased more rapidly than the body area in the image at 1400 nm. Second, the effect of the change pixel intensity values caused by water content change was stronger at 1400 nm than at 1070 nm. Thus, band ratio images which take advantages of these two features can detect sour skin in onions more sensitively than original gray images.

5.4.5 Image feature extraction and classification

An IDL (Interactive Data Language) program was written to extract grayscale images at 1070 nm and 1400 nm and calculate band ratio images from hyperspectral images automatically. Images were saved in TIFF format. Extracted images were processed to generate input features for classification. Before extracting features for classification operation, image enhancement operations were applied on images to remove background, identify edge of the onion, and build masks of onion neck/root area for each image. The image processing and feature extraction programs used were written in MATLAB (2009b, The MathWorks, Natick, MA, USA).

The grayscale image at 1070 nm was selected to provide original image information of the onion because it has higher light reflectance rate than the band of 1400 nm (as shown in Fig. 5.3). Consequently, onion images at 1070 nm have higher S/N (signal to noise) rate and higher contrast than images at 1400 nm. To extract image features, binary image masks for onion area and onion neck/root area were created on the onion gray image at 1070 nm by using following algorithm.

To minimize the confusion from background information on the classification process, background segmentation was performed by using a histogram-based automatic thresholding method (Jain et al., 1995). All pixels in background area were set to dark (pixel value to 0) to remove original information, which contained noisy spatial information of sample holder and light shades of the onion. Based on results of background segmentation, edge of onion bulb

was determined and the image was converted to a binary image. By applying morphological erosion operations, the foreground (white area) in binary image shrank further to fit the onion bulb in the image, which generated a binary mask for partitioning an onion bulb from the background.

The next step was segmentation of onion neck/root area. To enhance the image contrast, morphological top-hat filtering and bottom-hat filtering operations (Sonka et al., 1999) were applied. After that, a texture filter that calculated the local standard deviation was applied to extract the texture features of an onion image for segmenting root or neck area. The image after texture analysis was converted to a binary image by using an automatic histogram-based threshold segmentation method. Morphological erosion and dilation operations were performed on the binary image so that a bitter fit was obtained between the white area and the neck/root area. The binary image, joined with the binary mask determined above, could partition the onion image to background, neck or root, and body areas. Finally, mean pixel intensity values of neck/root area, body area, and the whole onion area were calculated, which were used as input features for classification.

BPNN and SVM classifiers were trained using the training dataset that contained 30 spatial patterns extracted from onion images scanned before inoculation (15 patterns, as healthy) and at day 6 (15 patterns, as diseased). All tested classifiers achieved 100% classification accuracy over training and validation datasets. Then, classifiers were evaluated by the testing dataset, which consisted of 20 patterns of 10 healthy (before inoculation) and 10 diseased (at day 6) onions. Table 5.1 shows the classification results of BPNN and SVM models.

The highest classification rates (95%) were obtained by two BPNN models. In general, the BPNN classifiers performed better than SVM classifiers. When the three image features extracted from original onion image at 1070 nm were removed, the BPNN classifier achieved the same performance with the previous BPNN model using six image features. The SVM classifier even performed better on the dataset that only contains three image

features extracted from band ratio images. The improved performance of the SVM classifier on dataset II can be explained by the curse of dimensionality on the dataset. Three image features from original onion images increased the complexity of sample space and reduced the sensitivity of the classifier. This also indicates that the three image features extracted from band ratio images are sufficient to provide information to discriminate healthy onions and onions infected by sour skin. Hence, the proposed BPNN classifier using image features (mean pixel intensity values of root/neck area, body area, and overall onion area) in band ratio images is the best model for this purpose.

The optimal classification algorithm determined above was applied to hyperspectral images scanned over 1-7 days after inoculation. To provide patterns of healthy onions, spatial features extracted from ration images of onions before inoculation (healthy) were added to datasets of 1-7 days. Table 5.2 lists the classification results of the BPNN classifier on the testing dataset which contains 20 (10 healthy and 10 diseased) patterns calculated from ratio images of 10 independent onion samples on different days. The classifier misclassified all 10 infected onions as healthy at day 1 and day 2. On day 3, the classifier discriminated infected

Table 5.1: Comparison of classification results of BPNN and SVM models on the testing data set, which contains 20 patterns from hyperspectral images of onions scanned before inoculation and inoculated onions at day 6

Image Features Used	Classifiers	False positive (%)[a]	Loss (%)[b]	Correct Prediction	Accuracy (%)
Six spatial features from ratio/1070 nm images	BPNN	1	0	19	95
	SVM	3	0	17	85
Three spatial features from ratio image	BPNN	1	0	19	95
	SVM	2	0	18	90

[a] False positive (%) = 100 × no. of diseased onions predicted as good ones/total no. of onions
[b] Loss (%) = 100 × no. of good onions predicted as bad ones/total no. of inspected onions

onions and healthy onions with a 50% false positive rate. Starting from day 4, the overall classification rates of the BPNN classifier were improved to 80% and above.

Table 5.2: Classification results of the onions on the testing datasets by using the BPNN classifier with three spatial features extracted from band ratio images

Classification Rates	Days After Inoculation						
	Day 1	Day 2	Day 3	Day 4	Day 5	Day 6	Day 7
Correct Prediction	10	10	14	16	17	19	20
Loss	0	0	1	2	0	0	0
False Positive	10	10	5	2	3	1	0
Total Accuracy	50%	50%	70%	80%	85%	95%	100%

This result coincides with our previous hypothesis obtained from visual observations on Fig. 5.2 and Fig. 5.3: onion hyperspectral reflectance images scanned after day 3 could provide useful spatial and spectral information for differentiating healthy and sour skin-infected onions. It also indicates the promise of using the proposed classification approach for detecting sour skin-infected onions at its early stage such as at day 3 or day 4 after inoculation in this work.

5.5 Conclusion

The near-infrared hyperspectral reflectance image technique showed promise for detecting onions infected by sour skin as early as 3-4 days after inoculation. A fast and effective classification approach can be developed based on ratio images of onions at optimal wavelength bands 1070 nm and 1400 nm, which were determined by principal component analysis on spectral signatures of healthy and sour skin-infected onions. The BPNN classifier using spatial features extracted from band ratio images achieved higher correct classification rate (95%) than the SVM model (90%) for discriminating healthy onions and inoculated onions on day 6 after inoculation. The result of this study can be utilized to further develop a multispectral imaging system for early detection of Vadalia sweet onions infected by sour skin.

5.6 Acknowledgements

This work was funded by the USDA NIFA Specialty Crop Research Initiative (Award No. 2009-51181-06010). The authors also gratefully acknowledge the financial support provided from Georgia Food Industry Partnership and Vidalia Onion Committee.

5.7 Bibliography

Ariana, D. P., Lu, R., 2008. Detection of internal defect in pickling cucumbers using hyperspectral transmittance imaging. Transactions of the ASABE 51 (2), 705–713.

Ariana, D. P., Lu, R., Guyer, D. E., 2006. Near-infrared hyperspectral reflectance imaging for detection of bruises on pickling cucumbers. Computers and Electronics in Agriculture 53 (1), 60–70.

Birth, G., Dull, G., Renfroe, W., Kays, S., 1985. Nondestructive spectrophotometric determination of dry matter in onions. Journal of the American Society for Horticultural Science 110 (2), 297–303.

Boatright, S. R., McKissick, J. C., 2009. 2008 georgia farm gate value report. Tech. rep., The University of Georgia, Center for Agribusiness and Economic Development College of Agricultural and Environmental Sciences.

Burkholder, W. H., 1950. Sour skin, a bacterial rot of onion bulbs. Phytopathology 40 (1), 115–117.

Chmiel, J., Davis, P., 2003. State of the art: Why do the lungs of patients with cystic fibrosis become infected and why can't they clear the infection? Respiratory Research 4 (1), 8.

Cortes, C., Vapnik, V., 1995. Support-vector networks. Machine Learning 20 (3), 273–297.

Eberhart, R. C., Shi, Y., 2007. Computational intelligence : concepts to implementations. Elsevier/Morgan Kaufmann Publishers, Amsterdam ; Boston.

ElMasry, G., Wang, N., Vigneault, C., Qiao, J., ElSayed, A., 2008. Early detection of apple bruises on different background colors using hyperspectral imaging. LWT - Food Science and Technology 41 (2), 337–345.

Gitaitis, R. D., 1994. Bacteriology results, 1993 onion trials. Tech. rep., University of Georgia, College of Agriculture and Environmental Sciences, Cooperative Extension Service.

Gowen, A. A., O'Donnell, C. P., Cullen, P. J., Downey, G., Frias, J. M., 2007. Hyperspectral imaging - an emerging process analytical tool for food quality and safety control. Trends in Food Science & Technology 18 (12), 590–598.

Grahn, H., Geladi, P., 2007. Techniques and applications of hyperspectral image analysis. J. Wiley, Chichester, England ; Hoboken, NJ.

Isles, A., Maclusky, I., Corey, M., Gold, R., Prober, C., Fleming, P., Levison, H., 1984. Pseudomonas cepacia infection in cystic fibrosis: an emerging problem. J Pediatr 104 (206).

Jain, R., Kasturi, R., Schunck, B. G., 1995. Machine vision. Artificial intelligence. McGraw-Hill, New York.

Kim, M. S., Lefcourt, A. M., Chao, K., Chen, Y. R., Kim, I., Chan, D. E., 2002. Multispectral detection of fecal contamination on apples based on hyperspectral imagery: Part I. application of visible and near-infrared reflectance imaging. Transactions of the American Society of Agricultural Engineers 45 (6), 2027–2037.

Lawrence, K. C., Windham, W. R., Park, B., Smith, D. P., Poole, G. H., 2004. Comparison between visible/NIR spectroscopy and hyperspectral imaging for detecting surface contaminants on poultry carcasses. Vol. 5271 of Proceedings of SPIE - The International Society for Optical Engineering. SPIE, pp. 35–42.

Li, C., Gitaitis, R., Tollner, B., Sumner, P., MacLean, D., 2009. Onion sour skin detection using a gas sensor array and support vector machine. Sensing and Instrumentation for Food Quality and Safety 3, 193–202.

Lu, R., 2003. Detection of bruises on apples using near-infrared hyperspectral imaging. Transactions of the American Society of Agricultural Engineers 46 (2), 523–530.

Lu, R., Chen, Y.-R., 1998. Hyperspectral imaging for safety inspection of food and agricultural products. Proceedings of SPIE - The International Society for Optical Engineering 3544, 121–133.

Maw, B., Hung, Y., Tollner, E., Smittle, D., 1989. Some physical properties of sweet onions. In: ASAE. No. Paper No. 896007. St. Joseph, Mich.

Park, B., Lawrence, K. C., Windham, W. R., Buhr, R. J., 2002. Hyperspectral imaging for detecting fecal and ingesta contaminants on poultry carcasses. Transactions of the American Society of Agricultural Engineers 45 (6), 2017–2026.

Qin, J., Burks, T. F., Kim, M. S., Chao, K., Ritenour, M. A., 2008. Citrus canker detection using hyperspectral reflectance imaging and PCA-based image classification method. Sensing and Instrumentation for Food Quality and Safety 2 (3), 168–177.

Qin, J., Burks, T. F., Ritenour, M. A., Bonn, W. G., 2009. Detection of citrus canker using hyperspectral reflectance imaging with spectral information divergence. Journal of Food Engineering 93 (2), 183–191.

Rencher, A. C., 2002. Methods of multivariate analysis, 2nd Edition. Wiley series in probability and statistics. Wiley-Interscience, New York.

Schwartz, H. F., Mohan, S. K., 2008. Compendium of onion and garlic diseases and pests, 2nd Edition. Disease compendium series of the American Phytopathological Society. APS Press, American Phytopathological Society, St. Paul, Minn.

Shahin, M. A., Tollner, E. W., Gitaitis, R. D., Sumner, D. R., Maw, B. W., 2002. Classification of sweet onions based on internal defects using image processing and neural network techniques. Transactions of the American Society of Agricultural Engineers 45 (5), 1613–1618.

Sonka, M., Hlavac, V., Boyle, R., 1999. Image Processing, Analysis, and Machine Vision. International Thomson Publishing, Tampa, FL.

Tollner, E. W., Hung, Y. C., Maw, B. W., Sumner, D. R., Gitaitis, R. D., 1995. Nondestructive testing for identifying poor-quality onions. Vol. 2345 of Proceedings of SPIE - The International Society for Optical Engineering. Society of Photo-Optical Instrumentation Engineers, pp. 392–402.

Williams, P., Norris, K. H., of Cereal Chemists., A. A., 1987. Near-infrared technology in the agricultural and food industries. American Association of Cereal Chemists, St. Paul, Minn., USA.

Yoon, S. C., Park, B., Lawrence, K. C., Windham, W. R., Heitschmidt, G. W., 2010. Development of real-time line-scan hyperspectral imaging system for online agricultural and food product inspection. Proceedings of the SPIE 7676, 76760J–76760J–11.

Chapter 6

Conclusions

Shortwave infrared (SWIR) spectral imaging is a powerful tool for food safety and quality inspection. This research consists of three aspects through chapters 3, 4, and 5, which are related with SWIR spectral imaging development and application. Chapter 3 thoroughly demonstrates the design, implementation and calibration processes of a liquid crystal tunable filter (LCTF) based SWIR spectral imaging system. Chapter 4 describes the development of a reliable and robust data acquisition software program for this LCTF-based SWIR spectral imaging system. Chapter 5 reports an application of using the SWIR spectral imaging to detect sour skin in Vidalia sweet onions.

6.1 Contributions

A spectral imaging system was developed for collecting hyperspectral or multispectral images in the spectral region of 900 - 1700 nm. The system was based on the liquid crystal tunable filter and has been fully calibrated and optimized in spatial and spectral domain. This system is particularly suitable for applications that require a fast selection of spectral bands and high quality image in the spectral region of 900 - 1700 nm. The results of calibration tests and preliminary experimental tests verified the accuracy of the system in the spectral and spatial domains, and demonstrated its capability for food safety and quality inspection.

Development of spectral image acquisition software is a grey area that is rarely discussed in depth in the literature. Chapter 4 fills this gap and demonstrates the design and implementation process of the spectral imaging data acquisition LabVIEW software. The software

was designed meticulously to achieve best liability and extensibility. Several build-in calibration/preprocessing/denoising functions were added to the software to enhance the quality of the captured spectral images.

The spectral imaging system developed in this work was used to collect data to detect sour skin in Vidalia onions in the laboratory. A fast classification approach was developed based on ratio images of onions at two optimal wavelength bands (1070 nm and 1400 nm). Results of these tests showed that the SWIR spectral imaging is a very promising technique to differentiate between healthy onions and sour skin-infected onions.

In summary, this research developed a high-performance spectral imaging system for nondestructive measurements of food and agricultural products in the spectral range of 900 - 1700 nm. This system demonstrated its potential to detect diseased onions by successfully detecting sour skin-infected onions in the early stage. The system and the SWIR spectral imaging techniques developed in this research could be extended for testing other foods and agricultural products.

6.2 Suggestions for Future Research

The development of this LCTF SWIR spectral imaging system provides a foundation for future studies regarding onion postharvest quality inspection and classification. Future research could be carried out in the following aspects:

- Make some adjustments on the configuration of this SWIR spectral imaging system, so that the LCTF-based spectral imager and software can be used for SWIR transmittance and scattering spectral image acquisition.

- Add and enhance functions of the data acquisition software program to include real-time image processing functions, and further improve the performance (speed, sensibility, etc) for achieving fast and automated inspection.

- Develop more effective feature selection and classification methods to process hyperspectral image data.
- Apply this system to predict onion internal quality properties such as dry matter content and sugar content at the spectral region from 900 nm to 1700 nm.
- Use this SWIR spectral imaging system for food safety and quality inspection of other agricultural products such as cotton fiber quality.

Appendix A

The flange focal distances of common lens mount types

Mount Type	Flange Focal Distance (mm)
C-mount	17.52
Canon EF mount	44
Sony Alpha mount	44.5
Nikon F-mount	46.5
M42	45.46
T-mount	55

Appendix B

Partial source codes of the spectral imaging LabVIEW software program

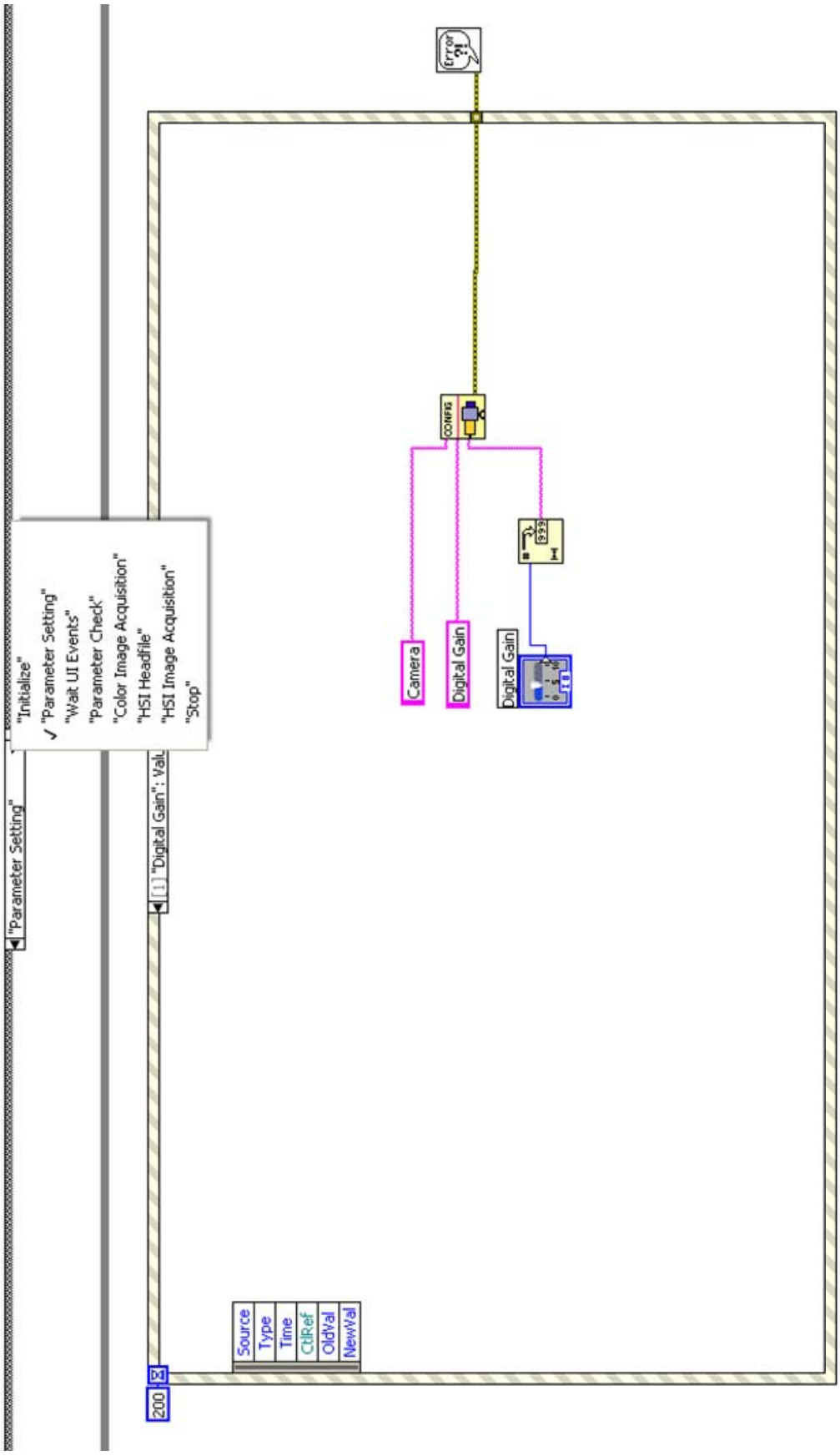

(a) The main structure (Finite State Machine)

(b) The status of previewing images and setting parameters

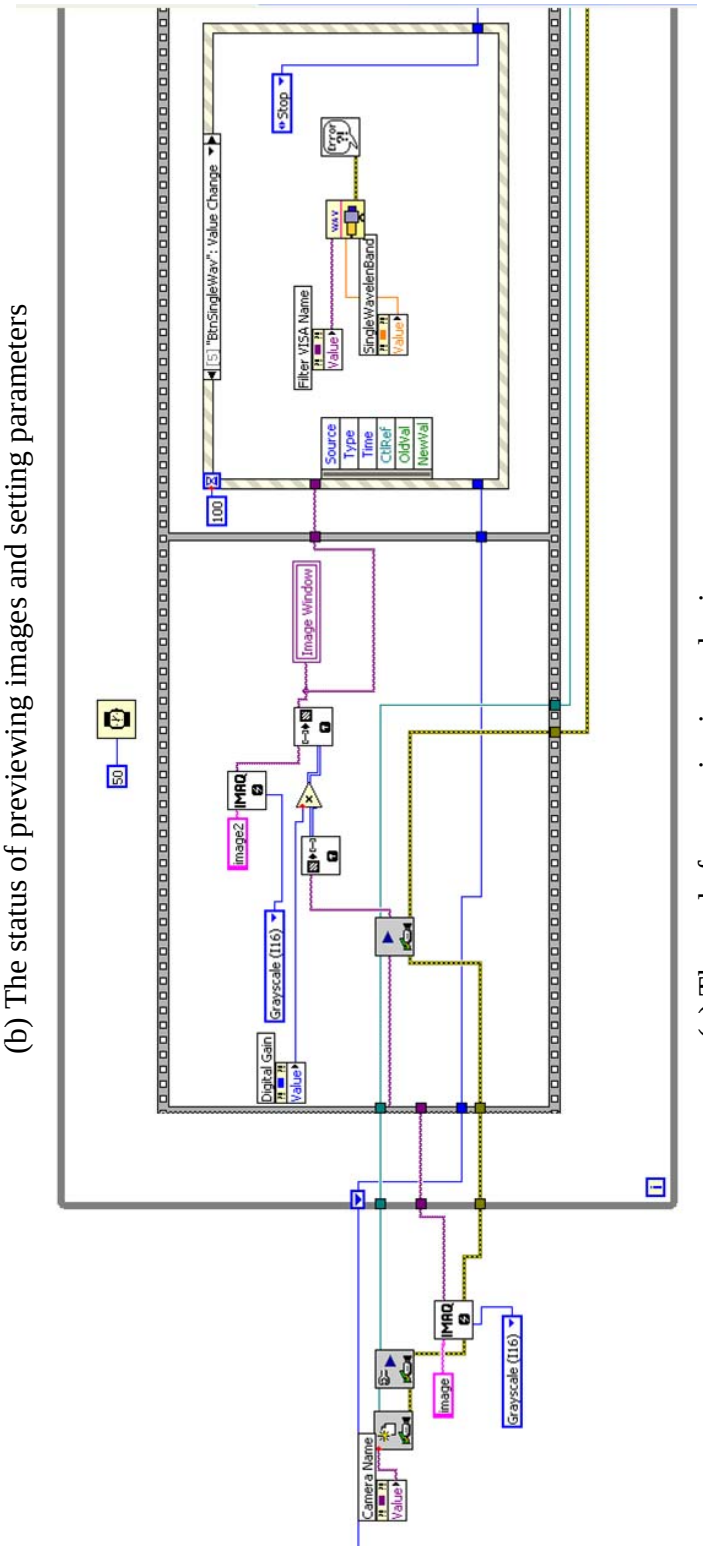

(c) The code for previewing color images

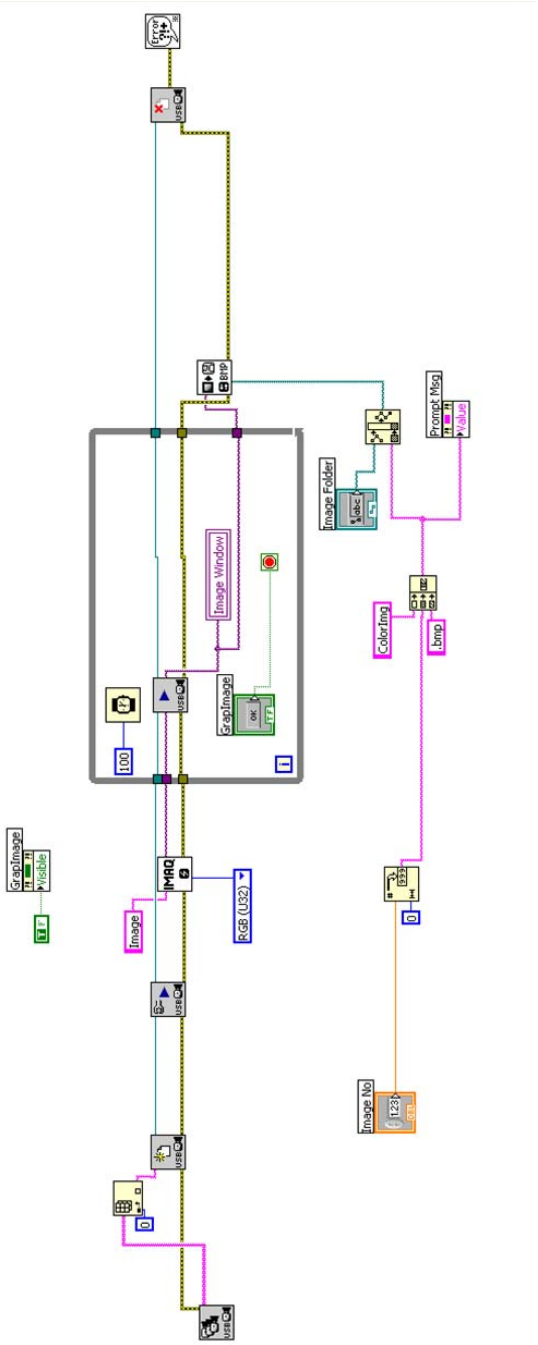

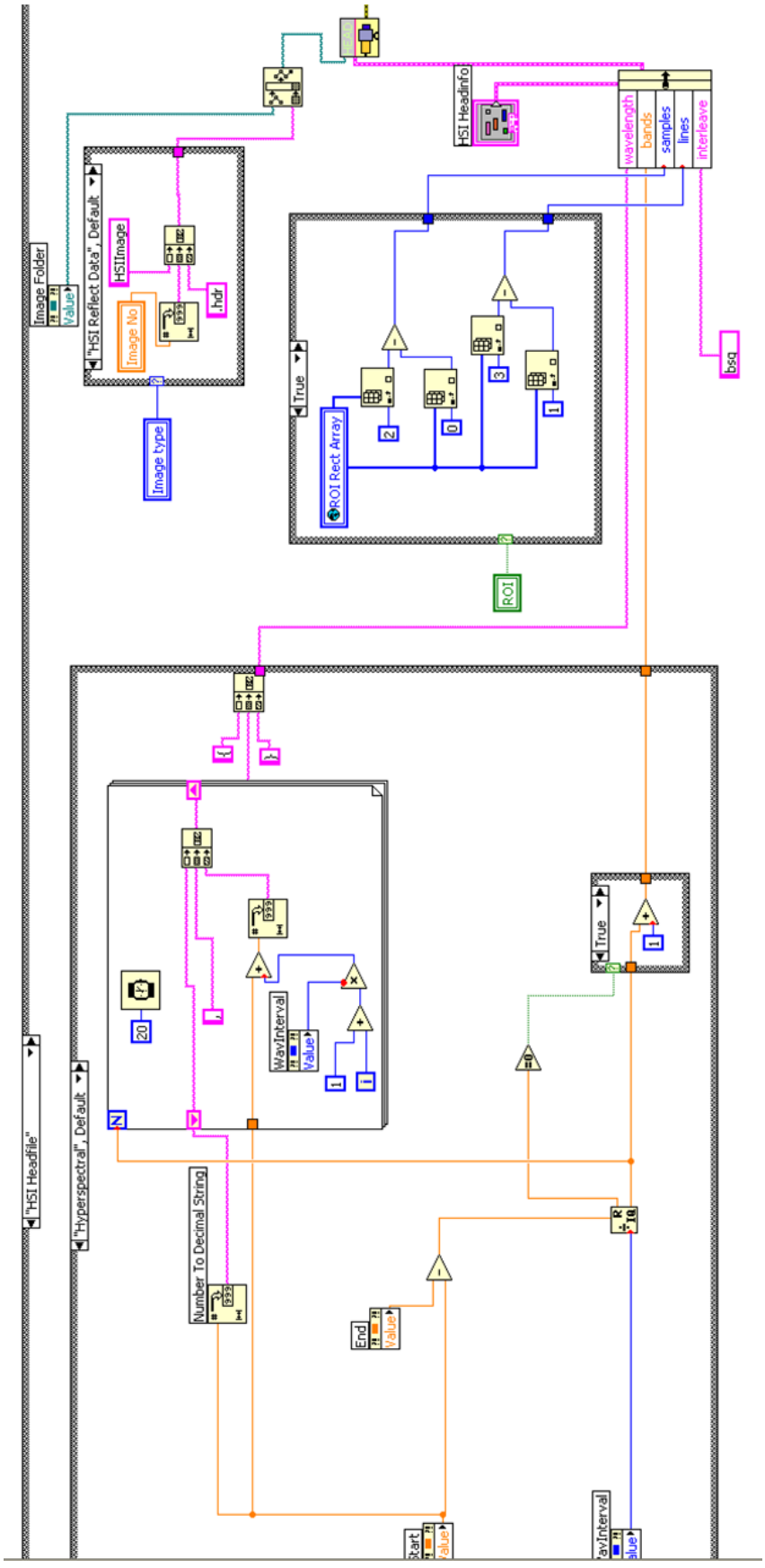

(d) The code for creating the headfile of the spectral image

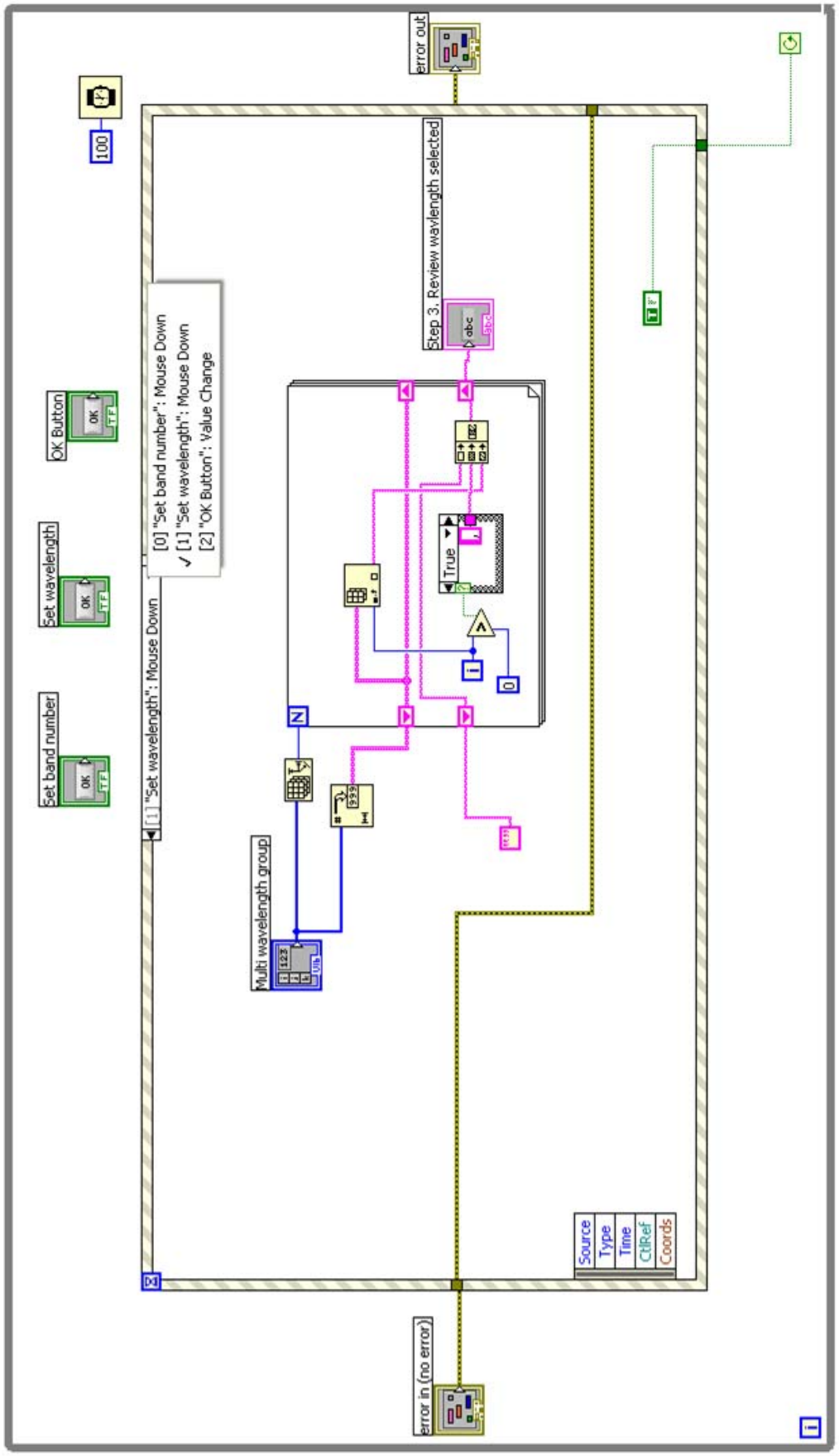

(e) The code of setting the wavelength bands for a multispectral image acquisition

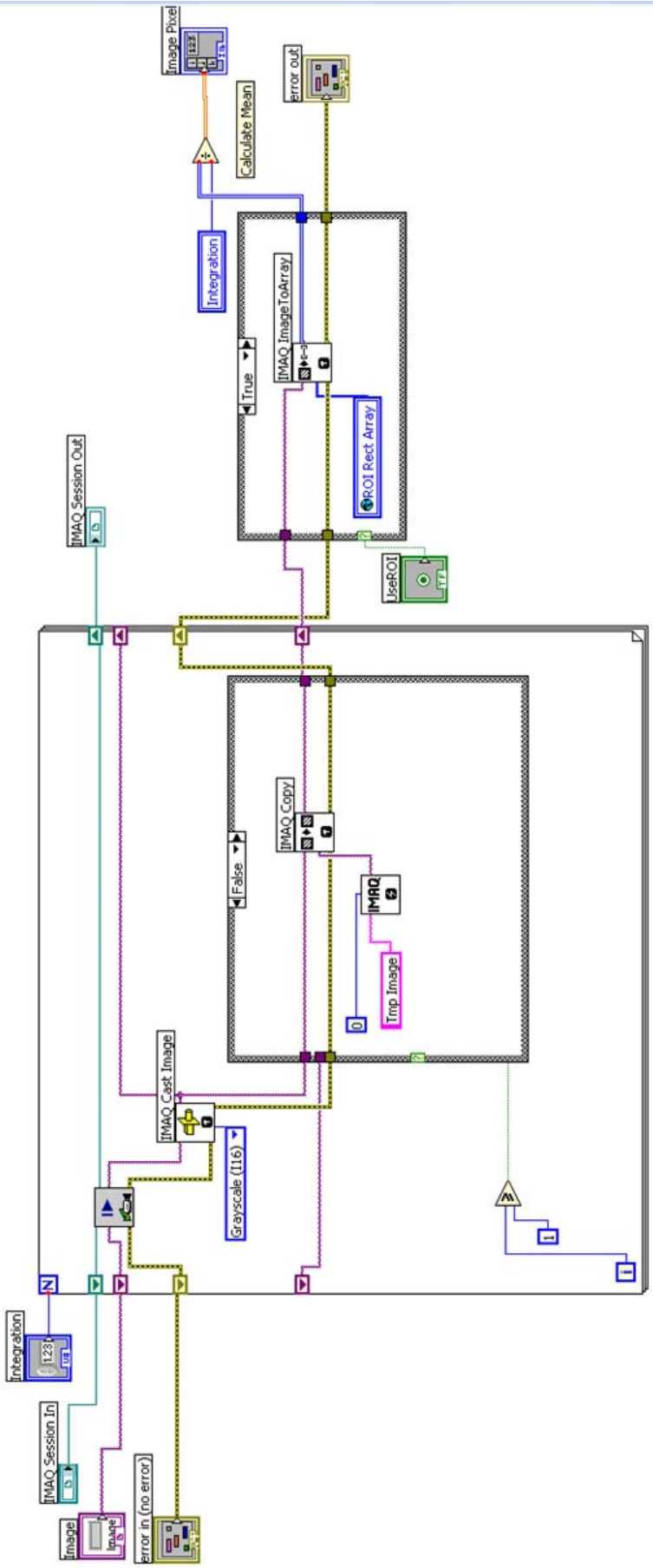

(f) The code of capturing images for a hyperspectral or multispectral image acquisition